Meeting Minutes

CEOS WGCV IVOS Fall92 Meeting

at NOAA Science Center, Camp Springs, MD, USA

November 30 - December 1, 1992

Tech. Team Mtg. 12/3/92

Meeting Minutes
CEOS WGCV IVOS Fall92 Meeting
at NOAA Science Center, Camp Springs, MD, USA
November 30 - December 1, 1992

AGENDA
November 30, 1992

1000	**Welcome**
1010	**Agenda**
1020	Brief Member Reports
	USA - NOAA, NASA, U of Arizona
	Canada
	France
	U.K.
	-EROS
	-JRC
	Australia
1100	Terms of Reference
	WGCV - S. Till
	IVOS
1130	AVHRR Status
	Other Instruments
1215	**Lunch**
1315	Pathfinder
1400	On-Board-Calibration (OBC)
	ATSR -2 (U.K.)
	MODIS (NASA)
	OTHER (SeaWiFS)
1500	Coordination
1600	Funding
	Interaction with Other Groups
1730	**Close**

December 1, 1992

- Initial Activities
- -Test Sites
- -AVHRR

- Future Campaigns, Sensors, & Plans

Meeting Minutes
CEOS WGCV IVOS Fall92 Meeting
at NOAA Science Center, Camp Springs, MD, USA
November 30 - December 1, 1992

Use CEOS Newsletter and Bulletin Board for communications
send information to Susan Till (CCRS Email Omnet or Internet) on
Up-coming meetings/campaigns with potential for international participation
Contact points for Cal/Val for satellite sensors
Up-dates on parameters and coefficients for satellite sensors
References to new reports
Lexicon (will be reviewed by WGCV)

Action Items

1. U. Arizona

To investigate a mechanism for wider use of White Sands test site during their intensive ground-based campaigns

2. CNES

To investigate a means whereby satellite-derived data collected over ground test sites can be released for mutual in-flight calibration of all IVOS, and thus improve the characterization of the test sites for the mutual benefit of the space agencies involved.

A comprehensive set of radiometric histograms is already being prepared for SPOT.
CNES does not direct commercial activities of SPOT Image
NASA has a program directed from Headquarters for accessing a certain number of SPOT images.
What is the policy that should be developed or sought.
Could use

3. IVOS members

Think about comparison of radiative transfer codes.
NOAA/NASA---->
implementation of the "Pathfinder" activities and encouragement of other space agencies to support similar activities for other satellite systems.
for atmospheric correction of EOS Satellite data

Lowtran	
Hitran	
Genlin2 -	U. K./USA
5S (6S)	LOA (Tanri)
MODTRAN	
RAL	U. K.

Other more rigorous codes

Goals:

a) Minimize ambiguity in the comparison of calibration activities
b) Recommend code(s) for use in calibration

CEOS IVOS Objectives

1. To identify and agree on calibration and validation requirements and standard specifications for IVOS, including on-board calibration systems.

2. To promote international and national collaboration in the calibration and validation of all IVOS and thus assist in the improved application of data from satellite instruments.

3. To include all sensors (ground based, airborne and satellite) where there is a direct link to the Cal/Val of satellite sensors

4. To identify test sites and encourage continuing observations and inter-comparisons of data from these sites

5. To encourage the timely and unencumbered release of data relating to cal/val activities including details of pre-launch and in-flight calibration parameters.

Provisional: May, 1992
Confirmed: December, 1992

Recommendations to CEOS WGCV

1. Recognizing that accurate long term calibration is crucial (essential) for the use of satellite data in climate and global change applications, the IVOS recommends that CEOS member agencies support the identification, characterization, and maintenance of ground test sites for the verification of on-board calibration systems, the in-flight calibration of IVOS, and subsequent cross-calibration of instruments.

   Discussion:
   To ensure the accuracy and continuity of satellite data and their use for climate and global change research,
   vital activity that allows for quantitative scientific inter comparison of global change parameters derived from different instruments.
   In view of the on-going problems related to the use of in-flight calibration of IVOS, the IVOS recommends support the use of ground test sites for the cross-calibration of IVOS and their mutual benefit.
   Rocket Sounding Programs, Solar Radiation Networks and other existing sources of required ancillary data should be supported within this framework.

2. That, *as a matter of urgency,* CEOS supports the establishment of a comprehensive database on selected test sites for the future in-flight calibration of infrared and visible sensors.

   Discussion:
   IVOS is currently identifying test sites and exploring data collection procedures.
   ESA felt that there were so many test sites (e. g. Black Forest test sites for SAR, corner cubes are unreliable (move) and therefore sits are typically used for)
   Dossier
   an international

3. CEOS WGCV IVOS congratulates NOAA/NASA on the implementation of the "Pathfinder" activities and encourages the producers and users of satellite data to support similar activities for other satellite systems.

Drop item #4 as an already approved item at a previous WGCV meeting.

4. IVOS endorses the recommendations of ad-hoc group on data policy regarding the exchange and availability of data (including imagery at cost-of-copy prices).

Items to be revisited at next CEOS IVOS meeting:

1. Inter comparison of Radiative Transfer Codes
2. Collation of Data on test sites
3. Use and experience of histograms database of SPOT
4. Validation activities (wider application than planned?)

Schedule for next meeting

Philosophy:

Meet less than twice a year, perhaps every 9-10 months

Meet just before WGCV and stay through that meeting

Next Meeting

CEOS IVOS: Monday and Tuesday,
30MAY92 and 1JUN92 in Ispra, ITALY

CEOS WGCV: Wednesday, Thursday and Friday
2-4JUN92 in Ispra, ITALY

Attendees

at

CEOS (Committee on Earth Observation Satellites)
WGCV (Working Group on Calibration and Validation)
IVOS (Infrared Visible Optical Sensors)
NOAA Science Center (formerly World Weather Building)
Camp Springs, Maryland USA
Monday, 30 November 1992, and
Tuesday, 1 December 1992

Barker, John L.	NASA/Goddard Space Flight Center Code 925 Greenbelt, MD 20771 USA Barker@highwire.gsfc.nasa.gov Jbarker@GSFCmail 301 286-9498 301 296-9200 (FAX)
Barton, Ian	CSIRO, Australia PMB No. 1, Mordialloc Victoria 3195, Australia Barton@lamy.dar.csiro.au 61-3-5867666, FAX 5867600
Biggar, Stuart F.	University of Arizona Optical Sciences Center 1600 N. Country Club Road, Suite 100 Tucson AZ 85716 internet: stu@spectra.opt-sci.arizona.edu 602 621-8168 602-621-8292 (FAX)
Helder, Dennis	for EROS Data Center South Dakota State University P.O. Box 2220 Brrokings, SD 57007 605-688-4523 605-688-5880 (FAX) ee04@sdsumus.sdstate.edu
Henry, Patrice	CNES 18, Av. Edouard Belin 31055 Toulouse Cedex, France 33 6 12747-12/Phone 33 6-1273-167(FAX)
Maracci, Giancarlo	CEC JRC-IRSA IRSA - JRC TP.272 21020 Ispra (VA) Italy 39 332 789136 39 332 789034 (Fax)

Mo, Tsan	NOAA/NESDIS 301 763-8763 301 763-8108 (FAX)
Mutlow, Chris	RAL (Rutherford Appleton Lab (U. K.) BNSC Rutherfurd AppCeton Laboratory Chilton, Didcot, Oxon Ox11 OQX Email: SPAN RLVP::Chris +44 235 446525 +44 235 445848 (Fax)
Planet, Walter G.	NOAA/NESDIS E/RAI4 WWB Rm 810 Washington, D.C. 20233 301-763-8136 301-763-8108 (FAX)
Rao, C. R. Nagaraja	NOAA/NESDIS/SRL PBE/RA/4 World Weather Building, Room 810 Washington, D.C. 20233 301 763-8763 301 763-8108 (FAX) (Michael P. Weinreb...same as RAO) (Non-member)
Schiro-Zavela, Jean	NOAA/NESDIS E/IA1 FB. 4, Room 0110 Washington, D.C. 20233 301 763-4586 301-736-5828 (Fax) Email: J. schiro.zavela/Omnet
Sherman,John W. III	NOAA/NESDIS Jack only a few hours on Monday 301 763-4626
Staenz, Karl	CCRS (Canadian Center of Remote Sensing 588 South Street Ottawa, Ontario, Canada KIA 0Y7 613-947-1250/Phone 613 947-1250/FAX
Till, Susan	CCRS Canada Centre for Remote Sensing 588 Booth St., Ottawa, Ontario KIA 0Y7 Canada Internet: till@ccrs.emr.ca Omnet: S.Till 613 998-9060 613-993-5022
Weinreb, Michael	NOAA/NESDIS (only present on Monday) 301 763-8763 301 763-8108 (FAX)

Action for JohnBarker:

Co-ordinator for Action Items on Test Sites and On-Board Calibrators

Test Sites

All agencies are to develop a database for selected test sites and investigate a means for easy exchange of data. At the next IVOS meeting, this activity will be reviewed and a mechanism established to collate these data

Action:

1) By end of January, 1993, agencies are to make available the location of possible test sites, including low reflectance sites such as water (off Australia), and details of their size, homogeneity, time variability, etc.
2) A start should have been made on collecting data for/from White Sands and one site in North Africa
3) Develop ideas for the collation of test site data into useful data set

Chair: John Barker (NASA/GSFC)
Subcommittee: Stuart Biggar (UAz), Patrice Henry (CNES)

Do White Papers, report, & publication to co-ordinate effort

Inter comparison of solar diffusers and on-board calibration techniques

Chair: John Barker
Subcommittee: ESA

MODIS On-Board Calibration Overview

NASA CEOS/IVOS Member Report

John Barker, Head of MCST

Joann Harnden

Ken Brown

Steve Ungar

Brian Markham

Contributions

Paul Anuta - *Spectral Simulation* • Phil Ardanuy - *Schedules* • Jon Burelbach - *Image Processing*

Doug Hoyt - *Instrument Plans* • Jon Smid - *Sensitivity Studies* • Joan Baden - *Editor*

1 December 1992

NOAA Science Center (formerly World Weather Building)

Camp Springs, MD

John Barker (925) Phone: 301-286-9498 / Internet: JBarker@gsfcmail.nasa.gov or JBarker@highwire.gsfc.nasa.gov • **Joann Harnden** (925) Phone: 301-286-4133 / Internet: Harnden@highwire.gsfc.nasa.gov • **Ken Brown** (925) Phone: 301-286-3296 / Internet: KBrown@gsfcmail.nasa.gov • NASA / GSFC / Code 925 / Sensor Development and Characterization Branch / MODIS Characterization Support Team (MCST) / Goddard Space Flight Center, Greenbelt, MD 20771

Brian Markham (923) Phone: 301-286-5240 • **Steve Ungar** (923) Phone: 301-286-4007 / Internet: Ungar@highwire.gsfc.nasa.gov or SUngar@gsfcmail.nasa.gov • NASA / GSFC / Code 923 / Biospheric Sciences Branch / Goddard Space Flight Center, Greenbelt, MD 20771

Tech. Team Mtg - 12/3/92

On-Orbit Instrument-Based Calibration Methodology

MODIS Performance/Calibration Requirements

Calibration-Related Instrument and Data Design
- Solar Diffuser (SD)
- Solar Diffuser Stability Monitor (SDSM)
- Spectroradiometric Calibration Assembly (SRCA)
- Blackbody (BB)
- Space Port (SP)

GSFC Requirements Lead to Instrument Design

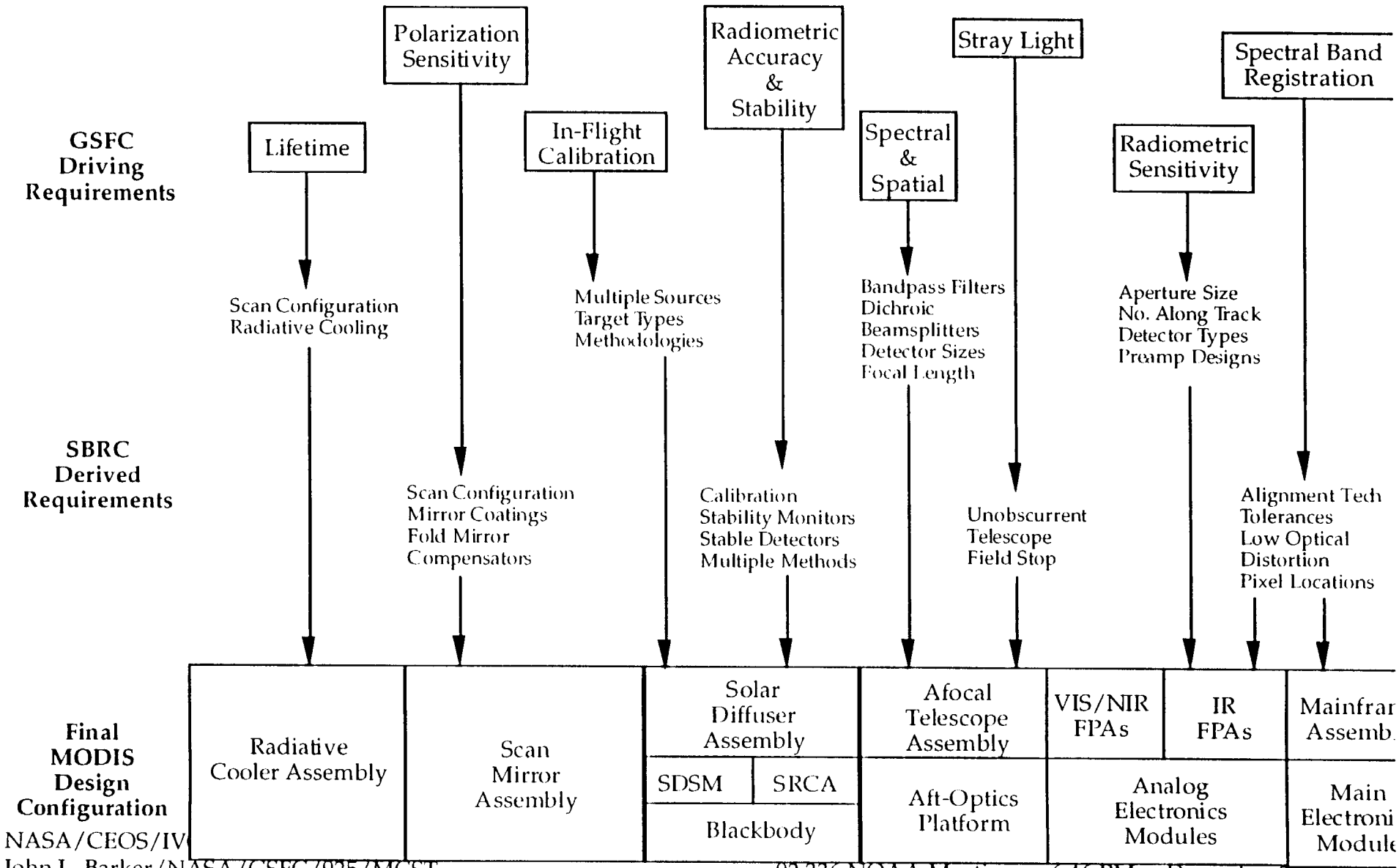

MODIS Calibration Requirements and On-board Calibrators

Specification		Calibrator
Radiometric		
Below 3.0 μm	5% absolute	SRCA Radiometric Mode Solar Diffuser & SDSM
Above 3.0 μm	1% absolute	Blackbody & Spaceview
Reflectance	2% relative to Sun	Solar Diffuser & SDSM
Spectral		
Center Wavelength	± 1.0 nm	SRCA Spectral Mode
Band-to-Band Stability	0.5% Full Scale 1.0% Half Scale	SRCA Spectral Mode SRCA Spectral Mode
Geometric		
Band-to-Band Registration	0.1 IFOV	SRCA Reticles
MTF	0.3 @ Nyquist	SRCA Reticles

MODIS SCAN CAVITY VIEW

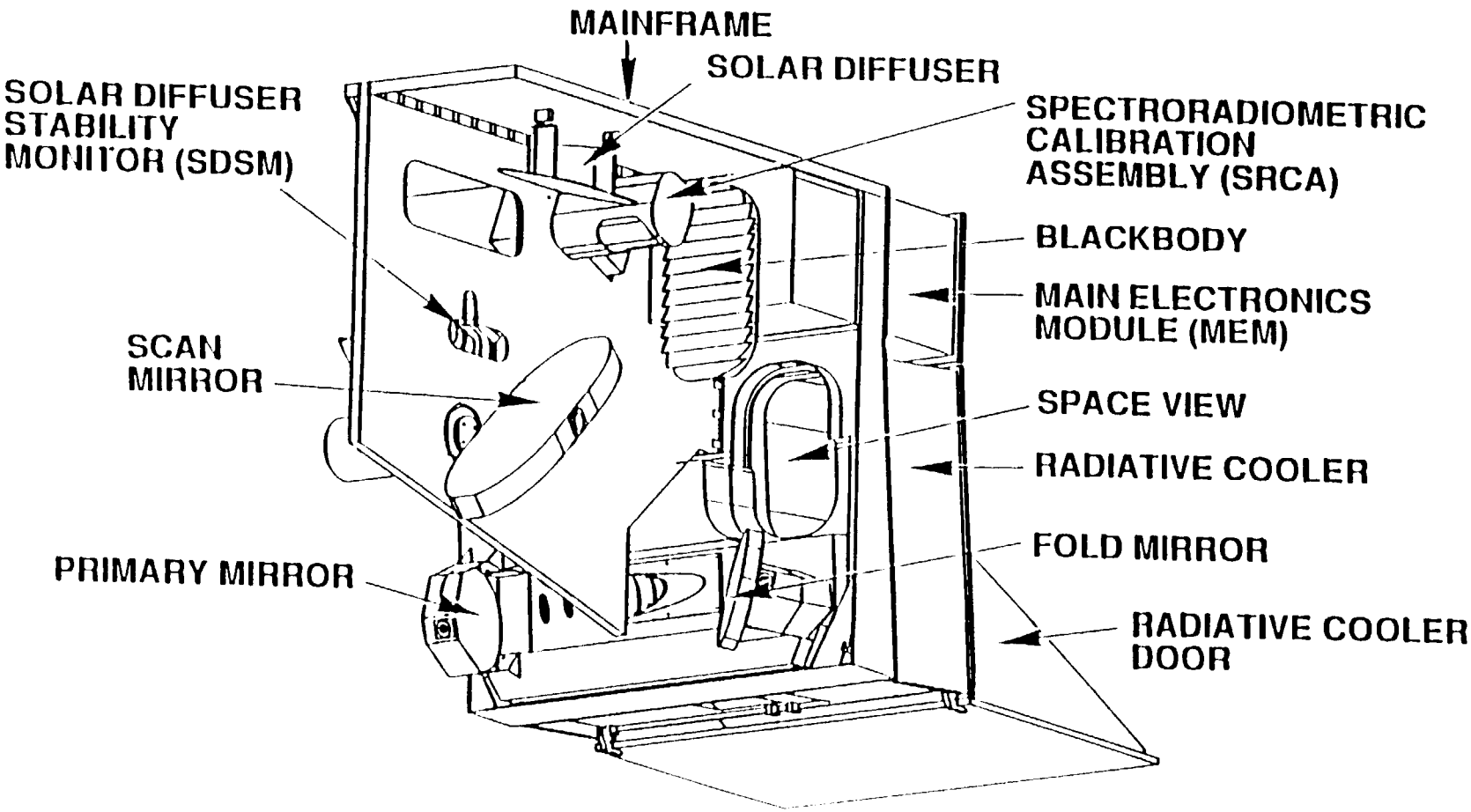

MODIS DATA FROM ONE SCAN

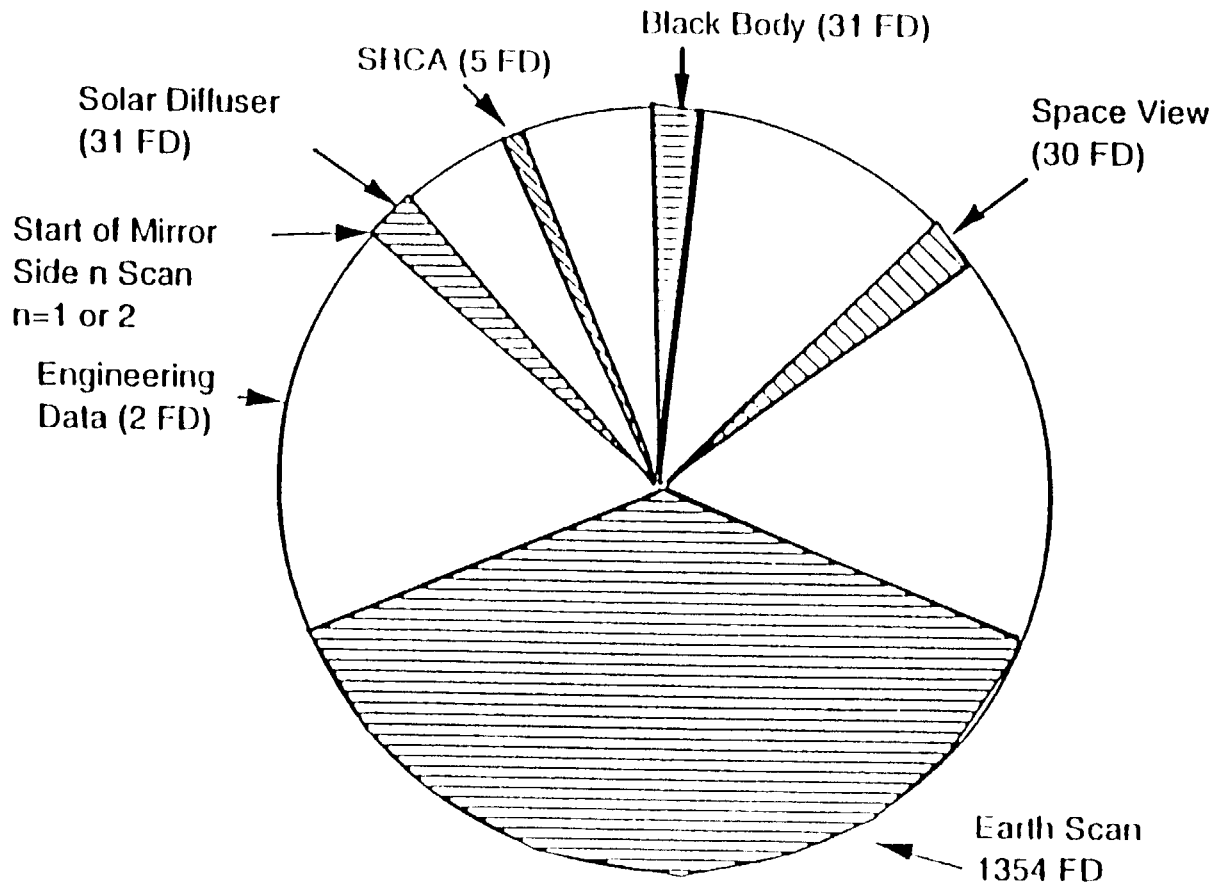

MODIS/MCST Calibration Strategy from 1991/1992 Science Team Meetings

1. Use Alternative MODIS Calibration Methodologies

Several alternative calibration methodologies will be implemented throughout 15-year mission to provide a robust unique "official" calibration algorithm and to allow for its validation by independent methods

2. Characterize Precision on a Time-Scale of Months

Post-launch quantitative characterization and monitoring of the precision (repeatability) with which MODIS at-satellite radiances are measured by various methods will occur within 2 to 6 months

3. Characterize Accuracy on a Time-Scale of Years

Post-launch quantitative characterization and monitoring of the accuracy with which MODIS at-satellite radiances are measured by various methods and on two in-orbit instruments will occur within 3 to 5 years

4. Validate Math Model in 10-15 Years

Validation of the components of the predictive radiometric math models for each MODIS instrument (with an expected life-time of five-six years each) will occur over the fifteen year life-time of EOS mission

Time-Dependent Radiometric Calibration of the Reflective Bands

Time Scale	Calibration Technique	Availability
Within a Scan Line	Scene-dependent MTF inversion	Post-Launch
Within a Scan	Bias Offset measurements Blackbody as DC-restore Space view	At-Launch
	Relative cross-correlation of detectors both within and between bands	At-Launch
Within a Half Orbit	Radiometric rectification over known radiometrically homogeneous sites	Post-Launch
Between Orbits	SRCA in Radiometric mode	At-Launch
Between Days	Solar Diffuser	At-Launch
Between Months	Lunar Pointing	(Not Baselined)
Between Years	Lunar Views	At-Launch
	Radiometric Math Model	Post-Launch*
Validation	Vicarious Measurement Methods aircraft and ground-based	Post-Launch on an intermittant schedule

Direct Lunar Viewing Calibration (Not Baselined)

Requirement: Radiometric Calibration Using Moon

SDSM assumed to provide stability of reflectance-based SD calibration on a time scale of months. On-Orbit Transfer of Absolute Radiometric Source from Solar Diffuser via MODIS detectors to Moon as source.

High Risk Using Spaceport View of Moon

It is assumed that 18-year Phase-Dependent Spectral/Spatial Lunar Radiometric Model from Hugh Keiffer will be available and that it will take approximately 20 to 200 independent lunar half-phase lunar observations to validate the Model and provide for a transfer, which would require require 5 to 50 years using the same MODIS instrument with spaceport observations at a rate of about 4 per year. Since this exceeds the expected five year life of a single MODIS instrument, the transfer cannot occur with required accuracy, if 20 to 200 observations are required.

Low Risk Using Direct View of Moon

It is assumed that 18-year Phase-Dependent Spectral/Spatial Lunar Radiometric Model from Hugh Keiffer will be available and that it will take approximately 10 to 100 independent lunar full-phase lunar observations to validate the Model and provide for a transfer, which would require require 1 to 8 years using the same MODIS instrument with thruough-the-aperature observations at a rate of about 12 per year. Since this is well within the expected five year life of a single MODIS instrument, the transfer can be accomplished with required accuracy, if 10-100 observations is the number required.

Recommention: Have Project do system-level study of feasibility of Monthly Full-Phase Off-Hoizon viewing of the Moon by MODIS in order to provide multi-year multi-instrument MODIS-to-MODIS radiometric cross calibrations for 15-year EOS mission life for continuous calibrated data sets.

MODIS Calibration Interfaces (Context Diagram)

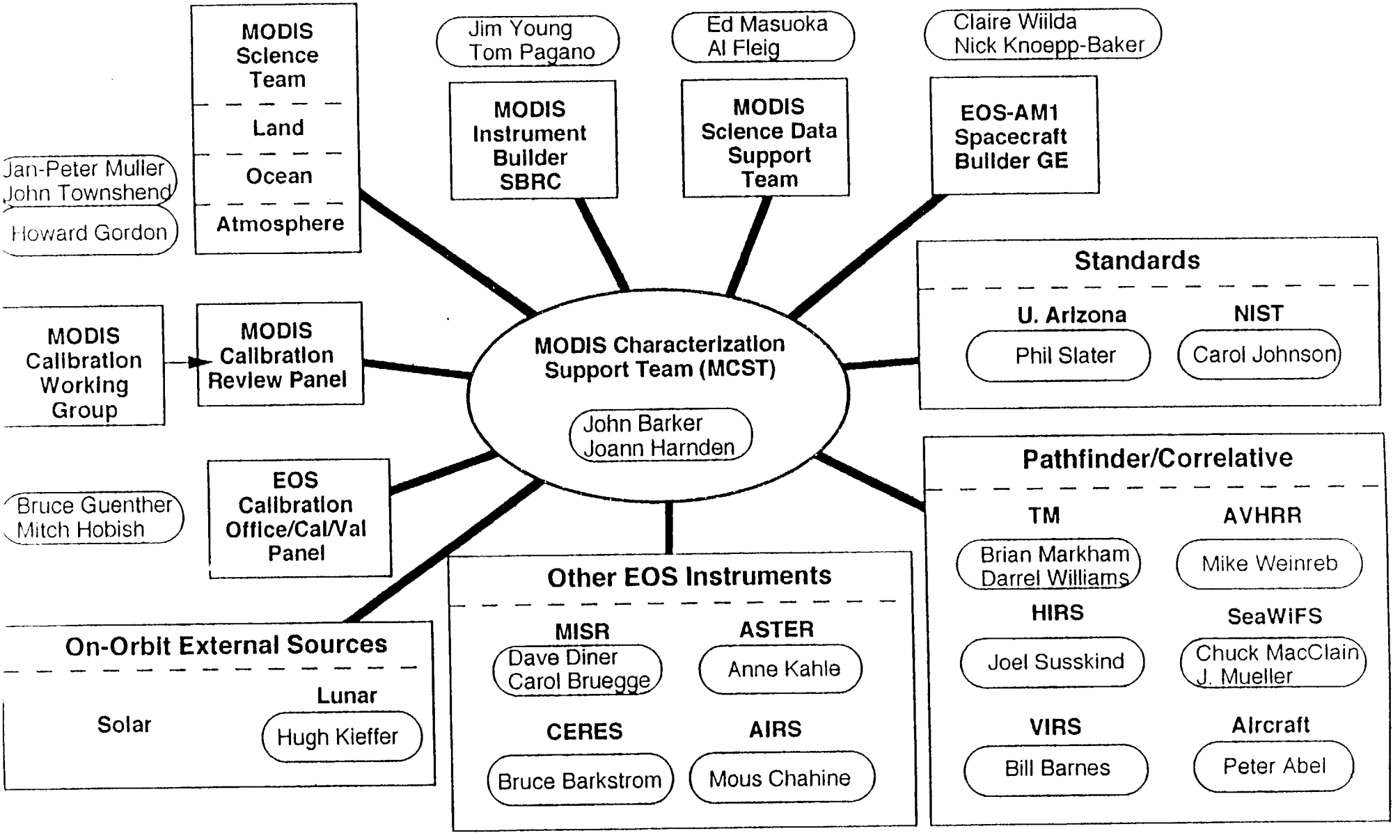

Original (1/17/92) MODIS Band-2 Filter Response and Vegetation Radiance Spectra (TOA)

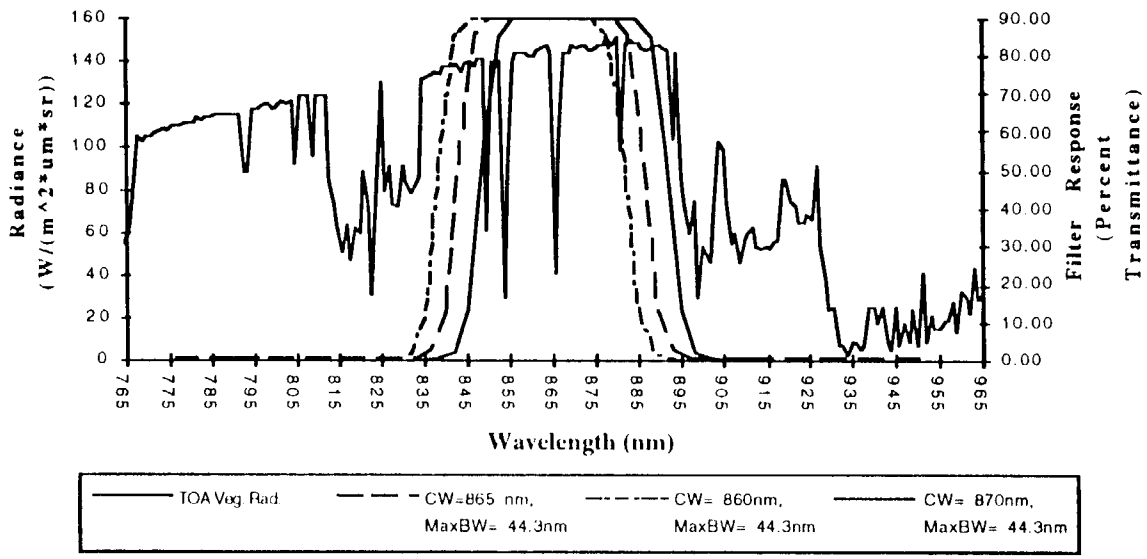

Original Band-2 filter compared to vegetation spectrum Maximum bandwidth case

MODIS Level-1B Calibration Product #3646
Algorithm and Ancillary Data Development Schedule

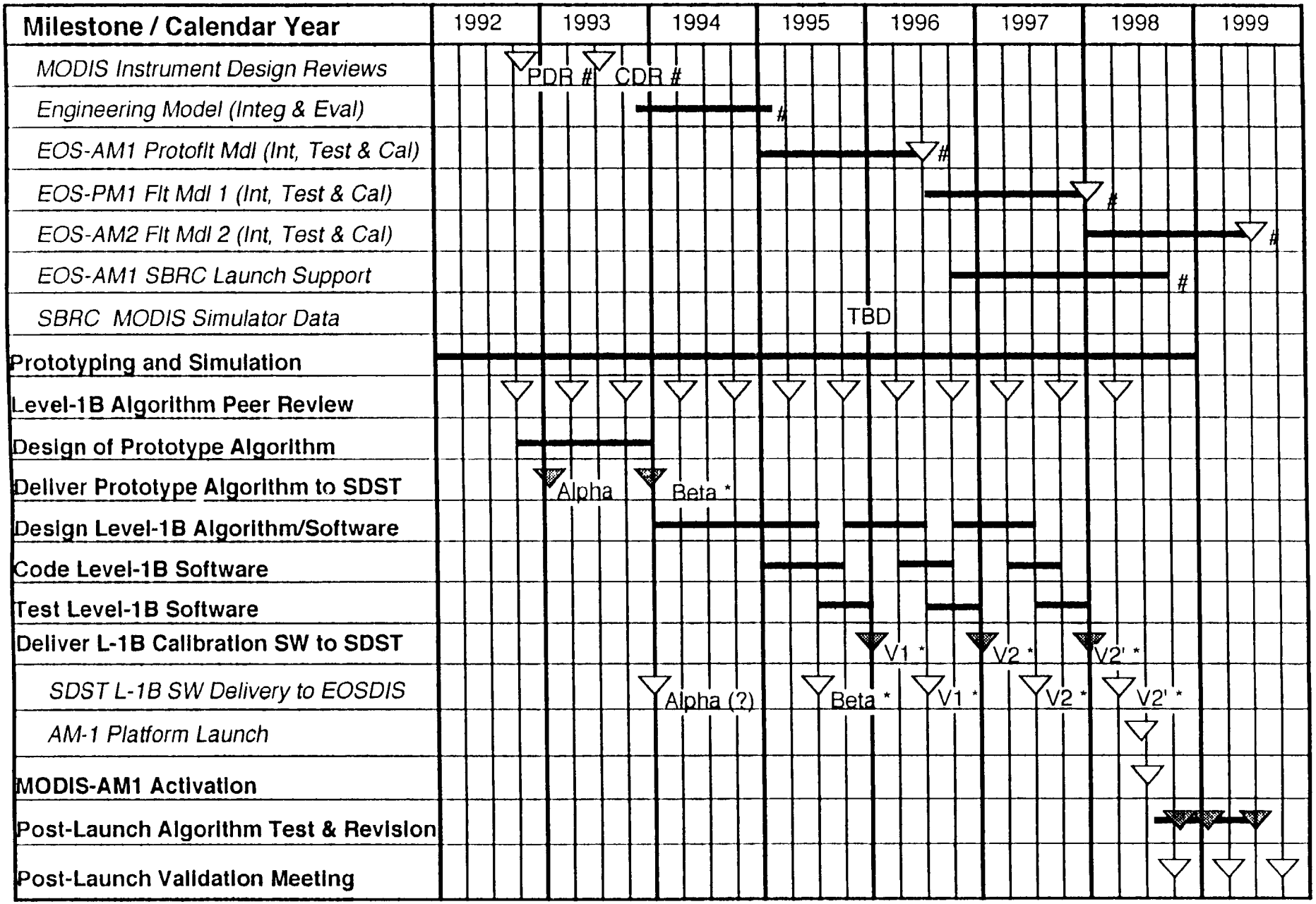

[* From MODIS SDST Schedule, June 11, 1992
From SBRC PRP90-1051C, Figure 3-7, Test Schedule Summary]

Chugach TM 4

Location: Chugach Mtns, AK

Center Latitude: 000
Center Longitude: 000

Path/Row: 000/000
NASA ID: 50518-20372
Satellite: Landsat-5
Instrument: Thematic Mapper (TM)
Acq. Date: 1AUG85
Sun El: 000 AZ: 000
Resampled Pixel Size: 28.5 m
Image Size: 1024.0 x 1024.0 pixels
Scene Size: 29.2 x 29.2 km

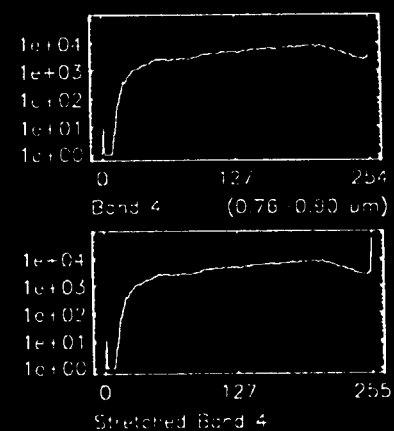

Chugach MODIS 2

Location: Chugach Mtns, AK

Center Latitude: 000
Center Longitude: 000

Path/Row: 000/000
NASA ID: 50518-20372
Satellite: Simulated EOS
Instrument: Simulated MODIS
Acq. Date: 1AUG85
Sun EL: 000 AZ: 000
Resampled Pixel Size: 250.0 m
Image Size: 116.0 x 116.0 pixels
Scene Size: 29.0 x 29.0 km

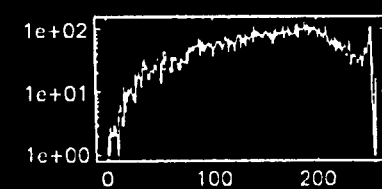

Band 2

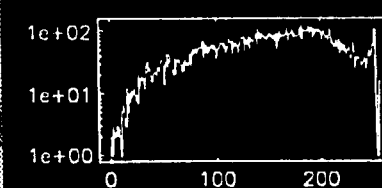

Stretched Band 2

J.L.Barker/J.W.Burcbach
NASA/GSFC/MCST Code 925
Tue Oct 13 12:24:07 1992

MODIS-N Band-to-Ba d Registration Sensitivity

for measuring an NDVI vegetation index over land within a single scene

(MODIS-N Band-to-Band Registration Requirement is 0.1 Pixel)

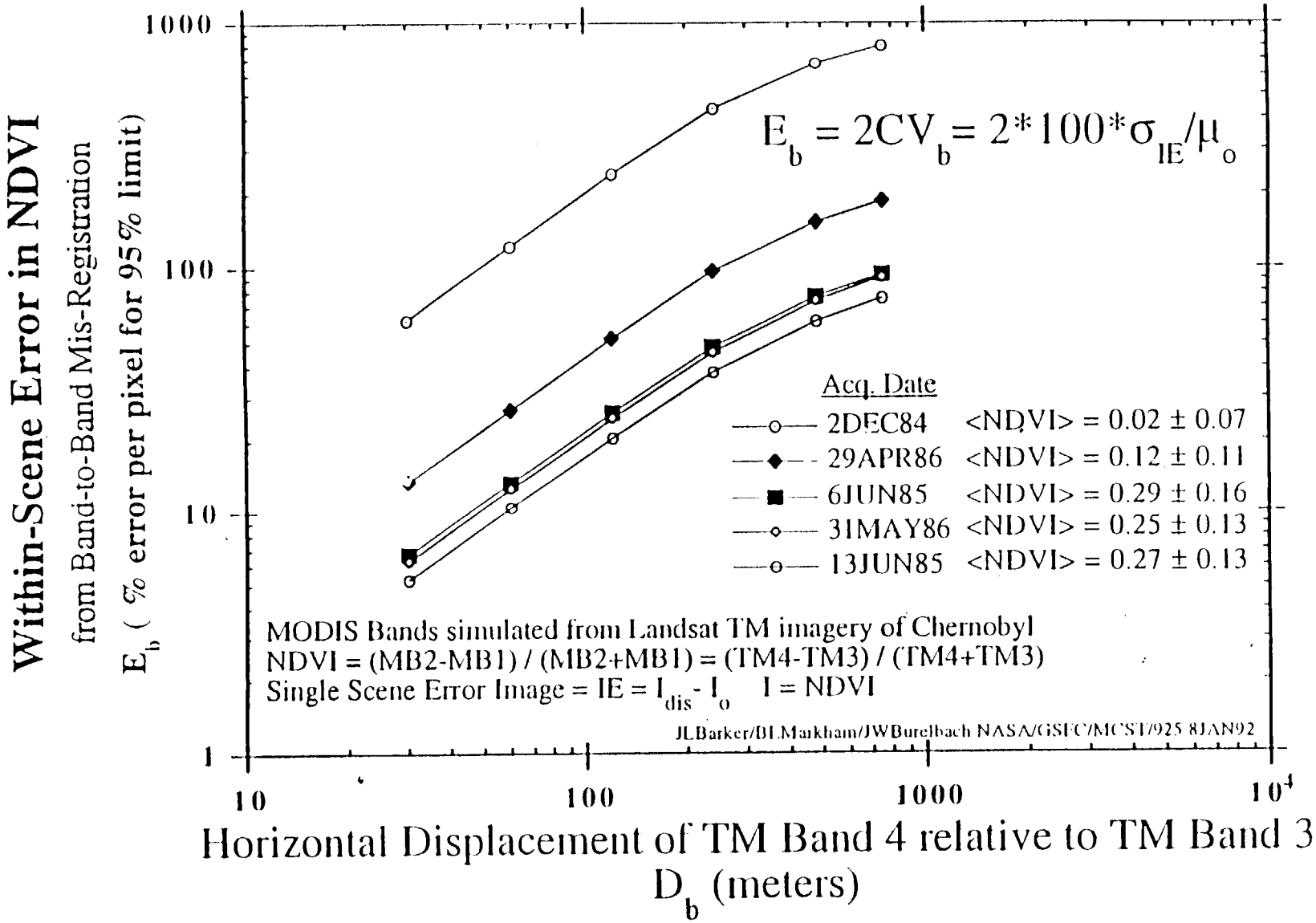

MODIS Band-to-Band Registration Sensitivity

for measuring an NDVI vegetation index over land within a single scene
(MODIS Band-to-Band Registration Requirement is 0.1 Pixel)

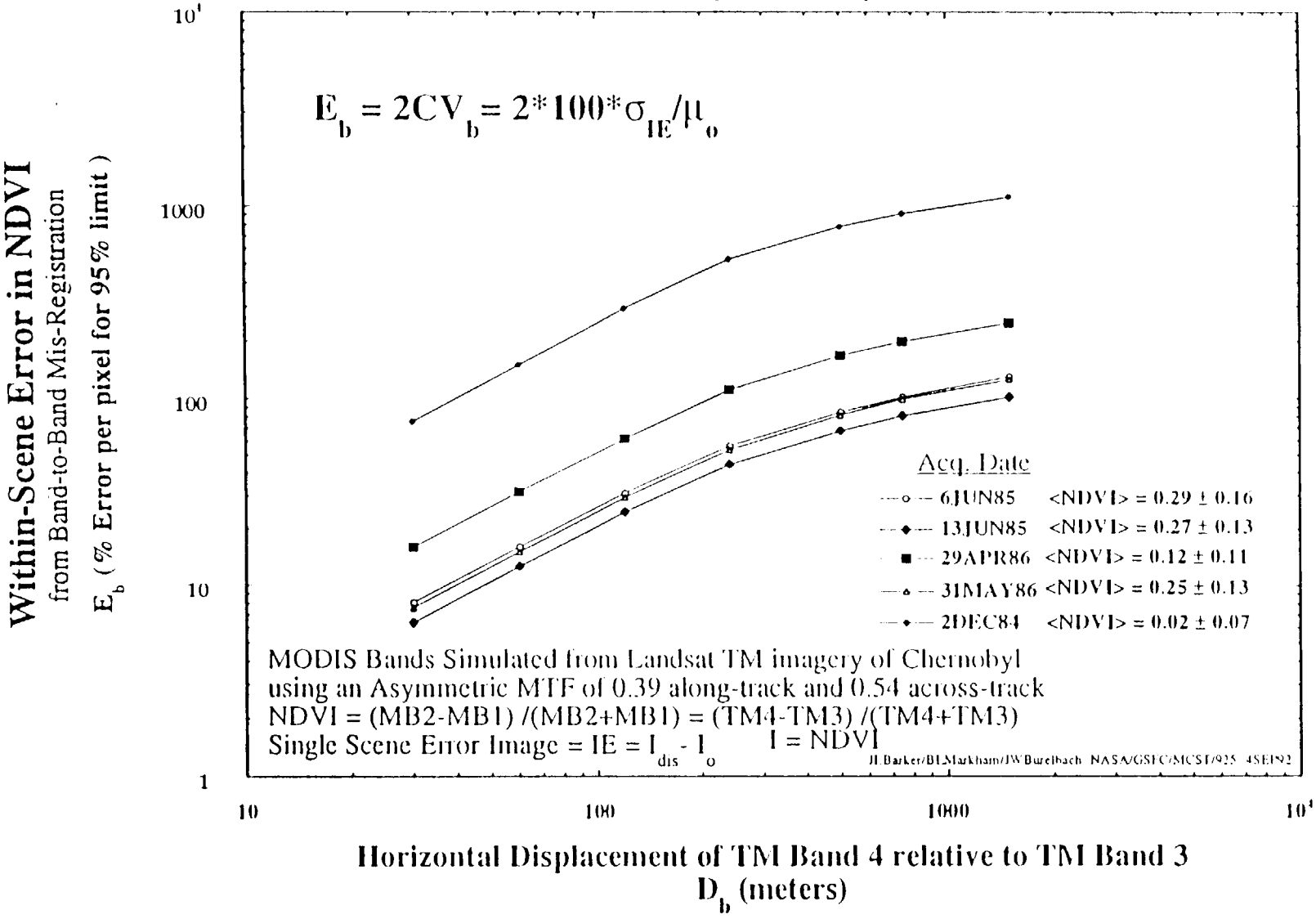

MODIS-N Scene-to-Scene Registration Sensitivity

for measuring a change in an NDVI vegetation index over land between dates

(End-to-End Instrument and Observatory Pointing Knowledge Req. for each scene is 480m at nadir)

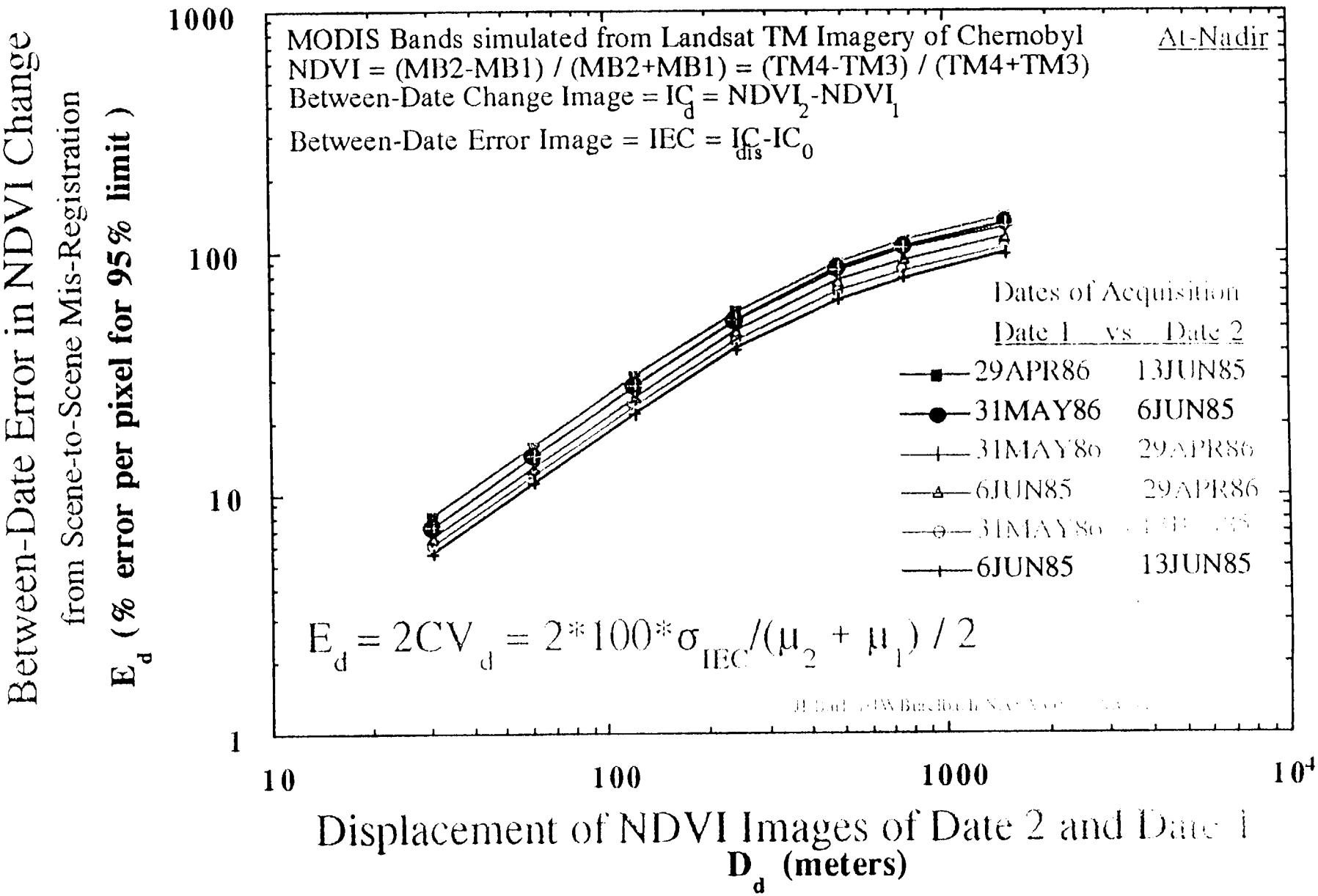

Simulated MODIS-N Sensitivity Studies by MCST

MODIS Scene-to-Scene Registration Sensitivity

for measuring an NDVI vegetation index over land

for examining combined Instrument and Observatory Pointing Knowledge Requirements

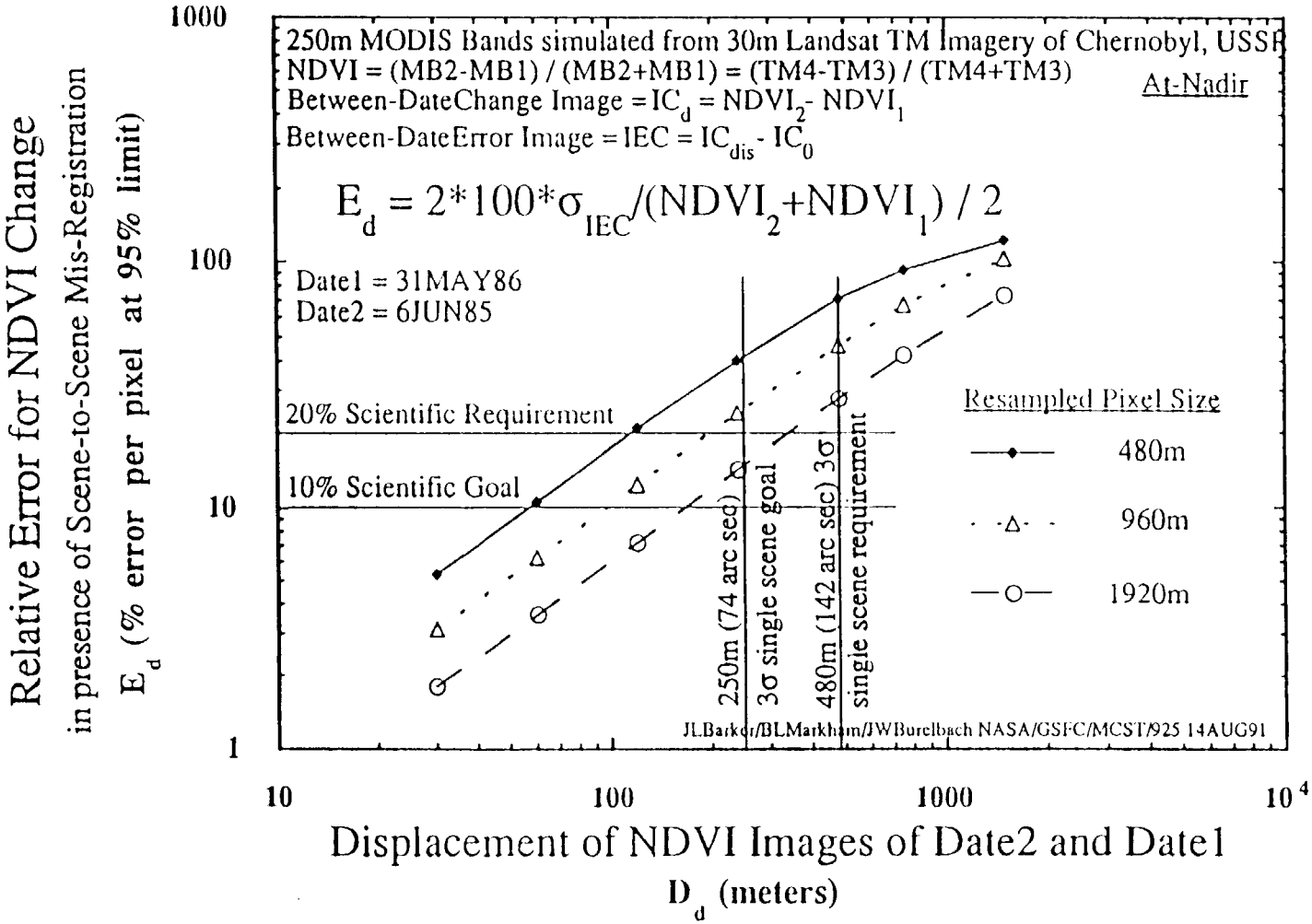

Unpublished Handouts
1 Dec 92
NOAA Science Center

Date	Title	Author(s)	Location	Journal	Journal Abv	Year	Vol	Num Pages	Start Page	End Page	Key Words
27-Nov-92	Airborne Imaging Spectrometer Sensor Characteristics	Dr. Karl Staenz/CCRS/ MPO Susan Till/CCRS	IVOS Subgroup of the CEOS Camp Springs, MD					4			
1-Nov-92	A Multi-Level Electronic Database for Documentaion and Dissemination of Time-Dependent NOAA-AVHRR Calibration Coefficients for the Solar Reflective Channels	P. M. Teillet and B. N. Holben	IVOS Subgroup of the CEOS Camp Springs, MD					10			
23-Nov-92	Report to the IGBP Data Information Systems (DIS) Land Cover Working Group on the 6th CEOS Cal/Val Working Group Meeting (WGCV6), November 23-25, 1992	P. M. Teillet, CCRS	IVOS Subgroup of the CEOS Camp Springs, MD					4			
24-Nov-92	IGBP-DIS Land Cover Working Group Report to CEOS WGCV7	P. M. Teillet, and J. R. G. Townshend	INPE, Sao Jose Dos Campos, Brazil					11			

Unpublished Handouts
1 Dec 92
NOAA Science Center

Date	Title	Author(s)	Location	Journal	Journal Abv	Year	Vol	Num Pages	Start Page	End Page	Key Words
25-Sep-91	A Calibration System, Using an Opal Diffuser, for the Visual Channels of the Along Track Scanning Radiometer, ATSR-2	P. D. Read, A. L. Hardie, J. E. Magraw, H. S. Taylor, and J. V. Jelley	IVOS Subgroup of the CEOS Camp Springs, MD					7			
1-Nov-92	Geophysical Validation of ATSR Sea Surface Temperatures	I. J. Barton, D. T. Llewellyn-Jones A. J. Prata, and R. P. Cechet	IVOS Subgroup of the CEOS Camp Springs, MD					4			
1-Dec-92	Meeting Minutes, CEOS WGCV IVOS Fall 92 at NOAA Science Center	John Barker	IVOS Subgroup of the CEOS Camp Springs, MD					9			
1-Dec-92	SPOT Papers 1992		IVOS Subgroup of the CEOS Camp Springs, MD					11			
28-Oct-92	Draft Recommendations to the London CEOS Plenary Meeting Adopted by the Participants to the CEOS Data Policy Ad Hoc Meeting	Susan M. Till	IVOS Subgroup of the CEOS Camp Springs, MD					8			

Unpublished Handouts
1 Dec 92
NOAA Science Center

Date	Title	Author(s)	Location	Journal	Journal Abv	Year	Vol	Num Pages	Start Page	End Page	Key Words
1-Dec-92	CEOS Consolidated Report 1992	Susan M. Till	IVOS Subgroup of the CEOS Camp Springs, MD					10			
1-Dec-92	Radiance Calibrations for Advanced Very High Resolution Radiometer Infrared Channels	D. A. Steyn-Ross, Moira L. Steyn-Ross, and S. Clift	IVOS Subgroup of the CEOS Camp Springs, MD	Journal of Geophysical Research	JGR	1992	97	17	5551	5568	
1-Dec-92	Visible and Infrared Optical Sensor Calibration Activities at NOAA/NESDIS	C. R. Nagaraja Rao	IVOS Subgroup of the CEOS Camp Springs, MD					27			

GEOPHYSICAL VALIDATION OF ATSR SEA SURFACE TEMPERATURES

I.J. Barton*, D.T. Llewellyn-Jones**, A.J. Prata*, and R.P. Cechet*
* CSIRO Division of Atmospheric Research, PMB No. 1, Mordialloc, Victoria, Australia
** Rutherford Appleton Laboratory, Chilton, Didcot, Oxon., United Kingdom

ABSTRACT

The Along Track Scanning Radiometer, which was launched on the ERS-1 satellite in 1991, is supplying global sea surface temperature (SST) measurements which are useful for climate research applications. To ensure that the radiometer is able to supply highly accurate estimates of SST, several cruises have been undertaken in Australian waters during which ship based measurements have been compared to those from space. A summary of this intercomparison is given in this paper along with a case study of comparisons between the ship measurements and those made using data from the Advanced Very High Resolution Radiometer (AVHRR) on the NOAA-11 meteorological satellite.

INTRODUCTION

The Along Track Scanning Radiometer (ATSR) is a new generation instrument that was built by a consortium of institutes in the United Kingdom, France and Australia, and was supplied to the European Space Agency for flight on the ERS-1 satellite. The instrument incorporates several novel features which are included to enable a derivation of sea surface temperature (SST) with an accuracy of 0.3K. These features include accurate on-board calibration targets, dual angle scanning of the earth's surface[1] and detectors cooled to 80K using a Sterling cycle cooler developed in the United Kingdom. This last feature gives an equivalent noise temperature of 0.02 to 0.04K on the infrared detectors and enables the signal to be detected using the full 12-bit capability of the instrument. Further details of the instrument design are given by Delderfield et al[2].

The design accuracy of the ATSR means that great care must be taken with the geophysical validation using ground based measurements. The ATSR is designed to measure the surface temperature with an accuracy of 0.3K which is the order of the magnitude of the temperature difference between the top of the thin surface skin layer of the ocean and the water some few millimetres below the surface. Thus ship-based radiometers must be used for validation of the ATSR and not the more conventional techniques used to obtain the temperature of the upper mixed layer of the ocean.

SHIP-BASED MEASUREMENTS

During 1991 two Australian research vessels were used to obtain validation data for the ATSR - the RV FRANKLIN which is operated by CSIRO, and the RV LADY BASTEN operated by the Australian

Tech Team Mtg - 12/3/92

Institute of Marine Science. A case study is presented here from data obtained during a cruise of the LADY BASTEN, and an overall assessment of the ATSR performance is given in a table of results from four different cruises in the Coral Sea.

An infrared radiometer, with similar spectral characteristics to the 11 and 12 μm channels on the ATSR, was mounted on the upper deck railing of the LADY BASTEN so that it viewed the sea surface with an incident angle of 40°. While the vessel was steaming the radiometer viewed partly disturbed water in the bow-wave of the vessel.

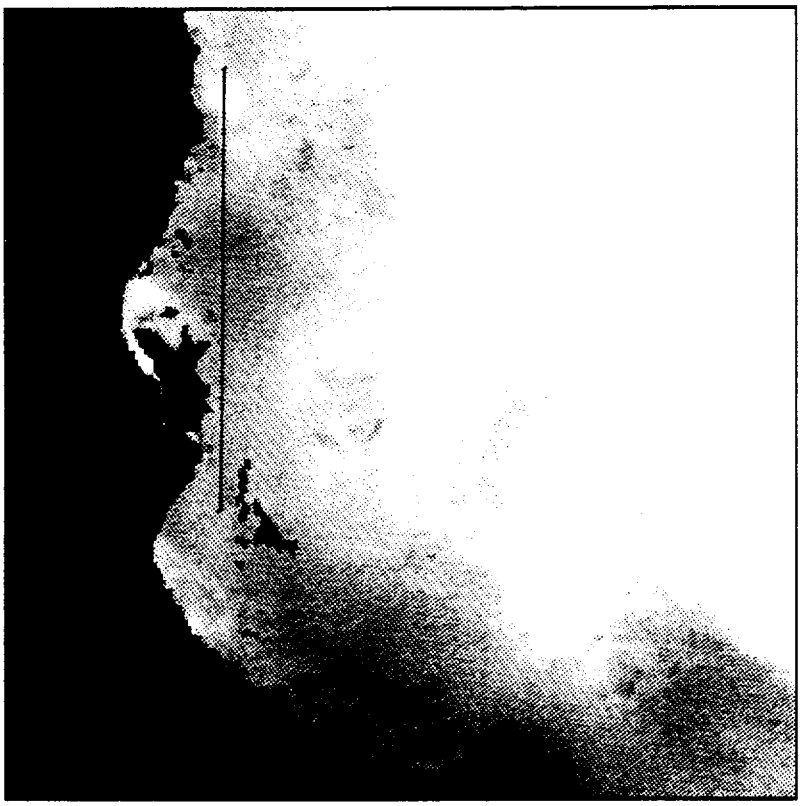

Figure 1: Small area (256km x 256km) ATSR image showing the ship track between 0100 and 0900 local time on September 14, 1991. The centre of the image is 18°13'S, 146°55'E.

The data analysed here were obtained on the night of September 13, 1991. The LADY BASTEN departed from Townsville at 2100 local time (LT) and travelled north towards Cairns. During this night satellite measurements were obtained from the ATSR at 2300 (LT) and the AVHRR on the NOAA-11 satellite at 0200 (LT). Figure 1 shows a 256km x 256 km image from the ATSR 11μm nadir scan with Townsville on the coast near the bottom of the image. From 0100 (LT) to 0900 (LT) the next morning the ship travelled along the line drawn in Figure 1. Temperature measurements along the ship track are shown in Figure 2. The ATSR brightness temperatures for the nadir and forward views in the 11 μm channel are shown to be near 21°C and 19°C respectively. The AVHRR 11μm temperature is close to that in the ATSR forward view as the AVHRR data were from the edge of the swath where the incidence angle is close to that of the ATSR forward view (55° at the surface). The sea surface temperatures derived from both the ATSR and AVHRR data are shown to be in close agreement with the surface temperature measured by the ship-borne radiometer. Prior to plotting, the radiometer data were corrected for the non-unity emissivity of the sea surface and for the reflected downcoming sky radiation.

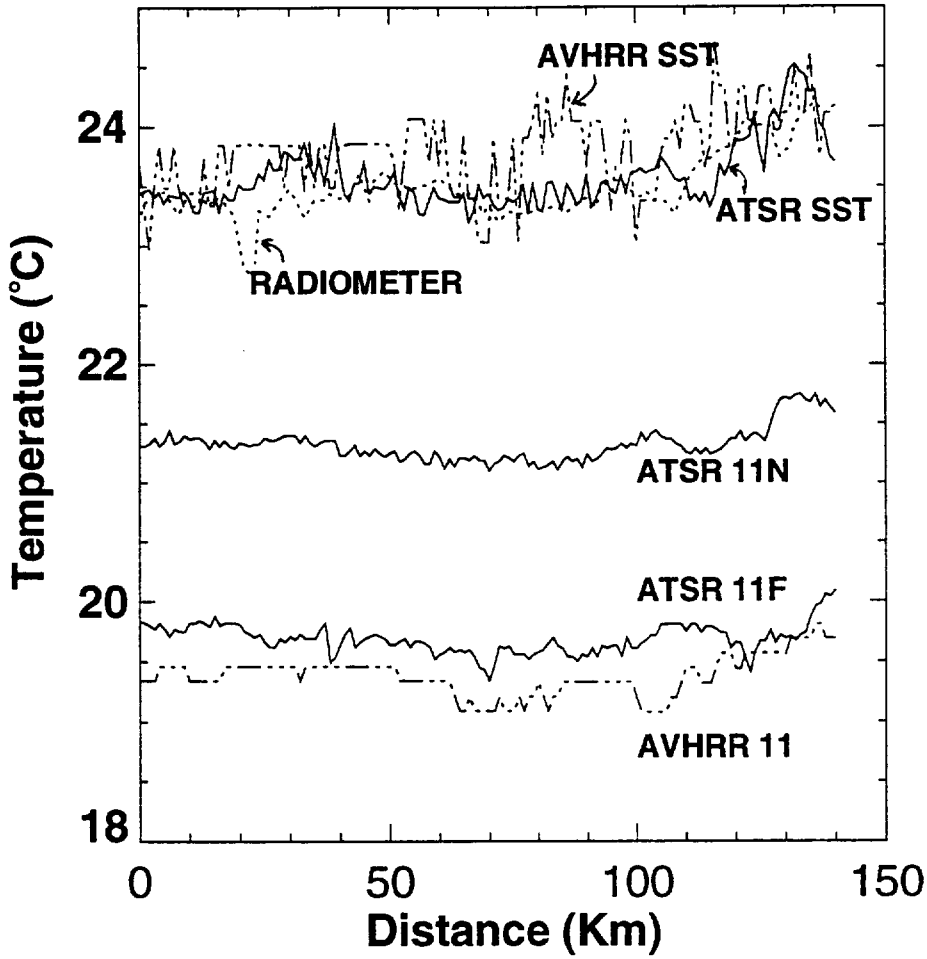

Figure 2: Satellite and surface temperatures along the ship track shown in Figure 1.

A closer examination of the surface temperature data reveals one of the major differences between the SST products from the ATSR and the AVHRR. The latter product is derived using the MCSST algorithm derived from an intercomparison of coincident satellite and drifting buoy measurements and thus is tuned to provide the bulk SST beneath the surface skin layer. In contrast the ATSR algorithm is derived from transmission modelling of the atmosphere and gives the actual skin surface temperature. Under normal conditions the skin layer is 0.2 to 0.5°C cooler than the bulk temperature. This effect can be seen in Figure 2 where the ATSR SST is generally cooler than that from the AVHRR and is also closer to the radiometric measurement of the skin layer. Unfortunately it was not possible to measure the bulk temperature of the ocean surface while the LADY BASTEN was under way.

GENERAL VALIDATION RESULTS

From the four ship cruises in Australian waters we have been able to identify twelve occasions when coincident ATSR and ship data were available for validation. Details are given in Table 1.

FINAL COMMENTS

The results in the table show that the ATSR is obtaining its design accuracy for the measurement of the SST. It also shows that the ATSR measures the skin temperature of the ocean surface and not the bulk

Table 1: Details of coincident ship and satellite measurements. RSST is the ship radiometer measurement of SST, BSST is the bulk temperature measurement, and ATSR is the satellite estimate.

Time GMT	Date 1991	Lat. (°S)	Long (°E)	BSST (K)	RSST (K)	ATSR (K)	BSST-ATSR	RSST-ATSR
1203	5/9	21.54	154.85	296.22	296.00	296.00	0.22	0.00
1257	7/9	18.71	147.22	296.91	296.60	296.61	0.30	-0.01
1315	8/9	24.20	156.92	295.62	295.48	295.41	0.21	0.07
1257	10/9	18.56	147.32	297.52	297.24	297.45	0.07	-0.07
1257	13/9	18.97	146.78	296.54	296.01	296.20	0.34	-0.19
1315	13/9	18.01	147.82	297.86	297.71	297.51	0.35	0.20
1257	16/9	16.71	145.96	297.93	297.47	297.73	0.20	-0.26
2330	21/9	17.07	147.34	298.64	298.46	298.57	0.07	-0.11
1014	22/9	16.09	146.34	298.26	298.11	297.91	0.35	0.20
1219	19/11	30.25	155.18	294.87	294.46	294.73	0.14	-0.27
2301	29/11	28.27	167.16	293.62	293.16	293.37	0.25	-0.21
1148	5/12	23.00	161.72	298.53	298.12	298.20	0.33	-0.08
						Mean error (bias)	0.24	-0.07
						Standard error (K)	0.10	0.17

temperature. The instrument is thus useful for determining energy budgets at the air-sea interface, but should be used with care if the bulk temperature of the ocean is required. Further analysis of global data may lead to a better understanding of the dynamics of the skin layer, and thus allow a wider application of this highly accurate data source.

ACKNOWLEDGEMENTS

The ATSR data are used by courtesy of the European Space Agency. The Rutherford Appleton Laboratory (RAL) processed and provided the ATSR data products. The ATSR SST algorithms were developed before launch by A.M. Zavody of RAL from a theoretical radiative transfer analysis of synoptic atmospheric data provided by the UK Meteorological Office. The Australian Institute of Marine Science provided a berth on their research vessel, and the crews of both the FRANKLIN and the LADY BASTEN are thanked for their support.

REFERENCES

1. Prata, A.J., R.P. Cechet, I.J. Barton and D.T. Llewellyn-Jones, 1990: The Along Track Scanning Radiometer for ERS-1 - scan geometry and data simulation. IEEE Transactions on Geoscience and Rem. Sens., 28, 3-13.

2. Delderfield, J., D.T. Llewellyn-Jones, R. Bernard, Y. de Javel, E.J. Williamson, I.M. Mason, D.R. Pick and I.J. Barton, 1986: The along track scanning radiometer (ATSR) for ERS-1, "Instrumentation for optical remote sensing from space", John S. Seeley, John W. Lear, Andre Monfils, Sidney L. Russak, Editors, Proc. SPIE 589, 114-120.

A CALIBRATION SYSTEM, USING AN OPAL DIFFUSER, FOR THE VISUAL CHANNELS OF THE ALONG TRACK SCANNING RADIOMETER", ATSR-2

ATSR 2
DATE RECEIVED: 25/9/91
DIST: KL/DF/CM/TE/JD/mo/PG/BAe
FILE NO: ER-TN-RAL-AT-2055

PLEASE RETURN TO
JOHN BARKER, CODE 925
NASA/GODDARD SPACE FLIGHT CENTER
BLDG. 22, ROOM 356
286-9498

P D READ, A L HARDIE, J E MAGRAW, H S TAYLOR
Science and Engineering Research Council
Rutherford Appleton Laboratory, Chilton, Didcot, Oxon, UK

J V Jelley
Consultant to Rutherford Appleton Laboratory

ABSTRACT

The ATSR-2 instrument is a successor to the ATSR instrument launched on the ERS-1 satellite on 17th July 1991. ATSR-2, which is currently under construction, will carry two radiometer systems each with their own calibration devices. The long wavelength radiometer operates with four channels in the infra red and provides continuity with ATSR in the global measurement of sea surface temperature. The short wavelength radiometer is additional to the ATSR instrument and uses three channels in the visible and one in the near-IR for the remote sensing of land areas. These additional channels require a calibration device matched to their own spectral requirements and this paper describes the arrangement of this short wavelength calibration system making use of solar radiation.

INTRODUCTION

ATSR-2, primarily an infrared survey instrument carried on the European satellite ERS-2, is essentially a replica of ATSR which has been described in detail elsewhere (Delderfield et al 1985) and (Edwards et al 1990).

Instrumentation used in space based measurements have finite lifetimes and the performance usually degrades with time. Calibration systems are necessary to enable compensation of the gain and sensitivity variations in the instrument to be corrected by direct control or in the measurement data. The short wavelength channels of the ATSR-2 are sensitive to radiance from the ground when it is illuminated by sunlight. The selected wavelengths of these channels are 555, 665 and 865 nm and the calibration system is optimised to cover this wavelength range.

CALIBRATION OF THE VISIBLE CHANNELS, REQUIREMENTS AND CONSTRAINTS

Since the effective colour temperature of light scattered from the ground and atmosphere is comparable to that of the Sun, a separate calibration and monitoring system had to be developed for the three additional pass-bands. The requirements for this visual calibration system (VISCAL) were three-fold. First, the spectrum of the calibrating light source should match that of the radiation scattered from the ground. Second, a flux level was requested which corresponded to around 20% of the maximum signal expected during scans of the ground (e.g. over fresh snow). Third, the source should be forward of the entire optical system, so that any changes in the instrument performance can be monitored and corrected.

Tech Team Mtg - 12/3/92
Attach. #4

Several mechanical, and electrical constraints on the possible choice of a light source and its associated equipment were imposed, since the design of the rest of the ATSR-2 structure had already been frozen. There were basically four constraints:- 1. The addition of the visual channels and VISCAL should not interfere with the IR performance, in particular there should be minimum thermal effect on the structure or on the black-body sources. 2. The addition of the external baffle required for the VISCAL, should not obstruct the microwave link. 3. Power consumption should be kept below 2W, and 4. There should be no mechanical switching of the source.

Choice of Light Source for the VISCAL

In view of the flux-levels and spectral distribution required, it was decided to use sunlight for calibrating the visual channels. Various alternatives were however first considered: these included tritium-phosphor sources, light emitting diodes, Cherenkov radiation from radioactive solutions (Jelley 1958), luminescent panels, fluorescent lights, and filament lamps (both vacuum-tungsten and halogen-tungsten). It was concluded that none of these would have been suitable, for a wide variety of reasons, including spectral matching properties, stability, reliability and power consumption.

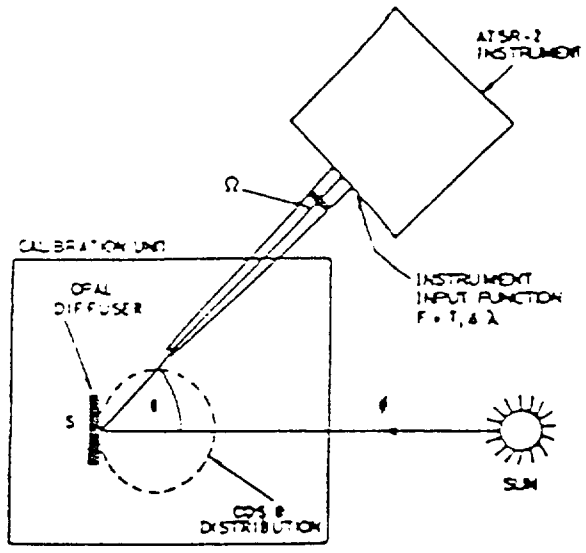

Fig. 1 Principles of an Opal Diffuser Calibration System

A solar radiation-based source has the following advantages over the alternatives:-

1. The spectrum is a close match to that of the ground radiance, 2. The flux is adequate and the source requires no power, 3. The absolute flux-level is known to great accuracy, 4. It is constant except for calculable and predictable corrections, and 5. The system requires only an opal diffuser and two plane mirrors.

The solar intensity has been measured to be constant to within 0.1% (Fröhlich and Brusa 1981) at the mean solar distance and varies only by the ellipticity of the Earth's orbit. This variation, from perihelion (around Jan 4th) to aphelion (around July 5th) amounts to ± 3.4%.

Since the solar flux is far too high for direct illumination of the detectors, it was necessary to devise an attenuator to reduce the intensity by a factor ~ (10^5-10^6). Since it is well established (see Banning 1949) that neutral-density filters cannot be made with densities much in excess of 2, without severe spectral distortion, it was decided to combine Lambertian scattering from the surface of opal (Garforth 1978) and the inverse square law to obtain the necessary attenuation. The system was modelled from an earlier laboratory instrument built at RGO (Jelley 1982) for testing various types of detector at extremely low light levels. The principles are sketched in Figure 1. Direct sunlight illuminates the opal scatterer S at normal incidence, and light scattered at some angle θ is collected within a small solid angle Ω. The light L collected in this cone is given by:-

$$L = (\phi A/\pi).\Omega.\cos\theta.R(\lambda,\theta).T(\lambda).\Delta\lambda \qquad \ldots.(1)$$

where ϕ is the solar flux above the atmosphere, A the illuminated area of the opal, Ω the effective solid angle for the interception of the scattered light, θ the scattering angle, R the Radiance Factor of the opal for the wavelength λ at the angle θ, and $T(\lambda)$ the transmission factor for a filter of bandwidth $\Delta\lambda$.

THE SOLAR CALIBRATION SYSTEM

A schematic of the features of the calibration system is shown in Figure 2, (a) plan and (b) elevation. The regions scanned by the existing ATSR instrument are defined by the baffle B. There are two semi-circular apertures N (nadir view) and F (forward view), and two black-body cavities C_1 and C_2 for calibration of the IR channels. It was found that, by the judicious siting of the opal and a pair of mirrors, a calibration beam could be formed and passed obliquely through the nadir aperture to reach a position where the scan-mirror SM would receive the beam for a portion of its scan.

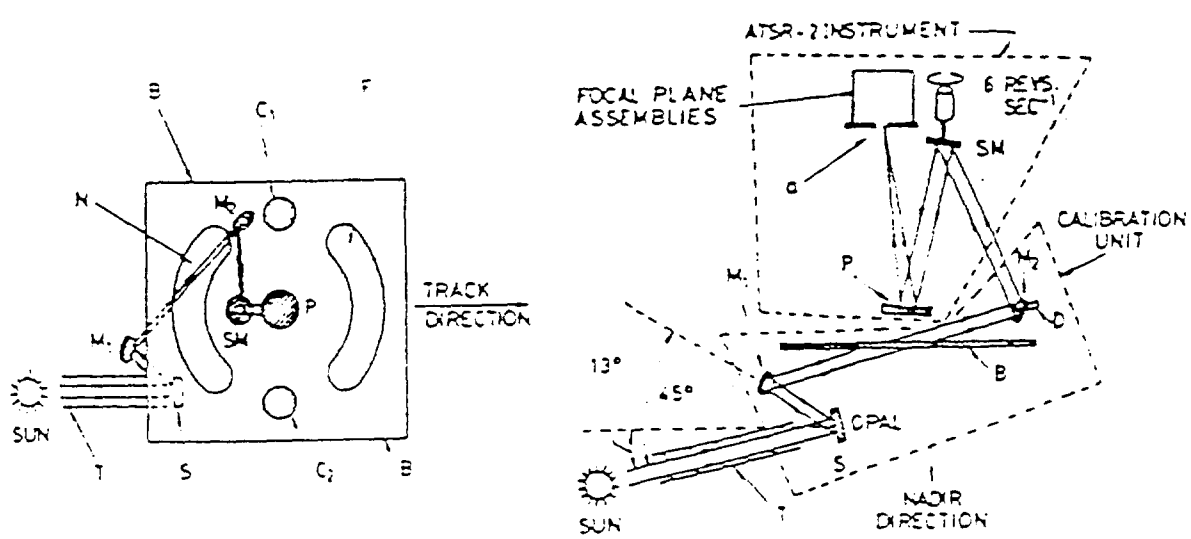

a. Plan

b. Elevation

Fig. 2 Schematic Layout of the Calibration System

The Sun illuminates the opal diffuser S (polished Russian opal type MS20) at normal incidence, via a baffled tube T. Light scattered at 45° is reflected by the two mirrors M_1 and M_2 (one below, and the other above, the plane of B) toward the scan mirror SM. The main off-axis parabaloidal mirror P, then focus the beam through the aperture stop into the detector housing. The area of the opal used is defined by the limiting projected area of M_2, with M_1 and the opal being oversized.

The baffle T restricts the calibration period to 33 seconds on each orbit. M_2 is placed in the view of the rotating scan mirror to allow 16 pixels of the full 2000 to be used for the calibration beam. This occurs close to the time of local satellite sunset, when the Sun is at a dip-angle of 13° to the local horizon, the solar beam then clearing the Earth's surface by ~ 600 km. (Note: A pixel corresponds to 1km square on the ground from the orbital height of 777 km.

During the calibration period with the scan mirror rotating at 6.66 revs.s^{-1}, 219 samples of 16 pixels each are made of the calibration beam on each orbit. This totals 7.7 mins a day for the 105-minute orbital period.

Very small deviations from normal incidence of the sunlight on the opal occur for two reasons:- (1) The sun appears to move in altitude across the baffle for about 1° each side of the normal, during each calibration; and (2), a drift occurs in the azimuth plane, of about ±4.75° due to the equation of time, for the sun-synchronous orbit. Since variations in the angle of incidence to the opal obey a cosine law similar to the Lambertian law for scattered light (Teel 1965), these variations in the extreme case amount to less than ±0.3%.

The Absolute Light-Levels in the VISCAL at the Detectors

Values of ϕ, $R(\lambda,45°)$, $T(\lambda)$ and $\Delta\lambda$ were available or measured for the four channel-wavelengths. By way of an example, we take the case for λ = 555 nm.

ϕ = 188.5 $\mu W\ cm^{-2}\ nm^{-1}$ (from tables by Fröhlich and Wehrli (1981))
$R(\lambda,45°)$ = 0.978 (measured at the NPL)
$T(\lambda)$ = 0.13, where T is the total transmission efficiency of the instrument and $\Delta\lambda$ = 20 nm.
Ω = 1.656×10^{-6} sr (field of view of the instrument 1 km^2 at 777 km altitude)
A = 24.2 cm^2 (used area of the opal: the projected area of M_2).

Inserting these figures in (1), one obtains L = 4.3 nW at the detectors.

The measured noise equivalent power at the detectors = 5.3 pW.
Hence signal to noise = 816
The expected peak signal from the ground radiation = 26.1 nW.
Hence calibration level = 16% of peak.

CHARACTERISATION AND MONITORING

The components of the calibration system have been evaluated for the possible damage effects of gamma, proton and ultraviolet radiation, that may result from the three years in space, and for any fluorescence or phosphorescence effects caused by UV excitation.

A 50mm square of calibrated opal obtained from NPL was sliced into four square quarters for use as samples. One was used as the control and the others irradiated with the gamma, proton and UV radiation. Measurements of the relative and absolute radiance factor efficiency were made before and after each radiation dose at both the centre wavelength of each channel and using broad band white light illumination.

Preliminary results from measurements of the opal efficiency show no measurable change for either proton or UV radiation; these compare favourably to measurements made on alternative materials such as Spectralon, Macor or Pyroceram [Guzman 1991]. The gamma radiation test however resulted in a reduction in the efficiency [Table 1].

Samples of the opal were irradiated using available sources of 1.17 Mev gamma rays at the University of Birmingham and 60 Mev proton radiation available from the Spallation Neutron Source at RAL. The UV radiation test was conducted by illuminating the opal at 254 nm from a high pressure mercury lamp. The total dosage that the opal sample is subjected to was calculated from the solar continuum at 254nm and the 33 seconds of illumination by the sun on each orbit over a three year period.

Table 1 shows the effect on the reflectance factor of the opal caused by gamma radiation, measured at different bandwidths.

TABLE 1

Equivalent orbital period	Three year			Fifteen years		
Gamma Tests:						
Radiation dose	50k rads			250k rads		
Energy	1.17 Mev			1.17 Mev		
Test Data:						
Wavelength (nm)	550	660	870	550	660	870
bandwidth (20nm)						
Decrease in (R) %	17	12.4	9	29	24	19
Bandwidth (300-900nm)						
Decrease in (R) %		11.4			21.3	
Proton Tests:						
Radiation dose	8k rads			30k rads		
Energy	60 Mev			60 Mev		
Both narrow and broadband						
Decrease in (R) %	No measurable change			No measurable change		
UV Radiation Test:						
Wavelength	254 nm			254 nm		
Intensity	85 microwatt/cm^2			85 microwatt/cm^2		
Duration	6 Days			30 Days		
Both Narrow and Broadband						
Decrease in (R) %	No Measurable change			No measureable change		

Phosphorescence and Fluorescence

Phosphorescence of the opal was investigated by illuminating a sample from a switched mercury UV lamp and measuring the residual radiance after the lamp was switched off. A radiometer with a sampling period of 0.5 seconds was used for the measurement and no phosphorescence was detected, the radiance falling to the background level after about one second. (In comparison the solar input to the opal will be vignetted within 10 seconds by the solar baffle on each orbit).

Fluorescence was investigated by illuminating the opal with the 254 nm mercury source and measuring the radiance from the surface over the wavelength range 350 to 1100 nm with and without the UV radiating component. Fluorescence was detected at a level of 0.6% of the equivalent scattered UV radiance from the opal. Although this effect is small when the UV content of the solar continuum is used there may be significant effects from non-thermal radiation such as the highly energetic Lyman alpha radiation at 125 nm.

Furthermore, since these non-thermal emissions are not predictable, a decision was made to reduce any likely effect of fluorescence on the calibration system by including a UV blocking glass window ahead of the opal.

UV Blocking Window

A 3 mm thick uncoated Schott window of BK7G25 is mounted ahead of the opal. The glass has a short-wavelength cut-off of 300 nm but a high transmission efficiency from 500-1700 nm which covers the calibration bandwidth. A sample window was subjected to radiation and fluorescence tests, as for the opal, and the transmission measurements inclusive of surface reflection effects are shown in Table 2. The features show a reduction in efficiency which also has a colour component.

TABLE 2

Percentage Transmission of BK7G25 after Radiation

Radiation Energy	Radiation Dose (Rads)	Wavelength nm 550	670	870	1600
Unirradiated		91.8	92.5	93.5	93.9
Gamma (g) 1.17 Mev	15K(g)+ 4K(p)	89.6	91.2	92.8	93.8
Proton (p) 60 Mev	30K(g)+ 8K(p)	86.9	89.8	92.5	93.7

Photodiode Monitor

Both the gamma radiation effect on the opal efficiency and the degradation in the window transmission indicates the need of a monitor in the calibration beam that will show any small slow changes. The calibration data from the monitor can be used in conjunction with data from the detectors for analysing changes in the channel sensitivities.

The monitor will take the form of an unfiltered radiation-hardened silicon photo diode placed behind a 2 mm diameter aperture in the centre of the second mirror M2 (fig. 2). The intensity of the calibration beam over the full bandwidth is recorded to an accuracy of 0.1%, and will measure the predictable changes already described as well as the unpredictable characteristics.

CALIBRATION ACCURACY

Combining the data from the broadband monitor and from the detectors with their wavelength information systematic variations in the channel sensitivities can be analysed and the data corrected.

Absolute calibration level will be known to an uncertainty of ± 5%, and the relative orbit to orbit calibration will be known to ± .1%.

Additional Calibration Aids

In addition to flying a constant absolute calibration system a comparison with ground data from uniform areas of sand or snow will further improve the accuracy of the data from the ground. Such areas are the arctic regions and white sands in New Mexico and the uses of such a comparison are being evaluated.

Future Test

In addition to the Space Qualification Procedure there are scheduled polarisation measurements on the opal and, a radiance measurement using direct solar illumination of the complete system.

REFERENCES

Banning M. (1947). J. Opt. Soc. Am. 37, 686.

Delderfield J. et al (1985). Proc. SPIE. Vol. 589 114-120.

Edwards T. et al. (1990). Journ. Brit. Interplanetary Soc. 43, [4], 160.

Frölich C. and Brusa R.W. (1981). Solar Phys. 74, [1] 209.

Frölich C. and Wehrli C. (quoted in Table 3.3.2 in "Introduction to Solar Radiation", by Muhammad Iqbal. Academic Press 1983, pp46, 47).

Garforth F.A. (1978). Proc. SPIE Vol. 146, 49.

Guzman C.T. et al (1991). Proc. SPIE Vol. 1943-14

Jelley J.V. (1958). Cherenkov Radiation and its Applications, Pergamon Press, London p 245

Jelley J.V. (1982). Observatory, 102, 30.

Teel. R.P. (1965). Chap 1 "Photometry" in Applied Optics and Optical Engineering Vol. 1 (ed. R. Kingslake) Academic Press, New York.

JOURNAL OF GEOPHYSICAL RESEARCH, VOL. 97, NO. C4, PAGES 5551–5568, APRIL 15, 1992

Radiance Calibrations for Advanced Very High Resolution Radiometer Infrared Channels

D. A. STEYN-ROSS AND MOIRA L. STEYN-ROSS

Physics Department, University of Waikato, Hamilton, New Zealand

S. CLIFT

CSIRO Marine Laboratories, Hobart, Tasmania, Australia

We examine in detail the calibration procedures for the advanced very high resolution radiometer (AVHRR) infrared channels. The AVHRR literature states that the linear mapping used to convert radiometric count to scene radiance is satisfactory for channel 3, but is only approximately correct for channels 4 and 5 since these channels have a slight curvature in their respective radiance-versus-count response functions, so a nonlinearity correction (NLC) is applied. Traditionally, these adjustments have been tabulated as brightness temperature corrections; we find that when expressed as radiance corrections, the NLCs can be written in a particularly simple form which depends only on the temperature of the internal calibration target. This new formulation eliminates the need to interpolate within the tables of temperature NLCs and permits the correction to be applied prior to conversion to equivalent brightness temperature, rather than after. Examination of the calibration records for 48 NOAA 11 passes sampled over a full year revealed several significant features: (1) For low Sun elevation angles relative to the satellite, sunlight can apparently leak into the optical path of the AVHRR, distorting the in-flight calibration data for channel 3, producing errors in apparent scene temperature as large as 2°C. (2) There is a clear demarcation between the calibration slopes for day and night operation of the satellite. (3) The thermal step that occurs when the spacecraft crosses the night-day boundary into full sunlight leads to transient calibration errors which decay to zero with a time constant of about 40 s. At the peak of the transient, the apparent scene temperature can be depressed by over 1°C in channel 3, and by up to 0.4°C in channels 4 and 5. Quality control measures and techniques for compensating for calibration problems are discussed.

1. Introduction

The advanced very high resolution radiometers (AVHRRs) flown on the NOAA series of polar-orbiting satellites sense visible and infrared radiation reflected by and emitted from the Earth. The NOAA 9, 11 and 12 satellites carry a five-channel AVHRR: channels 1 and 2 work over two intervals within the visible spectrum, channel 3 responds in the near infrared (nominally 3.5–4.0 μm), while thermal infrared emissions are detected by channels 4 and 5 (10.5–11.5 and 11.5–12.5 μm, respectively). NOAA 10 lacks a channel 5 sensor. The filter functions for channels 3, 4, and 5 for NOAA 11 are shown in Figure 1.

Since 1985 the CSIRO (Commonwealth Scientific, Industrial, and Research Organisation) Marine Laboratories in Hobart, Australia, have been systematically receiving and processing AVHRR data to estimate sea surface temperatures and vegetation indices and are currently developing cloud retrieval algorithms. Essential to algorithms involving the infrared measurements are accurate values for radiance, which implies that there must be a well-defined and consistent calibration procedure. By calibration we mean, How does the radiometer's digitized output value (or count) relate to the actual radiance of the observed scene? In principle, if the radiometer were perfectly stable, one could perform the necessary calibration experiments on Earth prior to launch to establish the precise and permanent relation between counts and radiance/brightness temperature. The resulting transfer function could then be used for all subsequent in-flight measurements. However, because the characteristics of the on-board sensors and electronics may drift with time and environmental changes, they need to be regularly recalibrated while in service. We describe this in-flight testing process as "dynamic" calibration in which changes in instrument response are automatically tracked and corrected.

The in-flight calibration of the AVHRR infrared channels proceeds by monitoring the radiometer output when it views two targets whose radiance is known or can be computed: deep space serves as a zero-radiance reference and an internal "blackbody" calibration target (ICT) which is located in the instrument baseplate, and whose temperature is measured with a cluster of four platinum-resistance thermometers (PRTs), provides the second reference. These two measurements are used to define a continuously updated linear mapping from count to radiance. For channel 3, this linear form is satisfactory; however, channels 4 and 5, whose detectors have a nonlinear radiance-versus-counts response, require a nonlinearity correction (NLC). These corrections traditionally have been tabulated in temperature space; however we feel that since radiance is the fundamental physical quantity measured, the corrections are more naturally stated in radiance space. Furthermore, some algorithms, for example cloud retrieval, require corrected scene radiances rather than brightness temperatures. In order to produce the corrections in radiance space, we transform the NESDIS (NOAA National Environmental Satellite, Data, and Information Service) brightness temperature corrections as tabulated by *Weinreb et al.* [1990]. When the resulting radiance corrections are plotted as a function of apparent scene radiance, we discover that the NLCs can be expressed in a particularly simple form.

Copyright 1992 by the American Geophysical Union.

Paper number 91JC03055.
0148-0227/92/91JC-03055$05.00

Tech Team Mtg-12/3/9

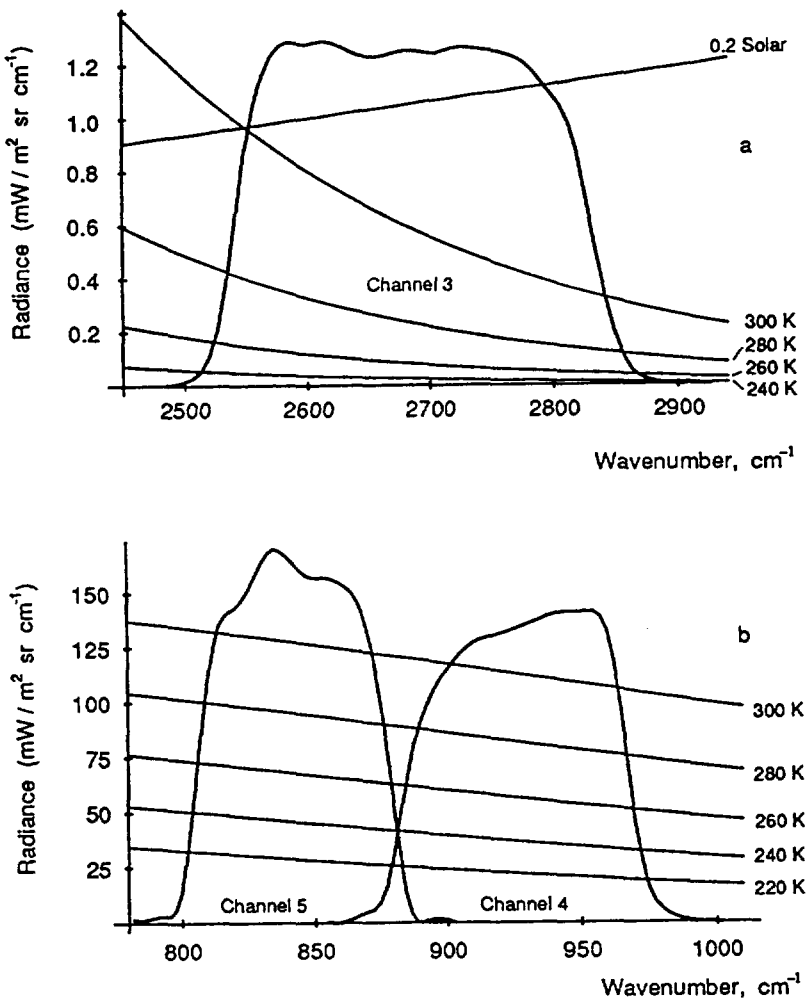

Fig. 1. Channel filter functions for NOAA 11 plotted in wavenumber (inverse centimeter) space. The superimposed family of curves show the variation of blackbody radiance at each of the specified temperatures across the width of the filter function (the filter functions have been arbitrarily scaled vertically for convenient display). (*a*) Channel 3 filter. The single rising curve represents 20% (factor chosen for convenience of comparison with the other curves) of the solar radiance at the top of the atmosphere, and assumes the Sun is a blackbody radiating at 5800 K. Clearly, solar contributions cannot be neglected for channel 3 (this has implications for inflight calibrations of this near-infrared channel; see discussion in the text). (*b*) Filter functions and sample blackbody radiances for channels 4 and 5. Solar contributions are negligible across these thermal infrared channels.

The NESDIS nonlinearity correction tables (in temperature space) are calculated from data obtained in the prelaunch experiments at ITT Aerospace/Optical Division, as described by *Weinreb et al.* [1990]. These experiments produce, for each channel and for three different baseplate temperatures, the fundamental calibration curve of radiance versus AVHRR output in digital counts. A sample radiance-versus-count curve is shown in Figure 2. The graphs for channels 4 and 5 show a slight curvature, of approximately quadratic nature. The nonlinearity corrections are obtained by subtracting a linear approximation from the curved form. Use of the corrections is based on the assumption that they are invariant with time so that what applied in the laboratory will therefore apply in flight.

To check the quality and stability of the in-flight calibrations, we examined the calibration records for 48 NOAA 11 passes sampled at monthly intervals over a full year (two daytime passes and two nighttime passes for each month). Our examination revealed several surprising and significant features. In 16 of the 24 daytime passes, the channel 3 count-versus-ICT-temperature calibration curve displayed consistently large but spurious deviations away from the expected trend, caused, we conjecture, by sunlight leaking into the optical path. If this extraneous radiation is not corrected for, the apparent scene temperature in channel 3 may be lowered by as much as 2°C. With the exception of the four (southern hemisphere) summer months November through February, solar corruption of the channel 3 ICT data seems to be a regular daytime event at our Hobart ground station (latitude 43°S).

We also found that the calibration slope (change in radiance per change in count; g in equation (2)) for all three infrared channels showed clear demarcations between day and night operation. It might be hoped that the dynamic calibrations will completely compensate for these day-night variations. However, when the satellite crosses the night-day boundary into full sunlight, it experiences a thermal step. The ICT temperature rises rapidly, and the radiometer counts decline steeply; it takes almost 3 min for the temperature to stabilize to the new value. During this period the dynamic calibrations are only partially successful at tracking the thermal changes, producing significant deviations from the anticipated calibration trend which persist for about 40 s following the transi-

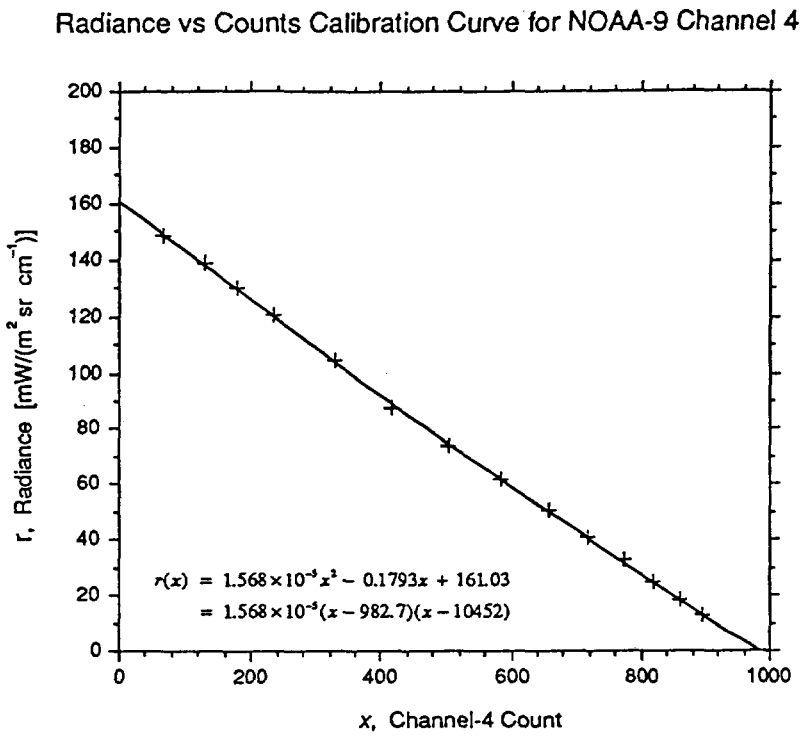

Fig. 2. Appproximate calibration curve for channel 4 of NOAA 9 AVHRR (measured from Fig. 1 of *Weinreb et al.* [1990]). The least squares parabola fitted to the data has been factorized to show the form $r(x) = a(x - \mathrm{SC})(x - \gamma)$, where SC and γ are the roots of the quadratic. Knowledge of the curvature a enables a simple expression to be written down for the correction when approximating the curve with a two-point-calibration straight line passing through the space count, SC.

tion. These instabilities appear to be due to lags in the PRT responses resulting from the finite thermal conductivity of the ICT material. Uncorrected, the apparent scene temperature could be momentarily lowered by as much as 1°C for channel 3, and 0.4°C for channels 4 and 5. This syndrome affected all 12 of the sampled night passes within the 6-month interval October through March.

In section 2 we describe the standard calibration method which converts AVHRR count to radiance via a linear mapping. In section 3 we argue that the application of the nonlinearity corrections is considerably simplified when the correction is stated in radiance space rather in temperature space as has been tradition. We present the results of our examinations of in-flight data for NOAA 11 in section 4, and in section 5 we list recommendations pertinent to quality control of AVHRR calibrations.

2. CONVERTING AVHRR COUNTS TO RADIANCE

As part of the preflight calibrations procedures, NESDIS establishes a least squares polynomial which maps t, the PRT output count, to absolute temperature T. The individual PRT temperatures are then averaged to obtain the mean ICT temperature. For NOAA 11 and 12, the polynomial is the quadratic

$$T = 276.60 + 0.051275t + 1.363\times10^{-6}t^2 \qquad (1)$$

Weinreb et al. [1990] describe how the constant term will have been adjusted, if necessary, so that (1) gives the brightness temperature of the ICT, rather than its physical or thermodynamic temperature. This modification to the polynomial effectively eliminates systematic errors arising from nonblackness of the ICT blackbody, so that thereafter the emissivity of the ICT can be assumed to be unity. The actual emissivity of the ICT is estimated to be better than 0.994 [*Weinreb et al.*, 1990].

All analog measurements are converted to digital counts. The satellite broadcasts the PRT temperature and the radiometric data for the space-views and the internal target views for channels 3, 4, and 5 as part of each scan line. Thus for a typical 14-min overpass of 5000 lines there will be 5000 calibration sets for each channel, enabling the ground station to monitor calibration changes during this period.

Figure 3*a* illustrates the standard NESDIS calibration method, which assumes that the count-to-radiance mapping is a straight line passing through the space count SC on the x axis (deep space has essentially zero radiance in the infrared), with slope $g = R/(\mathrm{IC} - \mathrm{SC})$. IC is the channel count when the sensor viewed the internal target, and R is the total radiance of the target at temperature T received by the sensor. We may thus express the (linear) conversion from AVHRR count x to (linear) scene radiance $r_{\mathrm{lin}}(x)$ as follows:

$$r_{\mathrm{lin}}(x) = \frac{R}{\mathrm{IC} - \mathrm{SC}}(x - \mathrm{SC}) = gx + h \qquad (2)$$

We refer to g as the "calibration slope" with units of radiance per count; h is the intercept on the radiance axis. We calculate R by integrating the Planck blackbody expression $B(\nu, T)$ across the channel filter function $\phi(\nu)$:

$$R = \frac{\int_{\nu_1}^{\nu_2} B(\nu,T)\phi(\nu)d\nu}{\int_{\nu_1}^{\nu_2} \phi(\nu)d\nu} \qquad (3)$$

where ν_1 and ν_2 are respectively the lower and upper wavenumber limits of the filter function. The Planck equation expressed in wavenumber space is

$$B(\nu,T) = \frac{c_1\nu^3}{e^{c_2\nu/T} - 1} \qquad (4)$$

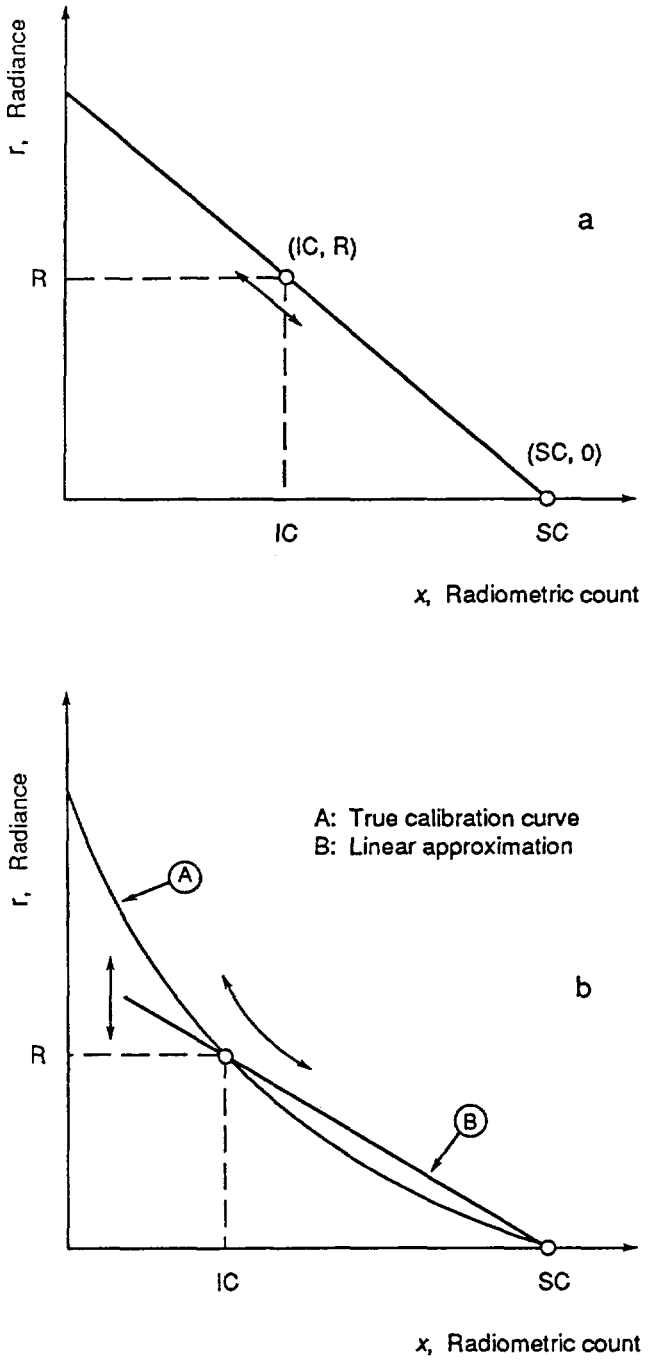

Fig. 3. AVHRR calibrations are derived from two reference views. The space view fixes the zero-radiance reference; the ICT view defines a second point on the true calibration curve. Because the ICT temperature varies, this second point moves up and down the calibration curve, and thus the size of any nonlinearity corrections to be applied also varies. (*a*) For channel 3, the detector response is linear, so a two-point calibration fixes the counts-to-radiance mapping unambiguously. (*b*) Channels 4 and 5 have a curvature whose deviation from a linear fit can be compensated for by applying tabulated nonlinearity radiance corrections. (Based on Fig. 3 of *Weinreb et al.* [1990].)

with c_1 and c_2 being the first and second radiation constants scaled to give radiance units of $\mathrm{mW/(m^2\,sr\,cm^{-1})}$:

$$c_1 = 2hc^2 \times 10^{11} = 1.1910439 \times 10^{-5}\ \mathrm{cm^3\,mW/(m^2\,sr\,cm^{-1})}$$

$$c_2 = hc/k \times 10^2 = 1.438769\ \mathrm{cm\,K}$$

where h, c, and k are respectively Planck's constant, speed of light, and Boltzmann's constant. It should be noted that these values for the two radiation constants, which are derived from the 1986 CODATA Recommended Values of the Fundamental Physical Constants [*Cohen and Taylor*, 1987], differ by a few parts per million from those quoted in the NESDIS literature [*Lauritson et al.*, 1979; *Planet*, 1988], namely:

$$C_1 = 1.1910659 \times 10^{-5}$$

$$C_2 = 1.438833$$

NESDIS tabulates each infrared filter function at 60 evenly spaced wavenumber increments $\Delta\nu$. The table entries are normalized so that the area under the filter curve (i.e., the denominator in equation (3)) is unity. Because in some cases the filter functions are not precisely zero at the tails, we elect to use the trapezium rule to evaluate (3):

$$R = \frac{\Delta\nu}{2}\left[B(\nu_1,T)\,\phi(\nu_1) + B(\nu_{60},T)\,\phi(\nu_{60})\right] + \Delta\nu\sum_{i=2}^{59} B(\nu_i,T)\,\phi(\nu_i) \tag{5}$$

We use equation (5) to create a three-column temperature-to-radiance lookup table, one column for each channel, computed for a temperature range of 180 K to 340 K in 0.1 K steps. (A coarsely sampled subset from the full NOAA 11 lookup table is shown in Table 1.) Thereafter, all conversions from temperature to radiance (and vice versa) are done by interpolating within the body of the table.

TABLE 1. Sample Subset from the NOAA 11 Temperature-to-Radiance Lookup Table

Temperature, K	Radiance, $\mathrm{mW/(m^2\,sr\,cm^{-1})}$		
	Channel 3	Channel 4	Channel 5
180	0.00013	5.761	8.531
190	0.00040	8.504	12.155
200	0.00108	12.076	16.718
210	0.00266	16.588	22.314
220	0.00606	22.144	29.019
230	0.01288	28.832	36.896
240	0.02569	36.733	45.996
250	0.04850	45.912	56.354
260	0.08725	56.422	67.997
270	0.15032	68.305	80.937
280	0.24917	81.589	95.179
290	0.39896	96.296	110.718
300	0.61918	112.435	127.545
310	0.93425	130.008	145.643
320	1.37407	149.010	164.989
330	1.97449	169.429	185.559
340	2.77774	191.249	207.325

This subset table was created by integrating the Planck function at the specified temperature across each of the channel filter functions in turn. (The full lookup table has a resolution of 0.1 K.)

To summarize: The satellite broadcasts the space count SC, the internal target count IC, and the PRT temperature count t as part of each scan line. The ground station converts the PRT count to absolute temperature T of the internal target via equation (1). This is mapped to radiance R by interpolating in the temperature-to-radiance lookup tables generated earlier from equation (5). The linear calibration slope $g = R/(\mathrm{IC} - \mathrm{SC})$ is established for each of the three infrared channels. Thereafter, equation (2) is used to convert the raw radiometric

count x for each scene pixel into the corresponding linear estimate for radiance r_{lin}.

3. RADIANCE CORRECTIONS FOR CHANNELS 4 AND 5

Equation (2) is valid for all counts x only if the detector response varies linearly with radiance. However, the channel 4 and 5 sensors have a slight curvature, which we model as quadratic, in their radiance-versus-counts response as indicated in Figures 2 and 3 (the curvature has been exaggerated in the latter figure for clarity). For these channels the linear conversion of (2) can only be correct when the scene radiance matches either of the two reference radiances (i.e., either zero radiance or ICT radiance). For scene radiances higher than that of the ICT, the linear approximation will underestimate the true scene radiance, while for lower scene radiances it will overestimate. Therefore for channels 4 and 5 a correction must be applied to the linear fit. This adjustment is referred to as the "nonlinearity correction."

The in-flight ICT temperature is not constant; it varies rapidly as the spacecraft moves into (or out of) Earth shadow, and more gradually at other times. The anticipated minimum and maximum operating temperatures are approximately 10° and 20°C respectively, although for a given ground station overpass the temperature variation is unlikely to exceed 2°–3°C. If the ICT temperature increases, the upper calibration point defined by the intersection between the true calibration curve and the linear fit moves further up the curve (see Figure 3*b*), and the nonlinearity corrections alter correspondingly. Similarly, a decreasing spacecraft temperature drives the calibration point down the curve, and again the NLCs must be altered. It was *Brown et al.* [1985] who first recognized that the NLCs are necessarily a function of ICT temperature.

NESDIS publishes tables of nonlinearity corrections computed from prelaunch tests in which the radiometer views a calibrated laboratory blackbody whose temperature ranges from 175 to 315 K in steps of 5 or 10 K. The calibration procedure is carried out for three settings (four for NOAA-12) of the AVHRR's baseplate temperature, nominally 10°, 15°, and 20°C (and 25°C for NOAA 12). This determines the "true" AVHRR radiance-to-counts calibration (the curved line in Figure 3). The linear approximation draws a straight line which intersects the curve at zero radiance, and again at the baseplate radiance. The deviations away from the linear fit define the required corrections: $\Delta r = r_{true} - r_{lin}$. Thus the true scene radiance is obtained by adding the correction to the linear result.

For historical reasons, NESDIS transforms these radiance corrections into brightness temperature corrections, and tabulates them as a function of apparent scene temperature (rather than apparent scene radiance); this is the form in which the NLC tables are published. (For an example, refer to the first four columns of Table 2.) The presentation of the corrections in this form makes life awkward for users who wish to extract corrected radiance rather than brightness temperature, requiring a four-step process: (1) count to radiance via equation (2); (2) radiance to temperature via table lookup; (3) temperature to corrected temperature via NLC tables; (4) corrected temperature back to corrected radiance via reverse lookup. The more direct approach would be to recover the original tables of radiance corrections to be applied to the scene radiance calculated from equation (2); at that point the user could convert the corrected radiance to brightness temperature should he or she so wish. Since we feel that such tables are useful, we computed the full set of radiance corrections for NOAA 9, 10, 11, and 12. These are contained in Tables 2 to 9, and plotted in Figures 4 to 11.

To regenerate the original radiance NLCs, we "reverse engineered" the NESDIS tables by making two interpolative forays per correction into the temperature-to-radiance lookup tables (LUTs), first to convert the apparent scene temperature T_{lin} to apparent scene radiance r_{lin}, the second time to find the true radiance corresponding to the corrected temperature $(T_{lin} + \Delta T)$ where ΔT is the NLC in temperature space); the difference gives the radiance correction:

$$\Delta r = r_{true} - r_{lin} = \mathrm{LUT}(T_{lin} + \Delta T) - \mathrm{LUT}(T_{lin}) \tag{6}$$

where $\mathrm{LUT}(T)$ means "the radiance corresponding to brightness temperature T obtained from interpolation within the radiance lookup table."

Figures 8 and 9 show the results of plotting the temperature corrections versus apparent scene temperature, and the corresponding radiance corrections versus apparent scene radiance for channels 4 and 5 of NOAA 11. Viewed in temperature space, the corrections appear as sets of nearly parallel curves. As *Weinreb et al.* [1990] observe, if the curves were exactly parallel, then considered as a function of scene temperature minus base plate temperature, the correction terms would be independent of base plate temperature.

However, when viewed in radiance space, the corrections form a nest of well-defined parabolas. This is consistent with our initial assumption that the underlying count-to-radiance calibration curve is well approximated by a quadratic function (e.g., Figure 2). We would not expect the curvature of this underlying calibration curve to depend on the base plate temperature (even though the correction magnitudes clearly do), in view of the instrument description by *Schwalb* [1978, pp. 43–45] indicating that the infrared detectors are mounted adjacent to a radiant cooler which maintains their temperature at a constant 105 K. (In fact, maintaining HgCdTe detectors at low temperature would appear to be a necessary condition for their successful operation [*Norwood and Lansing*, 1983, p. 354].)

All three radiance correction curves in Figure 8*b* pass through the origin (zero error at zero radiance), and have as their second root the radiance R of the internal target at the specified base plate temperature (zero error when the scene radiance matches the ICT radiance: this is the upper calibration point in Figure 3). Since the horizontal axis of Figure 8*b* is the apparent scene radiance r_{lin}, (i.e., the radiance as estimated from the linear equation (2)), each correction parabola can be expressed as a quadratic function of r_{lin}:

$$\Delta r = k r_{lin}(r_{lin} - R) \tag{7}$$

where

$$r_{lin} = g(x - \mathrm{SC}) \tag{8}$$

and k, the quadratic coefficient for the corrections parabola, is a least squares fitted constant (details given later this section). The corrected scene radiance then is obtained by adding (7) to (8):

$$r = r_{lin} + \Delta r \tag{9}$$

Once the corrections coefficient k has been established, equations (7) through (9) provide a simple algorithm for correcting linear radiance estimates in channels 4 and 5. It is considerably more straightforward to implement than the four-step $r_{lin} \rightarrow T_{lin} \rightarrow T_{true} \rightarrow r_{true}$ process outlined above, and it allows direct calculation of the radiance NLC at any baseplate temperature without the need to interpolate in the NESDIS ta-

TABLE 2. Temperature Corrections [Weinreb et al., 1990, Table 3] and the Corresponding Radiance Corrections for NOAA 9, Channel 4

Scene Temperature	Temperature Correction			Scene Radiance	Radiance Correction		
	10.0	15.0	19.3		10.0	15.0	19.3
320	2.35	2.53	2.28	148.676	4.67	5.03	4.53
315	1.89	1.97	1.81	139.003	3.61	3.77	3.46
310		1.55	1.31	129.686		2.85	2.41
305	1.45	1.02	0.88	120.728	2.56	1.80	1.55
295	0.82	0.46	0.17	103.888	1.33	0.74	0.27
285	0.11	-0.22	-0.48	88.485	0.16	-0.32	-0.70
275	-0.48	-0.61	-0.90	74.513	-0.63	-0.81	-1.19
265	-0.71	-0.84	-1.26	61.955	-0.84	-0.99	-1.48
255	-0.96	-1.25	-1.50	50.787	-1.00	-1.30	-1.56
245	-1.09	-1.36	-1.66	40.973	-0.99	-1.23	-1.50
235	-1.15	-1.38	-1.60	32.466	-0.90	-1.07	-1.24
225	-1.32	-1.39	-1.53	25.204	-0.87	-0.91	-1.01
215	-1.22	-1.34	-1.42	19.116	-0.67	-0.73	-0.77
205	-1.21	-1.48	-0.90	14.116	-0.54	-0.65	-0.40

The first column gives a vector of apparent scene temperatures, in K, computed via the linear model of equation (2). The next three columns define the temperature corrections to be applied (added) to the apparent scene temperature for baseplate temperatures of 10.0°, 15.0°, and 19.3°C. The final three columns contain the corresponding radiance corrections to be added to a given apparent scene radiance. In application, interpolate vertically within the scene temperature (or radiance) column, then horizontally between bracketing baseplate temperature columns to arrive at the appropriate temperature (or radiance) correction.

TABLE 3. Temperature Corrections [*Weinreb et al.*, 1990, Table 3] and the Corresponding Radiance Corrections for NOAA 9, Channel 5

Scene Temperature	Temperature Correction			Scene Radiance	Radiance Correction		
	10.0	15.0	19.3		10.0	15.0	19.3
320	0.82	1.14	1.16	164.495	1.64	2.28	2.32
315	0.64	0.83	0.91	154.666	1.24	1.61	1.77
310		0.71	0.68	145.148		1.33	1.28
305	0.66	0.35	0.47	135.944	1.20	0.63	0.85
295	0.45	0.20	0.09	118.489	0.76	0.34	0.15
285	0.05	-0.09	-0.24	102.320	0.08	-0.14	-0.37
275	-0.25	-0.31	-0.47	87.450	-0.36	-0.44	-0.67
265	-0.42	-0.46	-0.75	73.886	-0.54	-0.59	-0.96
255	-0.63	-0.81	-0.91	61.627	-0.73	-0.94	-1.05
245	-0.76	-0.92	-1.12	50.664	-0.78	-0.94	-1.15
235	-1.03	-1.19	-1.31	40.976	-0.93	-1.07	-1.18
225	-1.14	-1.11	-1.14	32.531	-0.89	-0.86	-0.89
215	-1.24	-1.28	-1.41	25.286	-0.82	-0.84	-0.93
205	-1.43	-1.62	-1.23	19.183	-0.78	-0.89	-0.68

TABLE 4. Temperature Corrections [*Weinreb et al.*, 1990, Table 4] and the Corresponding Radiance Corrections for NOAA 10, Channel 4

Scene Temperature	Temperature Correction			Scene Radiance	Radiance Correction		
	8.7	13.8	19.1		8.7	13.8	19.1
320	3.50	2.83	2.54	152.595	7.02	5.66	5.08
315	2.93	2.19	1.97	142.858	5.66	4.22	3.80
305	1.88	1.34	1.11	124.427	3.36	2.39	1.98
295	1.12	0.57	0.12	107.396	1.84	0.93	0.20
285	0.20	-0.15	-0.38	91.770	0.30	-0.22	-0.57
275	-0.46	-0.53	-1.08	77.550	-0.62	-0.71	-1.45
265	-0.76	-0.93	-1.37	64.724	-0.92	-1.12	-1.65
255	-1.33	-1.49	-1.77	53.275	-1.42	-1.59	-1.89
245	-1.74	-2.09	-2.26	43.171	-1.62	-1.95	-2.10
235	-1.79	-2.20	-2.53	34.372	-1.44	-1.77	-2.03
225	-2.22	-2.51	-2.53	26.825	-1.51	-1.71	-1.72
215	-2.58	-2.65	-2.80	20.463	-1.46	-1.50	-1.58
205	-2.47	-2.88	-3.27	15.207	-1.14	-1.32	-1.49

TABLE 5. Temperature Corrections [*Weinreb et al.*, 1990, Table 5] and the Corresponding Radiance Corrections for NOAA 11, Channel 4, Based on the Original 1981 Data

Scene Temperature	Temperature Correction			Scene Radiance	Radiance Correction		
	9.2	13.9	19.0		9.2	13.9	19.0
320	4.81	4.16	3.64	149.010	9.65	8.32	7.27
315	4.03	3.43	2.93	139.331	7.77	6.60	5.63
310	3.28	2.68	2.20	130.008	6.08	4.95	4.06
305	2.56	1.99	1.52	121.042	4.55	3.53	2.69
295	1.27	0.82	0.27	104.186	2.06	1.33	0.44
285	0.23	-0.20	-0.71	88.764	0.34	-0.29	-1.04
275	-0.61	-1.06	-1.41	74.770	-0.81	-1.40	-1.86
265	-1.22	-1.58	-1.91	62.190	-1.44	-1.86	-2.24
255	-1.70	-2.08	-2.35	50.998	-1.77	-2.16	-2.43
245	-2.02	-2.43	-2.63	41.159	-1.83	-2.19	-2.37
235	-2.21	-2.42	-2.55	32.627	-1.72	-1.87	-1.97
225	-2.18	-2.46	-2.71	25.341	-1.43	-1.61	-1.77
215	-2.17	-2.41	-2.55	19.230	-1.18	-1.31	-1.38
205	-1.97	-2.25	-2.12	14.208	-0.87	-0.99	-0.93

TABLE 6. Revised Temperature and Radiance Corrections for NOAA 11 Channel 4, Based on the Recalibration Data from 1988 [*Weinreb et al.*, 1990, Table 7]

Scene Temperature	Temperature Correction			Scene Radiance	Radiance Correction		
	9.2	14.2	19.0		9.2	14.2	19.0
320	4.29	3.71	3.25	149.010	8.59	7.41	6.48
315	3.50	2.98	2.55	139.331	6.74	5.73	4.89
310	2.85	2.33	1.91	130.008	5.27	4.30	3.52
305	2.23	1.73	1.32	121.042	3.95	3.06	2.33
295	1.05	0.68	0.22	104.186	1.70	1.10	0.36
285	0.24	-0.21	-0.67	88.764	0.35	-0.31	-0.98
275	-0.45	-0.79	-1.15	74.770	-0.60	-1.05	-1.52
265	-1.06	-1.37	-1.66	62.190	-1.25	-1.61	-1.95
255	-1.41	-1.72	-2.03	50.998	-1.47	-1.79	-2.11
245	-1.70	-1.96	-2.22	41.159	-1.54	-1.77	-2.01
235	-1.87	-2.10	-2.28	32.627	-1.46	-1.63	-1.77
225	-1.90	-2.14	-2.36	25.341	-1.25	-1.40	-1.55
215	-1.82	-2.02	-2.20	19.230	-0.99	-1.10	-1.20
205	-1.54	-1.76	-1.98	14.208	-0.68	-0.78	-0.87

The NOAA 11 AVHRR was originally calibrated in 1981, then retested prior to launch in 1988. As a result, a revised set of nonlinearity corrections was issued for channel 4. (In contrast, the channel-5 retests showed no significant change.)

TABLE 7. Temperature and Radiance Corrections for NOAA 11 Channel 5, Based on 1981 Data [*Weinreb et al.*, 1990, Table 5]

Scene Temperature	Temperature Correction			Scene Radiance	Radiance Correction		
	9.2	13.9	19.0		9.2	13.9	19.0
320	1.43	1.26	1.12	164.989	2.87	2.53	2.24
315	1.23	1.03	0.89	155.161	2.39	2.00	1.73
310	1.05	0.84	0.70	145.643	1.97	1.58	1.31
305	0.85	0.64	0.47	136.436	1.54	1.16	0.85
295	0.43	0.28	0.09	118.972	0.72	0.47	0.15
285	0.07	-0.07	-0.23	102.787	0.11	-0.11	-0.36
275	-0.19	-0.34	-0.47	87.895	-0.27	-0.48	-0.67
265	-0.37	-0.51	-0.60	74.304	-0.48	-0.66	-0.77
255	-0.60	-0.77	-0.78	62.014	-0.70	-0.89	-0.90
245	-0.72	-0.90	-0.92	51.016	-0.74	-0.93	-0.95
235	-0.84	-1.02	-1.00	41.290	-0.76	-0.92	-0.90
225	-0.94	-1.06	-1.16	32.807	-0.73	-0.83	-0.91
215	-1.12	-1.24	-1.16	25.523	-0.74	-0.82	-0.77
205	-1.15	-1.27	-1.23	19.382	-0.64	-0.70	-0.68

TABLE 8. Temperature Corrections and Corresponding Radiance Corrections for NOAA 12, Channel 4 (May 1991 Addendum to *Planet* [1988])

Scene Temperature	Temperature Correction 8.9	14.7	19.5	23.9	Scene Radiance	Radiance Correction 8.9	14.7	19.5	23.9
320	3.21	2.88	2.27	1.91	150.306	6.41	5.75	4.52	3.80
315	2.58	2.39	1.72	1.43	140.608	4.96	4.59	3.30	2.74
310	2.04	1.94	1.28	0.98	131.262	3.77	3.58	2.36	1.80
305	1.60	1.42	0.80	0.52	122.270	2.84	2.52	1.41	0.92
295	0.80	0.53	0.13	-0.16	105.352	1.30	0.86	0.21	-0.26
285	0.16	-0.23	-0.52	-0.70	89.859	0.24	-0.34	-0.77	-1.03
275	-0.41	-0.84	-1.05	-1.19	75.784	-0.55	-1.12	-1.40	-1.58
265	-0.71	-0.97	-1.19	-1.32	63.116	-0.85	-1.15	-1.41	-1.57
255	-1.04	-1.20	-1.53	-1.59	51.831	-1.10	-1.26	-1.61	-1.67
245	-1.18	-1.40	-1.58	-1.62	41.897	-1.09	-1.29	-1.45	-1.49
235	-1.05	-1.59	-1.51	-1.63	33.268	-0.83	-1.26	-1.19	-1.29
225	-1.33	-1.65	-1.58	-1.67	25.887	-0.89	-1.10	-1.06	-1.12
215	-1.24	-1.65	-1.49	-1.53	19.685	-0.69	-0.92	-0.83	-0.85
205	-1.58	-1.80	-1.31	-1.33	14.577	-0.71	-0.81	-0.59	-0.60

Note that there are now four columns of temperature corrections.

TABLE 9. Temperature Corrections and Corresponding Radiance Corrections for NOAA 12, Channel 5 (May 1991 Addendum to *Planet* [1988])

Scene Temperature	Temperature Correction 8.9	14.7	19.5	23.9	Scene Radiance	Radiance Correction 8.9	14.7	19.5	23.9
320	0.80	0.80	0.80	0.73	165.810	1.60	1.60	1.60	1.46
315	0.80	0.80	0.73	0.61	155.983	1.55	1.55	1.42	1.18
310	0.80	0.73	0.61	0.37	146.462	1.50	1.37	1.15	0.69
305	0.73	0.61	0.37	0.18	137.251	1.33	1.11	0.67	0.33
295	0.37	0.18	0.08	-0.08	119.769	0.62	0.30	0.13	-0.13
285	0.08	-0.08	-0.21	-0.31	103.555	0.12	-0.12	-0.33	-0.48
275	-0.21	-0.31	-0.37	-0.41	88.626	-0.30	-0.44	-0.53	-0.58
265	-0.37	-0.41	-0.47	-0.53	74.990	-0.48	-0.53	-0.61	-0.69
255	-0.47	-0.53	-0.63	-0.76	62.648	-0.55	-0.62	-0.73	-0.89
245	-0.63	-0.76	-0.88	-0.94	51.592	-0.65	-0.79	-0.91	-0.97
235	-0.88	-0.94	-1.01	-1.10	41.805	-0.80	-0.86	-0.92	-1.00
225	-1.01	-1.10	-1.15	-1.19	33.258	-0.80	-0.87	-0.91	-0.94
215	-1.15	-1.19	-1.17	-1.16	25.910	-0.77	-0.80	-0.78	-0.78
205	-1.17	-1.16	-1.19	-1.23	19.705	-0.65	-0.65	-0.67	-0.69

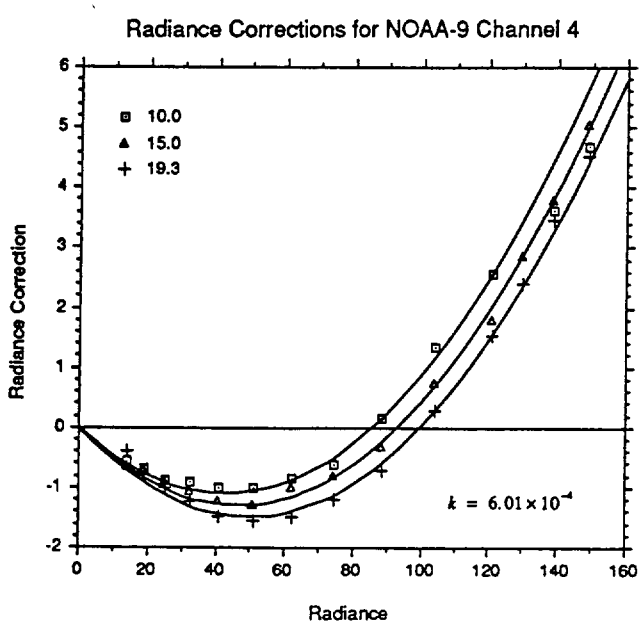

Fig. 4. Radiance corrections for channel 4 of NOAA 9. Least squares parabolas of the form $\Delta r = k r_{lin}(r_{lin} - R)$ have been fitted to the radiance data from Table 2.

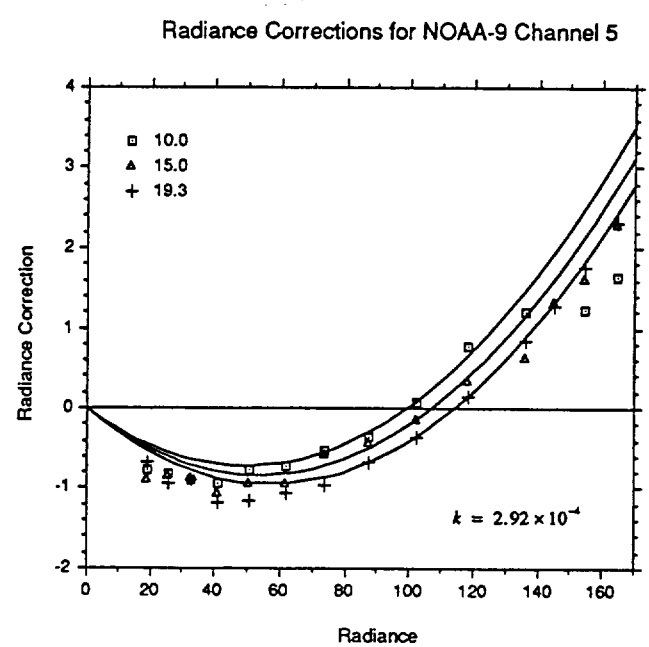

Fig. 5. Radiance correction parabolas for channel 5 of NOAA 9, plotted from Table 3.

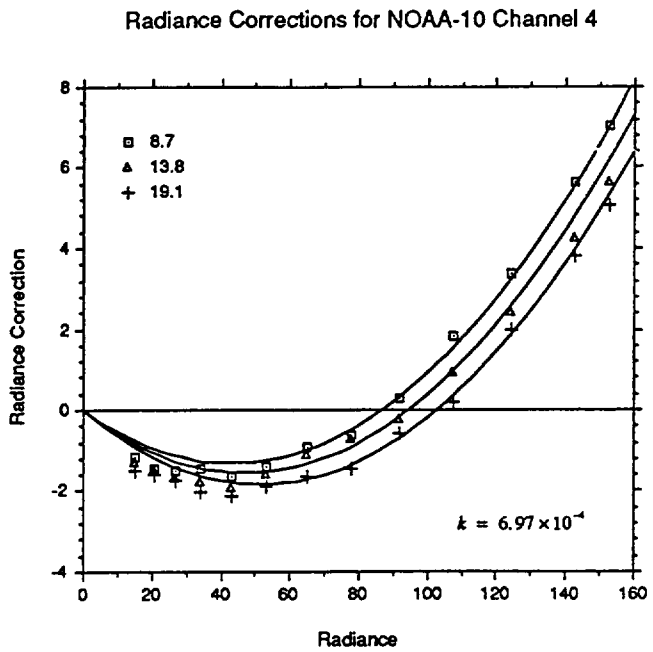

Fig. 6. Radiance correction parabolas for channel 4 of NOAA 10, plotted from Table 4.

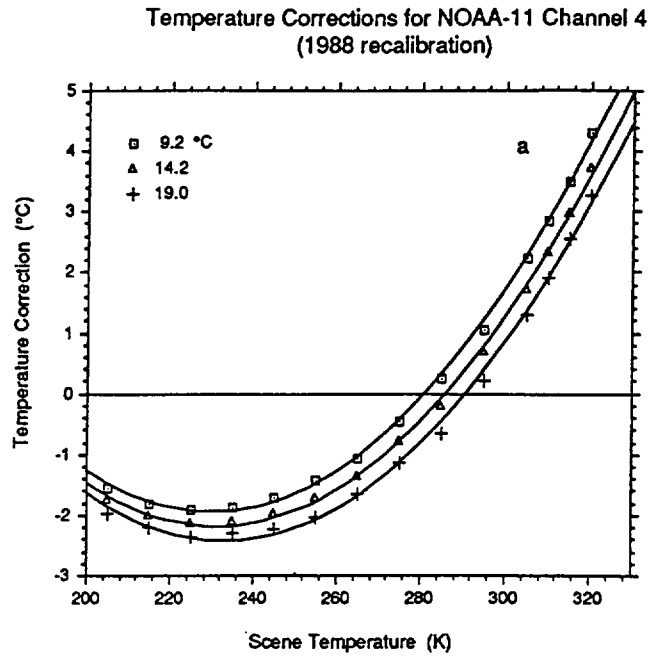

Fig. 8a. Temperature corrections for channel 4 of NOAA 11, based on 1988 revised calibration set in Table 6.

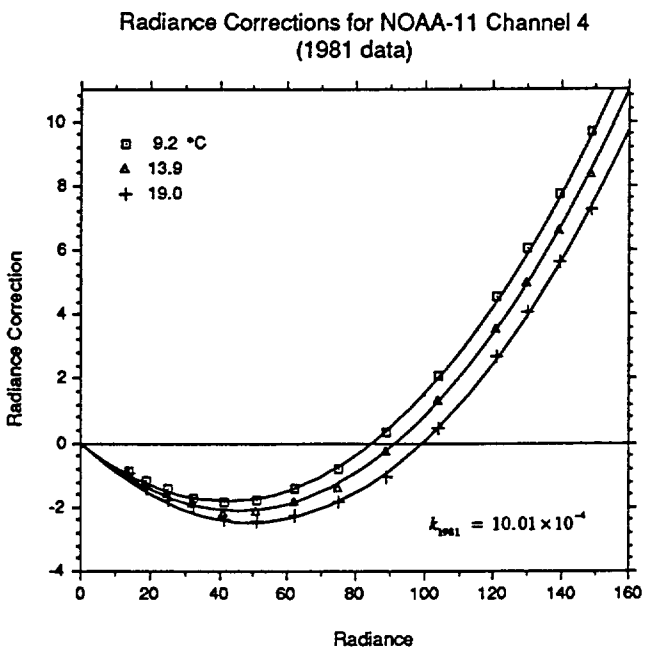

Fig. 7. Radiance correction parabolas for channel 4 of NOAA 11, based on the 1981 calibration data contained in Table 5.

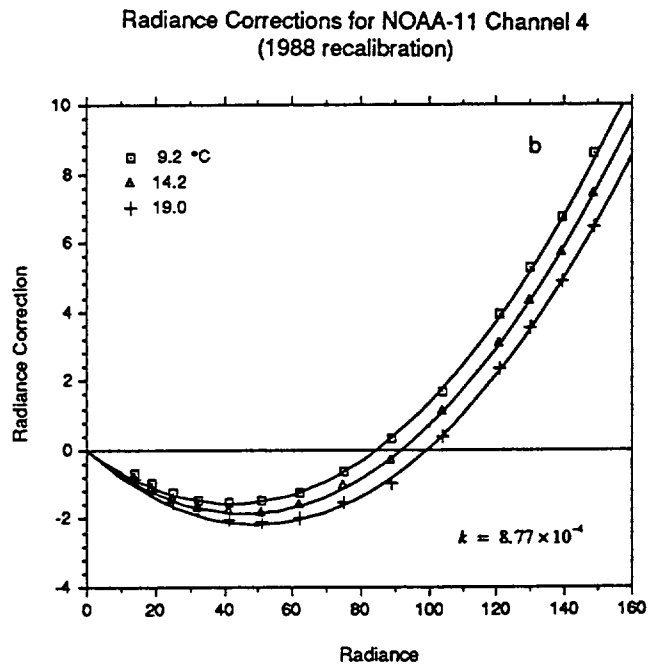

Fig. 8b. Radiance corrections for channel 4 of NOAA 11, based on 1988 revised calibrations. Least squares parabolas of the form $\Delta r = k r_{\text{lin}} (r_{\text{lin}} - R)$ have been fitted to the radiance data from Table 6. For each radiance curve the two zero-correction points (i.e., the roots of the corrections quadratic) occur when the radiance is zero, and when the target radiance matches R, the radiance of the ICT.

bles. For users who require brightness temperature, the three steps would be $r_{\text{lin}} \rightarrow r_{\text{true}} \rightarrow T_{\text{true}}$; the important change from present procedure is that the correction is to be applied before conversion to temperature, rather than after.

In fact, we can reduce (7) to an even simpler form if we know the quadratic factor in the original calibration equation (i.e., the curve generated from the prelaunch ITT experiments, e.g., Figure 2) which relates the AVHRR count x to radiance:

$$r(x) = ax^2 + bx + c = a(x - \text{SC})(x - \gamma) \tag{10}$$

with a, b, and c being calibration constants. We refer (rather loosely) to a as the curvature of the count-to-radiance function. It is useful to write the expression in the factorized form, showing explicitly that the radiance goes to zero at $x = \text{SC}$ (the space view), and at some other point, $x = \gamma$ (of no physical significance). The curvature a is assumed to be fixed for all time, but the other "constants" b and c, or equivalently, SC and γ, may vary in flight. (In practice, the space count is

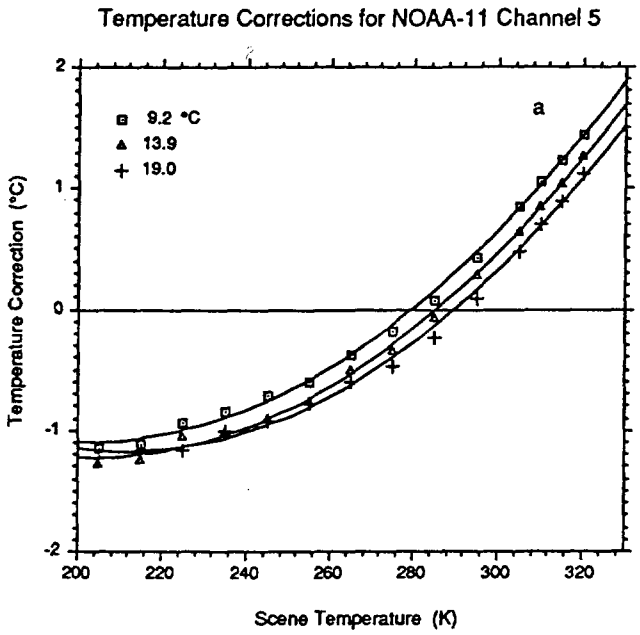

Fig. 9*a*. Temperature corrections for channel 5 of NOAA 11, fitted to the 1981 data of Table 7.

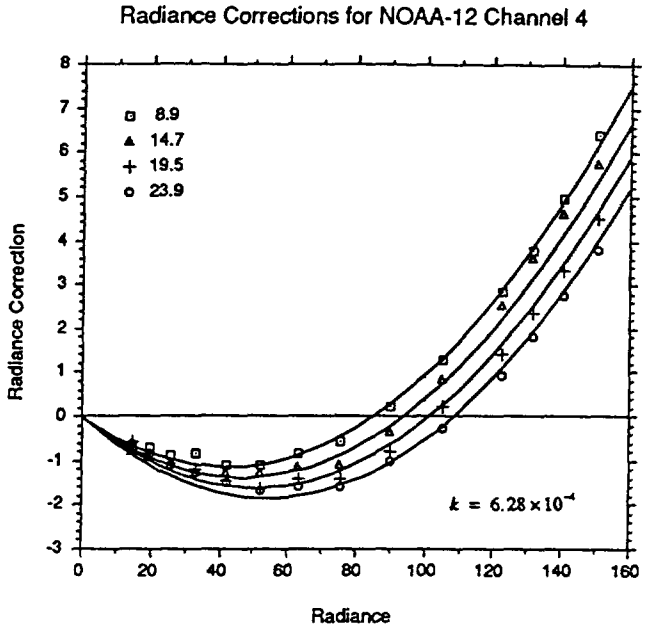

Fig. 10. Radiance correction parabolas for channel 4 of NOAA 12, fitted to the radiance data of Table 8.

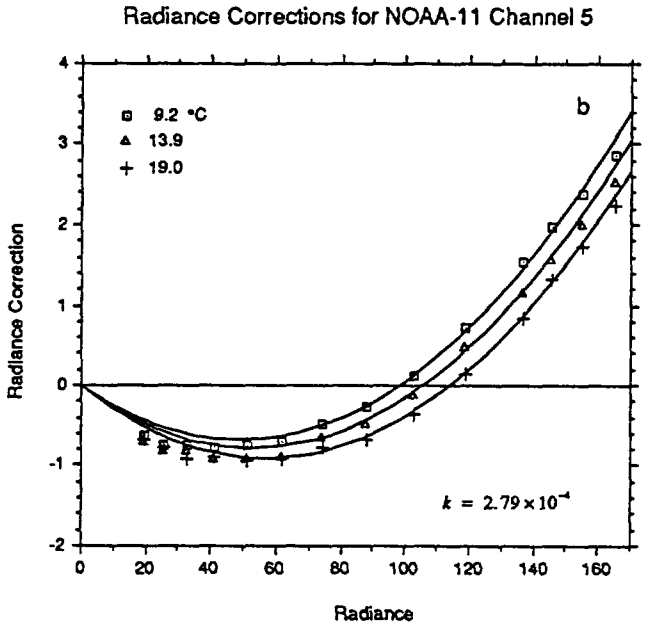

Fig. 9*b*. Radiance correction parabolas for channel 5 of NOAA 11, fitted to the 1981 radiance data of Table 7.

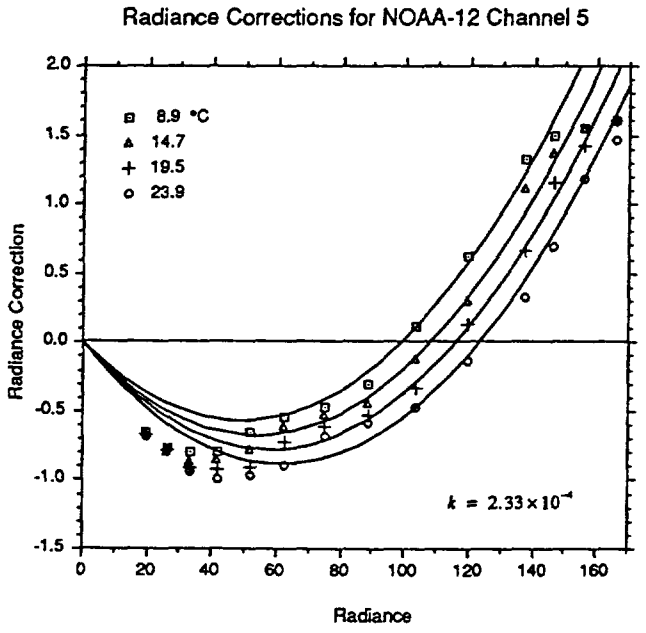

Fig. 11. Radiance correction parabolas for channel 5 of NOAA 12, fitted to the radiance data of Table 9. Unlike most of the other radiance correction curves, the experimental data seem not to follow the expected trend at both the high- and low-radiance extremes. This may point up systematic measurement errors in the prelaunch calibration experiments. Nevertheless, the agreement over the important sea surface radiance range is quite satisfactory.

very stable: we found that the value of SC for channels 4 and 5, after averaging in blocks of 50 scan lines, did not vary by more than ±0.04 and ±0.2 count, respectively, for the 48 NOAA 11 passes extracted over a full year.)

It follows from (10) that when $x = \mathrm{IC}$ (the ICT view), the radiance will be R:

$$R = r(\mathrm{IC}) = a(\mathrm{IC} - \mathrm{SC})(\mathrm{IC} - \gamma) \tag{11}$$

so that the linear calibration slope g becomes

$$g = R/(\mathrm{IC} - \mathrm{SC}) = a(\mathrm{IC} - \gamma) \tag{12}$$

Substituting this result into (8), and solving (9) for Δr, we obtain the following alternative to (7):

$$\Delta r = a(x - \mathrm{IC})(x - \mathrm{SC}) \tag{13}$$

The advantage of this form is that, provided we know a, (13) permits calculation of the NLC directly from the raw count. Equating (7) and (13), and eliminating r_{lin} using (8),

we can relate the corrections coefficient k to the calibrations curvature a:

$$k = a/g^2 \tag{14}$$

Because the calibration slope g depends (weakly) on base plate temperature, the corrections coefficient k will also vary with base plate temperature (higher ICT temperatures will be associated with lower values for k). This means that, strictly speaking, each of the three correction parabolas (corresponding to the three base plate temperatures) for a given channel should have its own k value. In practice, we find that this subtle variation in k is dominated by "noise" in the NESDIS NLC tables. *Weinreb et al.* [1990] remark that the lack of smoothness in some of the temperature-correction curves (e.g., Figure 9*a*) probably originates in the test procedures themselves.

Since the preflight values for a are unknown (to us), we have elected to work with equation (7) rather than (13), and to estimate a single average value for k which applies to all three (or four, in the case of NOAA 12) radiance correction parabolas for a given channel. The advantage of this average-value approach is that (7) can then be applied for any baseplate temperature, not just the nominal 10°, 15°, or 20°C temperatures which head the NLC tables.

Having extracted k, we could in principle calculate the curvature a from equation (14), but only if we knew the preflight values for the linear calibration slope g. Since we do not, the best we can do is to use averaged values for the calibration slopes derived from the inflight measurements. Because k is an average best fit value across the range of baseplate temperatures, we computed a representative slope which was averaged across the range of base plate temperatures accessible to us. For NOAA 9, we analyzed a single pass from mid 1988, and for NOAA 11 we used the full-year suite of 48 passes described below in section 4. (We have not yet examined in-flight data for NOAA 10 or 12.)

To explain our k extraction and a estimation methodologies, consider the radiance corrections for channel 5 of NOAA 11 (Table 7, Figure 9*b*). For each of the actual baseplate brightness temperatures {9.2, 13.9, 19.0}°C, we computed the corresponding channel 5 radiances R = {98.7, 106.0, 114.2} mW/(m^2 sr cm^{-1}), then evaluated least squares fits to the form $\Delta r = k r_{lin}(r_{lin} - R)$ to determine the corrections quadratic coefficient k for each curve in turn. The results for the three curves were $k = \{2.794, 2.778, 2.810\} \times 10^{-4}$. Because these values do not form a smoothly diminishing sequence with ICT temperature, we conclude that the true coefficients have been masked by measurement noise, so compute the average of the three using their sample standard deviation as the uncertainty estimate: $k_{ave} = (2.79 \pm 0.02) \times 10^{-4}$. From the 48-pass suite of NOAA 11 observations, for which the base plate temperature varied from 11.7° to 16.1°C, the average channel 5 calibration slope g was $-(0.1797 \pm 0.0004)$ radiance units per count; this implies a channel 5 estimated curvature $a = k_{ave} g^2 = (0.902 \pm 0.006) \times 10^{-5}$. Encouragingly, when we performed the analogous set of computations for NOAA 9 channel 4, we obtained a curvature estimate of $a = (1.59 \pm 0.04) \times 10^{-5}$ which agrees rather well with the 1.568×10^{-5} value gleaned from our least squares fit to the ITT calibration curve shown in Figure 2.

We repeated the k extraction procedures for all of the radiance correction tables. In some cases we omitted from the curve fit those extreme values which appeared to be glaring outliers; for example, we ignored the last two entries within the 8.9° and 14.7°C columns of Table 9 (NOAA 12 channel 5). The results of this work are contained in Table 10. There are three general observations. The corrections coefficient for channel 4 across the various AVHRRs is consistently higher than that for the corresponding channel 5 sensor by a factor of about 2 or 3, and therefore so are the relative magnitudes of the corrections to be applied; the NLC radiance curves for channel 4 are generally "better behaved" (less noisy) than those for channel 5; channel 5 generally exhibits deviations away from the expected trend at both the high and low radiance extremes. We do not know whether these deviations are real or a consequence of the calibration procedures. The first two observations are confirmed by the in-flight calibration record for NOAA 11 (discussed in detail in the next section): channel 5 has lower curvature but higher noise.

TABLE 10. Quadratic Coefficient k for Radiance Correction Parabolas, and Estimated Curvature a for the Underlying Count-to-Radiance Quadratic

Satellite	AVHRR Channel		k / 10^{-4}	a / 10^{-5}
NOAA 9	4		6.01 ± 0.14	1.59 ± 0.04
NOAA 9	5		2.92 ± 0.30	0.94 ± 0.10
NOAA 10	4		6.97 ± 0.33	
NOAA 11	4	(1981)	(10.01 ± 0.16)	(2.94 ± 0.05)
NOAA 11	4	(1988)	8.77 ± 0.12	2.58 ± 0.04
NOAA 11	5		2.79 ± 0.02	0.90 ± 0.01
NOAA 12	4		6.28 ± 0.47	
NOAA 12	5		2.33 ± 0.10	

Each entry has been scaled as indicated at the head of the column. The radiance correction Δr for a given channel can either be calculated from equation (7) using k and r_{lin}, or from equation (13) using a and raw radiometric count x.

Of particular interest is the degree to which the fitted corrections parabolas match the NESDIS corrections (expressed in radiance space) over the sea surface temperature range 273 to 310 K (neglecting atmospheric attenuation, this corresponds to radiance ranges 70–130 for channel 4, and 85–145 mW/(m^2 sr cm^{-1}) for channel 5). From inspection of the corrections graphs, it is clear that this temperature interval brackets the family of zero-error crossings, and for this interval at least, the agreement is generally very satisfactory. For radiances outside this range, the deviation of the experimental calibrations away from the smooth parabolic trends may simply be due to systematic errors in the measurement procedures. It is difficult to imagine, for instance, that the departures from the quadratic form displayed by the NOAA 12 channel 5 data (Figure 11) are more "real" than the smooth well-behaved trends shown by NOAA 11 channel 4 (Figures 7 and 8). Even if the departures were real, they tend to occur at the low and high radiance extremes and so are of little consequence to sea surface radiance and temperature estimates.

4. IN-FLIGHT DATA: NOAA 11

We examined in detail the in-flight calibration records generated by NOAA 11 for two daytime ascending and two nighttime descending passes received at Hobart on April 30, 1991. By "calibration record" we mean the following set of measurements averaged in blocks of 50 scan lines: {ICT brightness

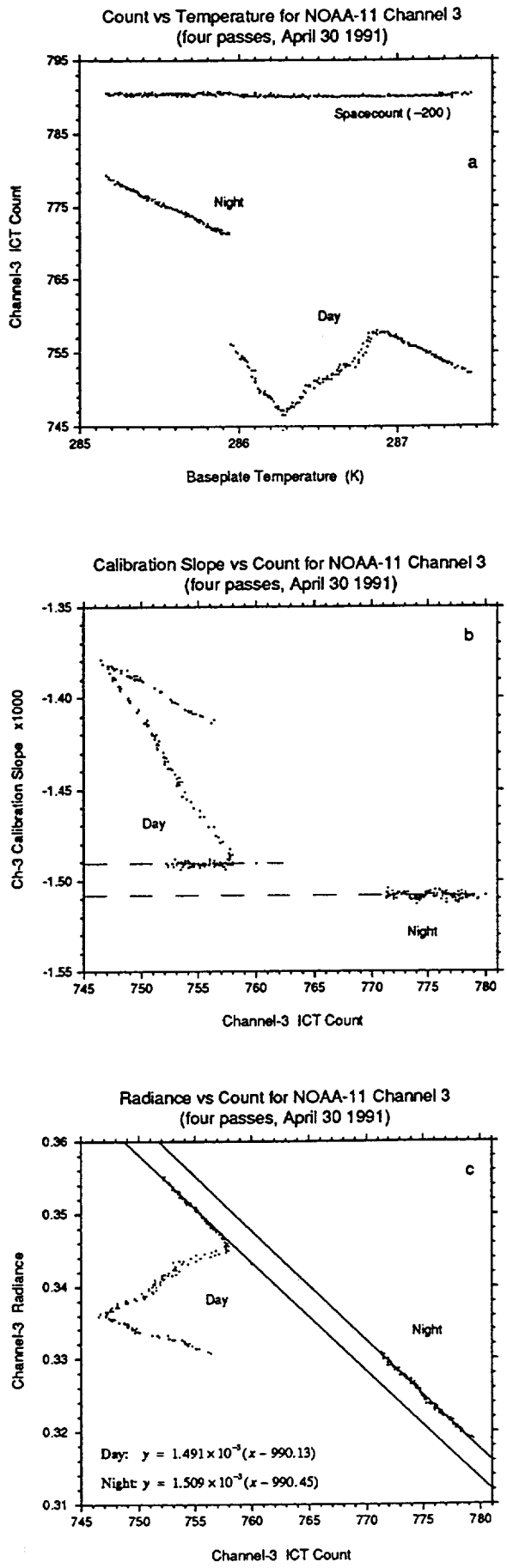
Count vs Temperature for NOAA-11 Channel 3
(four passes, April 30 1991)
Spacecount (~200)
a
Night
Day
Channel-3 ICT Count
Baseplate Temperature (K)
Calibration Slope vs Count for NOAA-11 Channel 3
(four passes, April 30 1991)
b
Day
Night
Ch-3 Calibration Slope x1000
Channel-3 ICT Count
Radiance vs Count for NOAA-11 Channel 3
(four passes, April 30 1991)
c
Day
Night
Day: y = 1.491 x 10^-3 (x - 990.13)
Night: y = 1.509 x 10^-3 (x - 990.45)
Channel-3 Radiance
Channel-3 ICT Count

Fig. 12.

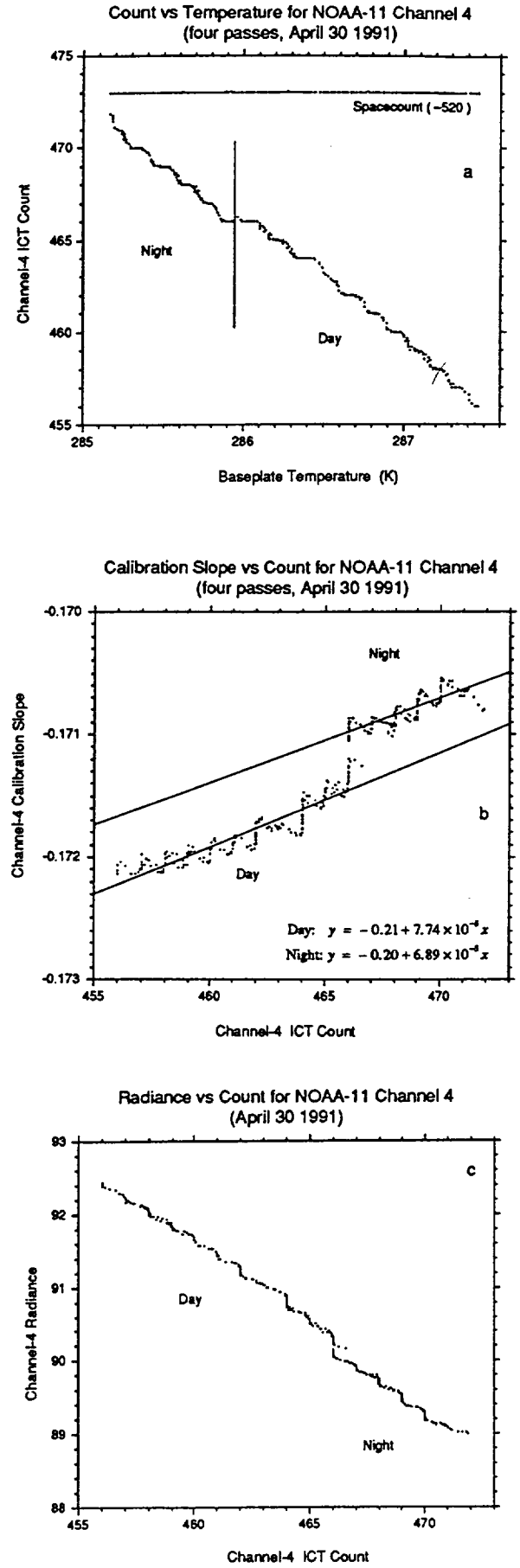
Count vs Temperature for NOAA-11 Channel 4
(four passes, April 30 1991)
Spacecount (~520)
a
Night
Day
Channel-4 ICT Count
Baseplate Temperature (K)
Calibration Slope vs Count for NOAA-11 Channel 4
(four passes, April 30 1991)
Night
b
Day
Day: y = -0.21 + 7.74 x 10^-4 x
Night: y = -0.20 + 6.89 x 10^-4 x
Channel-4 Calibration Slope
Channel-4 ICT Count
Radiance vs Count for NOAA-11 Channel 4
(April 30 1991)
c
Day
Night
Channel-4 Radiance
Channel-4 ICT Count

Fig. 13.

temperature; radiometric counts for both the ICT view and the space view for channels 3, 4, 5}. Since a typical pass consists of about 5000 scan lines, there will be about 100 averaged calibration records per pass. This initial investigation revealed unexpected day-night variations in all three infrared channels, as well as the presence of spurious daytime radiance in channel 3, presumed to be solar in origin. The channel 3 calibration graphs for the four (April 30, 1991) passes are presented in Figure 12.

Figure 12*a* shows the channel 3 ICT count as a function of ICT brightness temperature. As the satellite travels north from its southern polar crossing, it is in full sunlight and warms gradually, so the ICT count should diminish steadily. While this trend is evident in the channel 4 and 5 records (see Figures 13*a* and 14*a*), it is distorted severely in the channel 3 graph: in the early portion of the pass, channel 3 is exposed to an additional source of radiance which depresses the ICT curve by about 20 counts to form a characteristic "shark fin." This behavior is apparent for both daytime passes but is completely missing from the two nighttime (descending) passes during which temperature diminishes with time, causing the ICT count to steadily increase. Note that there is a strong correspondence between time and temperature in this and several of the

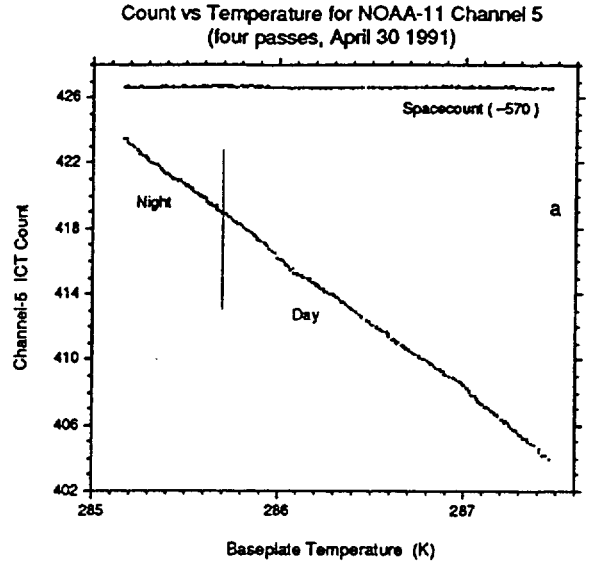

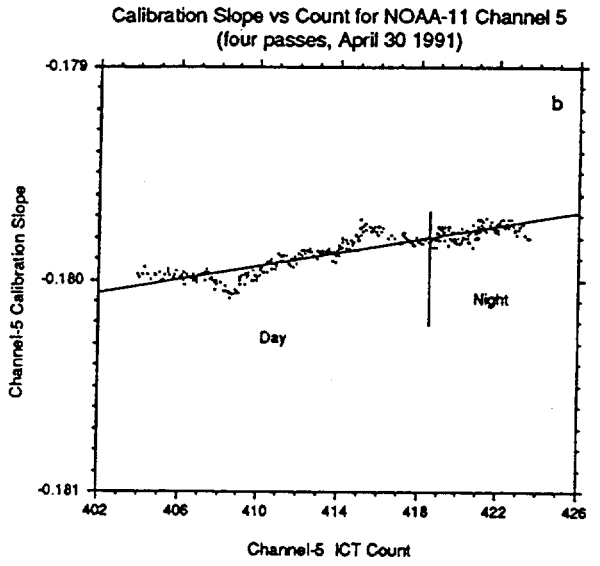

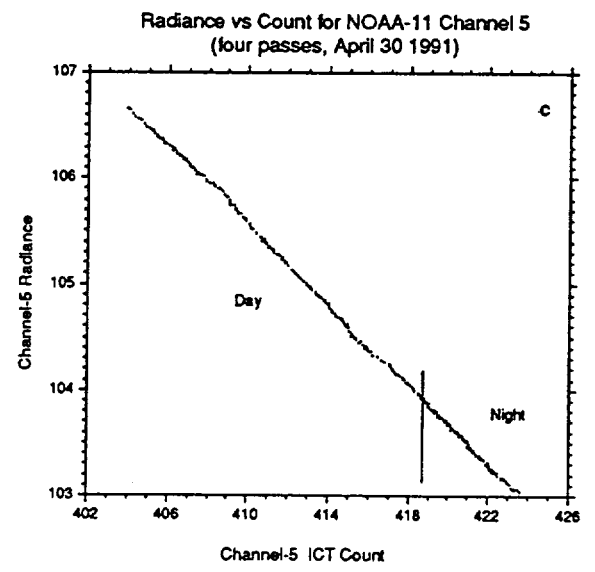

Fig. 14.

Fig. 12. In-flight calibration curves for channel 3 of NOAA 11 for four consecutive passes received at Hobart on April 30, 1991 (two daytime ascending passes plus two nighttime descending passes). (*a*) Channel 3 target count as a function of ICT brightness temperature. ICT temperature typically increases (for an ascending pass over Hobart; it decreases for a descending pass) by about 2°C during the 12-min overflight. Instead of the expected smooth variation of counts with temperature, both day passes exhibit a consistent anomalous behavior persisting for two thirds of the pass. The mismatch between the day and night curves indicates a change in instrument sensitivity. The space count (add 200 to top plot) was substantially constant at 990.28 ± 0.20 counts. (*b*) Plot of channel 3 calibration slope versus ICT count for the April 30 passes, showing distinct day and night clustering about a pair of average values which can be used to derive the linear counts-to-radiance equations. The solar distortion stands out clearly. (*c*) Channel 3 radiance versus ICT count. The brightness temperature data from Figure 12*a* have been converted to channel 3 radiances, and the linear calibration curves superimposed.

Fig. 13. In-flight calibration curves for channel 4 of NOAA 11 for four consecutive passes received at Hobart on April 30, 1991. (*a*) Channel 4 target count as a function of ICT brightness temperature. There is a discontinuity between the day and night curves; individual count steps can be clearly discerned, suggesting a superior noise performance compared with channels 3 and 5. The space count (add 520 to top plot) was substantially constant at 993.014 ± 0.007 counts. (*b*) Plot of channel 4 calibration slope versus ICT count. The distinct day and night graphs both follow an upward trend of approximate slope 7×10^{-5}. If we could be confident that the radiometer is responding only to the ICT temperature changes, then the slope of this graph could provide an in-flight estimate of the channel curvature. (*c*) Channel 4 radiance versus ICT count. The brightness temperature data from Figure 13*a* have been converted to channel 4 radiances. For an ideal radiometer, this graph of radiance versus radiometric count would represent a (tiny, 2°C) subset of the "true" counts-to-radiance calibration curve.

Fig. 14. In-flight calibration curves for channel 5 of NOAA 11 for four consecutive passes received at Hobart on April 30, 1991. (*a*) Channel 5 target count as a function of ICT brightness temperature. The space count (add 570 to top plot) was substantially constant at 996.66 ± 0.04 counts. (*b*) Channel 5 calibration slope versus ICT count. The day and night graphs merge at a count of 418, and follow an upward trend of slope 1.6×10^{-5}. (*c*) Channel 5 radiance versus ICT count. The brightness temperature data from Figure 14*a* have been converted to channel 5 radiances.

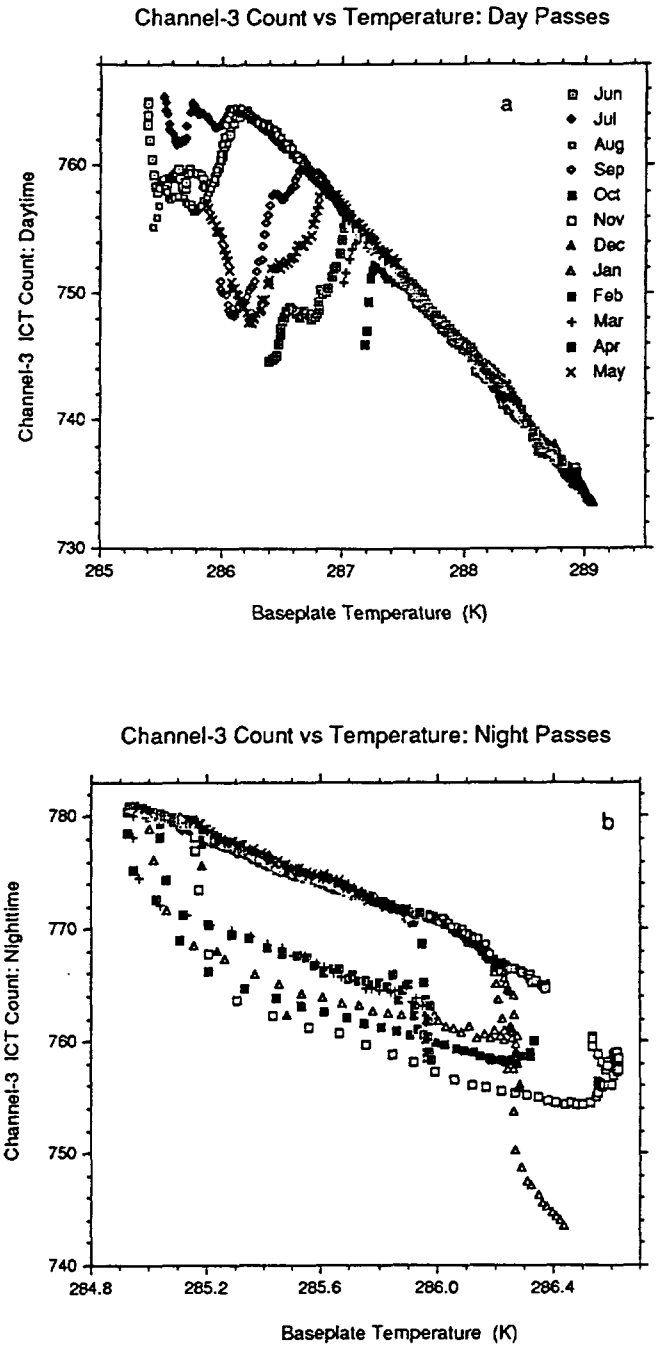

Fig. 15. Channel 3 ICT count versus base plate temperature over a full year. (*a*) Twelve daytime passes sampled at 1-monthly intervals. For 8 months, March through October, there is a substantial distortion in the curve caused by spurious radiance in channel 3. The daytime curves for channels 4 and 5 are clear of distortion (see Figures 16*a* and 17*a*) suggesting that sunlight is affecting calibrations in this channel. (*b*) Channel 3 nighttime passes sampled at 1-monthly intervals. Nighttime calibration instabilities occur during the southern hemisphere summer months (October through March) when the satellite crosses the night-day boundary into full sunlight. Similar disturbances are seen in the channel 4 and 5 night records (see Figures 16*b* and 17*b*), although of smaller magnitude.

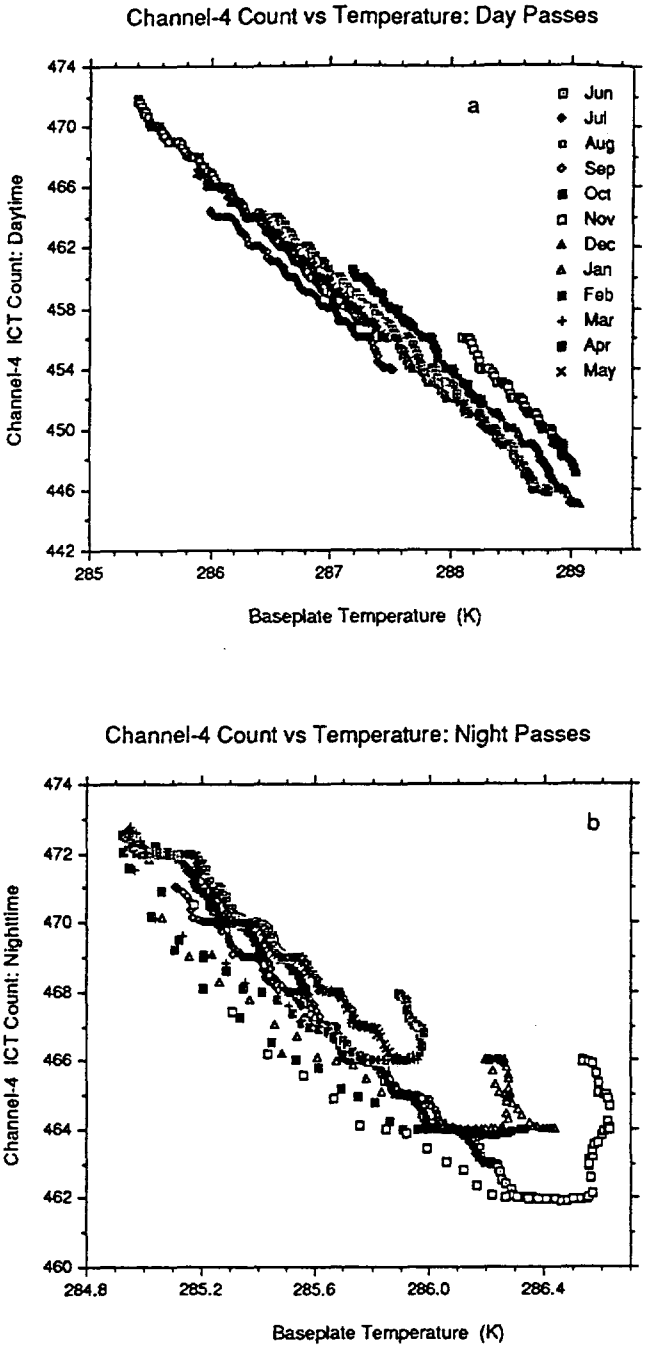

Fig. 16. Channel 4 ICT count versus base plate temperature over a full year. (*a*) Twelve daytime passes sampled at 1-monthly intervals. The curves follow the expected near-linear trends; there is no sign of the solar radiance distortions evident in channel 3 daytime passes. (*b*) Channel 4 nighttime passes sampled at 1-monthly intervals. Night pass calibration instabilities occur during the southern hemisphere summer months (October through March) when the satellite crosses the night-day boundary into full sunlight. The deviations away from the expected trend line are thought to be due to the difference in thermal response time of the radiometer compared with that of the PRT sensors which measure the bulk ICT temperature (see Figure 18).

following graphs and that some of the features are functions of time or spacecraft position rather than temperature.

To test our solar radiance hypothesis, we then examined 48 NOAA 11 passes sampled over a full year: two daytime passes and two nighttime passes for each month for the period June 1990 to May 1991 (see Figure 15*a*). Of the 24 day-time passes, 16 passes contained channel 3 radiance anomalies; only the months of November through February were free of daytime artifacts. These anomalies always coincided with Sun elevation angles relative to the satellite which were lower than about 15°

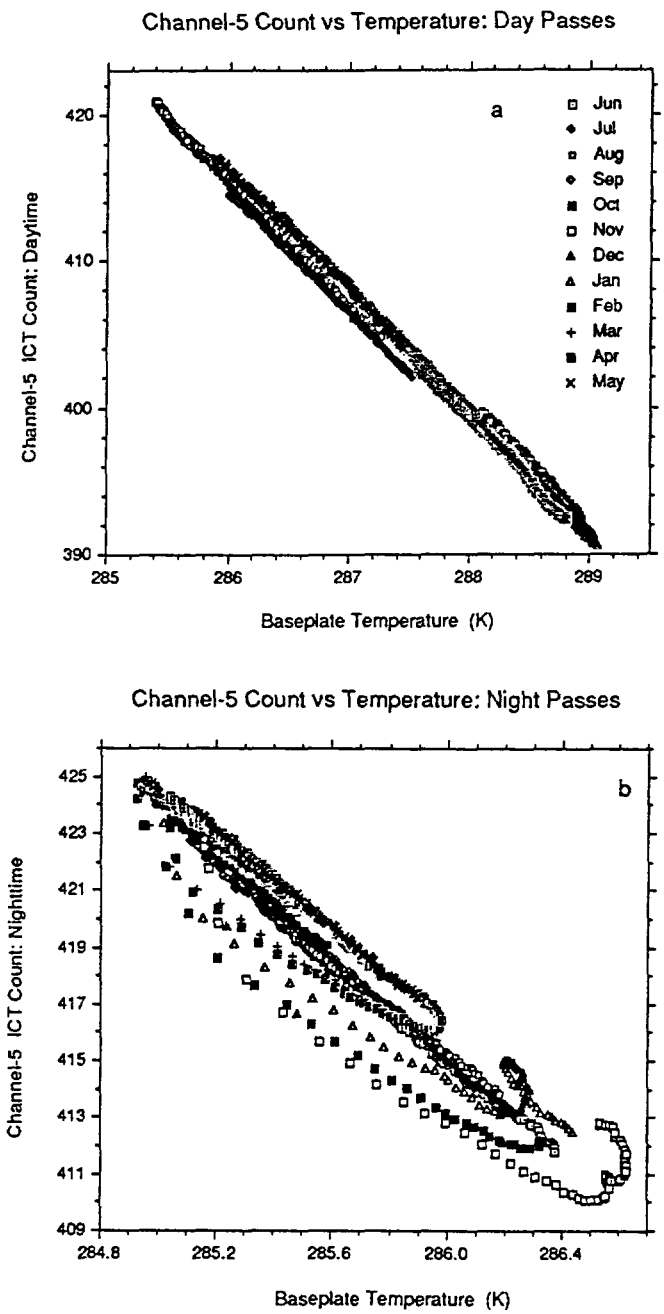

Fig. 17. Channel 5 ICT count versus base plate temperature over a full year. (*a*) Twelve daytime passes sampled at 1-monthly intervals. The curves follow the expected near-linear trends; there is no sign of the solar radiance distortions evident in the channel 3 daytime passes. (b) Channel 5 nighttime passes sampled at 1-monthly intervals. Nighttime calibration instabilities occur during the southern hemisphere summer months (October through March) when the satellite crosses the night-day boundary into full sunlight.

above the tangent plane; for Sun elevation angles higher than this, the calibration disturbances in channel 3 disappeared. At the time of the anomalies, the solar azimuth (Sun angle measured counterclockwise in the tangent plane from the satellite velocity vector) was typically in the range 25° to 45°, which placed the Sun on the same side as the AVHRR instrument. This leads us to suspect that at low solar elevations, a small amount of sunlight leaks into the optical path of the radiometer. Without access to a model of the satellite, it is difficult to know how this might occur; perhaps there is reflection from the edge of the scanning mirror when it is aligned towards the ICT, or even, at very low solar elevations, direct illumination onto and reflection from the imperfectly "black" ICT itself.

To demonstrate that this ICT reflection explanation is at least numerically feasible, we computed the total solar radiance across the channel 3 filter function by evaluating equation (3) for a blackbody radiating at 5800 K (the Sun), then scaled the result by the square of the ratio (radius of Sun : radius of Earth orbit about the Sun) to obtain the radiance at the top of the atmosphere [*Liou*, 1980, p.41 and exercise 2.1, p.48]. The result was 5.27 $mW/(m^2\,sr\,cm^{-1})$. We converted this to channel 3 counts by dividing by the channel 3 slope of –0.00149 radiance units per count (see Figures 12*b* and *c*), and then multiplying by the estimated (upper limit for) reflectivity of the ICT blackbody, (1 – 0.994 = 0.006), giving a predicted upper limit for the count displacement of –21.2 counts. From Figure 12*c* we estimate the actual count discrepancy at –17 counts. (Similar solar calculations for channels 4 and 5 predict a deviation of about –0.03 counts, well below the limits of detectability.)

If these distorted calibrations are taken at face value, they will lead to scene brightness temperature estimates in channel 3 which, for the case shown in Figure 12*a*, could be as much as 1.7°C too low. To illustrate, consider a scene pixel which happens to produce a channel 3 count of 747. In the absence of distortion, this count value would intersect the (extrapolated, lower) count-versus-temperature curve at about 288 K, whereas on the distorted curve the intersection would occur at 286.3 K, an error of –1.7°C. As a rough but useful guide, the slope of the radiometer response in the mid temperature range is about 10 counts $°C^{-1}$, so a count depression of Δx implies a temperature error of magnitude $\Delta x/10$.

Also evident in Figures 12*a* and 12*b* is a clear demarcation between the day and night calibration curves. Our conjecture is that there has been a change in instrument sensitivity arising from a change in the background radiance flux on the detectors. The standard dynamic calibration procedures will track, and, we hope, completely compensate for these changes. However, at the day-night transition itself, the success of dynamic calibrations is questionable (this is discussed in greater detail later in this section).

Figure 12*b* shows calibration slope $g = R/(\mathrm{IC} - \mathrm{SC})$ versus internal-target count for the four April 30 passes. A distinct day-night clustering about a pair of average values is observed, while the solar-contaminated data stand out clearly. Using these average slopes, a pair of linear counts-to-radiance equations were derived, which are shown in Figure 12*c* superimposed on the data of Figure 12*a* (the brightness temperatures have been converted to channel 3 radiances). The satisfactory agreement indicates that use of the uncontaminated data to derive a single slope figure for a pass has merit and should certainly be considered as a method for working around daytime calibrations afflicted with solar contamination problems.

Figures 13*a* and 14*a* show the channel 4 and 5 counts, respectively, as a function of ICT temperature for the same April 30 passes. As in Figure 12, counts and temperatures have been averaged in blocks of 50 lines, yet in the case of channel 4 the underlying digital-count steps can be clearly discerned indicating that this channel has a better noise performance than channels 3 and 5. As expected, there is no evidence of solar contamination in these thermal infrared channels.

Figures 13*b* and 14*b* show linear slopes for channels 4 and 5 as a function of ICT count. Unlike channel 3, there is no obvious clustering about an average value. Instead, the slope variations for both channels display an upward trend. It is tempting to speculate that on the basis of equation (12), the gradient of these calibration-slope-versus-internal-target-count graphs might provide an in-flight estimate of a, the channel curvature. Unfortunately, this requires that γ, the second root of the fundamental count-versus-radiance quadratic (equation (10)), remain constant. This quadratic has three degrees of freedom: a, SC, γ. We have already found that SC is substantially constant. If curvature a is assumed to be fixed, then any variations in the in-flight calibration curve must arise from variations in γ. Since for channel 4 the locus of day and night calibration points form two disjoint curves, it follows that for fixed a, γ has varied between day and night, and may even vary during the course of a single pass. Our model for this behavior pictures the radiance-versus-count transfer function (e.g., Figure 3) as a parabola of rigid shape (i.e., constant a) whose left branch is free to slide through the count-axis at a fixed point SC, so that the second count axis intersection, γ, can also vary freely.

The whole-year suite of 48 calibration trajectories, radiometric count versus baseplate temperature, for all three channels are shown in Figures 15 through 17. While the solar distortions in the channel 3 daytime passes have already been discussed, the graphs for the nighttime passes reveal some surprising deviations in all three channels. We find that for the Hobart ground station, calibration discrepancies occur in night passes during the southern hemisphere summer months (November through March): when the satellite crosses the terminator into the sunlight during a descending pass, the PRT measurements of the ICT temperature suddenly rise, but this temperature change is apparently anticipated by about 16 s (the time for two 50-line-averaged calibration records) in the radiometric-count curves (see Figures 18 and 19). All three infrared channels behave in this way. This is apparently due to the structure of the ICT. Surface heating due to incident sunlight will be immediately detected by the radiometer, but the PRTs are located somewhere inside the ICT and it will take some time for the heat to diffuse through to them. Channel 3 is more strongly affected by thermal calibration transients than either of the other infrared channels, probably because the solar elevation at transition will necessarily be low, enabling sunlight to leak into the optical path, thereby allowing reflected solar radiance to exacerbate the count depression in this channel.

For the Jan 2, 1991 pass illustrated in Figures 18 and 19, the initial thermal shock errors of about 1.0°, 0.4°, and 0.4°C respectively for channels 3, 4, and 5 can be almost completely eliminated by advancing the temperature records, relative to the radiometric-count records, by about 16 s (Figures 19*c* and 19*d*). It is clear that channel 3 is beset by more than just thermal inertia problems, since these timing adjustments do not remove the distortions evident during the middle and final sections of the count-versus-temperature trajectory. We suspect that sunlight leakage into the radiometer is the cause, and that the peaks and troughs within the distorted section are shadow or reflection patterns generated by the movement of the Sun relative to the underparts (e.g., antenna systems) of the spacecraft. We find that such distortion features are quite consistent in shape from pass to pass. The large count depression displayed at the end of the Jan 2 night-day pass is of similar magnitude to that shown near the beginning of the April 30 day pass (Figure 12*a*), and will result in a channel 3 brightness temperature which is about 2°C low.

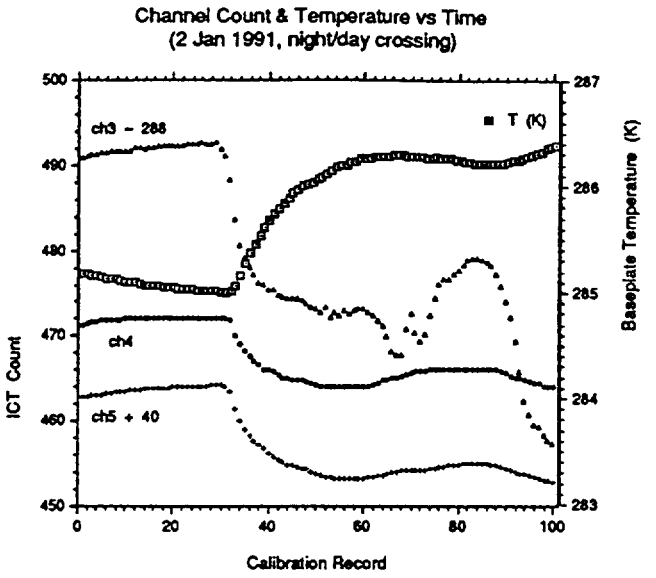

Fig. 18. Time series plot of radiometric count and base plate temperature for a night-pass (Jan 2, 1991) exhibiting thermal instabilities in the calibration curves. The horizontal axis is calibration record number; there are 100 such records in the pass. At about record 30 the satellite crosses the night-day terminator into full sunlight as indicated by the subsequent decline in the radiometric count plots. The base plate temperature starts to rise somewhat later, at record 32, and its rate of change is slower than that of the radiometer. This difference in thermal response times causes the interesting calibration trajectories shown in Figure 19*a*. (The channel 3 and 5 counts have been adjusted as indicated to allow simultaneous display.)

5. CONCLUSIONS AND RECOMMENDATIONS

In this paper we have examined the philosophy and methodologies of the preflight and in-flight calibrations for the AVHRR infrared channels. We find that the nonlinearity corrections required for channels 4 and 5, when expressed in radiance space, can be written in a simple form which depends only on the base plate radiance. This alternative formulation obviates the need to interpolate in the tables of brightness temperature corrections and reduces the computation effort required to produce corrected radiances. Users now have a choice of three methods for the application of the nonlinearity corrections: they can either (1) continue to follow the NESDIS practice of applying temperature corrections to the apparent scene temperatures, (2) perform the equivalent operation in radiance space by interpolating within the radiance correction columns presented in Tables 2 through 9, or (3) assume the corrections are best represented by smooth radiance-space parabolas, and utilize the k coefficient method of equation (7) as described in this paper. If, for future NOAA satellites launches, NESDIS were to publish the original count-versus-radiance calibration curves, users could extract the quadratic curvature term a and thereafter use the more direct a curvature method of equation (13) to calculate the NLCs.

It seems that our assumption of constant curvature for channels 4 and 5 may only be accurate to first order: recently, Weinreb (personal communication, 1991) pointed out that

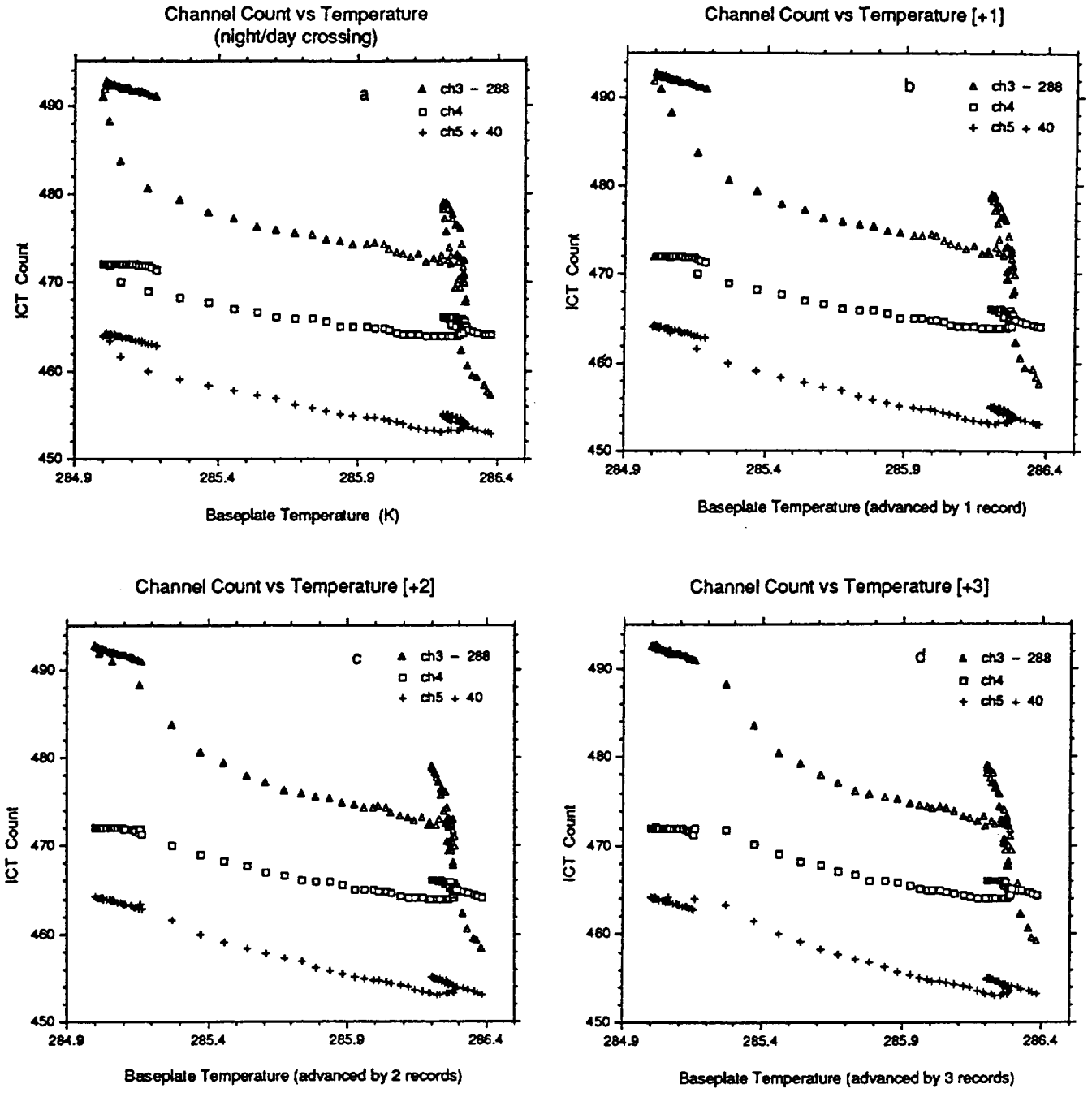

Fig. 19. Radiometric count as a function of base plate temperature for the Jan 2, 1991 night pass. The calibration trajectories display spurious kinks and loops arising from the slower response time, relative to the radiometer response, of the PRT sensors which measure the temperature of the base plate. These loops can be collapsed by advancing the temperature readings by two or three calibration records to compensate. (*a*) Count versus temperature with no lag adjustment. (*b*) Count versus temperature advanced by one record (~8 s). The calibration trajectories begin to collapse into a simpler form linking the upper and lower "stable" temperature regions. (*c*) Count versus temperature advanced by two records (~16 s). The upper portions of the channel 4 and 5 trajectories have collapsed into the main trend; the lower loop seems to have a longer time constant associated with it. (*d*) Count versus temperature advanced by three records (~24 s). The upper portion of the channel 3 trajectory has collapsed into the main trend; channels 4 and 5 are now overcompensated. The remaining deviations in channel 3 possibly arise from solar radiance reflected from the internal calibration target.

there may in fact be slight changes to the calibration curve itself as the ICT temperature varies. This could occur if the ICT temperature variations are associated with temperature changes in any AVHRR components which radiate to the detectors, since the nonlinearity is a (weak) function of background flux on the detectors. We are presently investigating this possibility.

Our examinations of the in-flight records for NOAA 11 exposed two events which can compromise the quality of the calibrations: solar distortion in channel 3 for low Sun-elevation

angles, and thermal transients affecting all three infrared channels when the spacecraft crosses the night-day boundary into full sunlight. Solar distortion lowers the apparent brightness temperature in channel 3 by up to 2°C; this error persists for as long as the solar elevation angle, relative to the satellite, is lower than about 15° above the tangent plane. In contrast, the thermal transient deviations produce temperature depression errors which decay to zero with a time-constant of about 40 s. The maximum error is typically –1°C in channel 3, and –0.4°C for channels 4 and 5.

Channel 3 seems to be much more sensitive to thermal transients and is the only infrared channel which can respond to stray reflected sunlight. For this channel at least, continuous unqualified dynamic calibrations are risky. A safer procedure would be to plot the channel 3 radiance-versus-count calibration curve for each pass, inspect for deviations from the expected trend, and, if necessary, use averaged slopes and intercepts extracted from known good portions of the curve for extrapolation into the contaminated section. This technique was demonstrated in Figure 12*c*.

Some users may prefer to ignore thermal shock perturbations in channels 4 and 5 because the effect is transient, and the magnitude of the error is at the threshold of significance. However, if the perturbation coincides with a portion of the pass which is critical to the user, we suggest the timing adjustments shown in Figures 19*a* to 19*d* as a possible correction method.

Acknowledgments. This work was completed during a 5-month sabbatical stay (by M.S.R. and A.S.R.) at CSIRO Marine Laboratories, Hobart, Tasmania, and these authors wish to express their gratitude to the members of the Remote Sensing group whose efforts made this work possible. In particular, we wish to thank Carl Nilsson for providing access to AVHRR data and for stimulating many useful and entertaining discussions regarding calibration techniques. Credit is also due to Paul Tildesley, Ross Jones, Ken Suber, and Chris Rathbone for their help in identifying the sources of the various calibration surprises. We thank D. R. White of the New Zealand DSIR Temperature Standards Laboratory for furnishing the CODATA reference for the fundamental physical constants, and M. P. Weinreb of the NOAA/National Environmental Satellite, Data, and Information Service for many helpful comments.

REFERENCES

Brown, O. B., J. W. Brown, and R. H. Evans, Calibration of advanced very high resolution radiometer infrared observations, *J. Geophys. Res.*, *90*, 11,667–11,677, 1985.

Cohen, E. R., and B. N. Taylor, The 1986 CODATA recommended values of the fundamental physical constants, *J. Res. Natl. Bur. Stand.*, *92*, 2, 1987.

Lauritson, L., G. J. Nelson, and F. W. Porto, Data extraction and calibration of TIROS-N/NOAA radiometers, *NOAA Tech. Memo. NESS 107*, 72 pp., Natl. Environ. Satell. Data and Inf. Serv., Washington, D.C., 1979.

Liou, K.N., An Introduction to Atmospheric Radiation, *International Geophysics Series*, vol. 26, chap. 2, Academic Press, 1980.

Norwood, V. T., and J. C. Lansing, Electro-optical imaging sensors, in *Manual of Remote Sensing*, vol. I, chap. 8, American Society of Photogrammetry, 1983.

Planet, W. G. (Ed.), Data extraction and calibration of TIROS-N/NOAA radiometers—Rev 1, *NOAA Tech. Memo. NESS 107* (Revised), Natl. Environ. Satell. Data and Inf. Serv., Washington, D.C., 1988.

Schwalb, A., The TIROS-N/NOAA A–G satellite series, *NOAA Tech. Memo. NESS 95*, 75 pp., Natl. Environ. Satell. Data and Inf. Serv., Washington, D.C., 1978.

Weinreb, M. P., G. Hamilton, S. Brown, and R. J. Koczor, Nonlinearity corrections of advanced very high resolution radiometer infrared channels, *J. Geophys. Res.*, *95*, 7381–7388, 1990.

S. Clift, CSIRO Marine Laboratories, P.O. Box 1538, Hobart, Tasmania 7001, Australia.

D. A. Steyn-Ross and M. L. Steyn-Ross, Physics Department, University of Waikato, Private Bag 3105, Hamilton, New Zealand.

(Received July 15, 1991;
revised December 9, 1991;
accepted December 9, 1991.)

CORRECTED VERSION

6th AUSTRALASIAN R.S. CONF.
WELLINGTON, N.Z., NOV.'92

A MULTI-LEVEL ELECTRONIC DATABASE FOR DOCUMENTATION AND DISSEMINATION OF TIME-DEPENDENT NOAA-AVHRR CALIBRATION COEFFICIENTS FOR THE SOLAR REFLECTIVE CHANNELS

P.M. Teillet[1] and B.N. Holben[2]
[1]Canada Centre for Remote Sensing
588 Booth Street, Ottawa, Ontario, Canada K1A 0E4
[2]NASA Goddard Space Flight Center (Code 923)
Greenbelt, Maryland, USA 20771

ABSTRACT

Recent requirements for more accurate absolute radiometric calibration of NOAA AVHRR data have given rise to a variety of investigations concerned with inflight calibration of the two solar reflective channels. In order to make available and document time histories of AVHRR calibration coefficients, a multi-level electronic database has been implemented. This article describes the spreadsheet and provides an overview of calibration methods and formulations. Specific recommendations are made toward the operational calibration of AVHRR image data, including the establishment of a procedure for the reliable and timely determination of calibration coefficients for the visible and infrared AVHRR channels.

INTRODUCTION

Digital image data from the Advanced Very High Resolution Radiometers (AVHRR) on-board the National Oceanic and Atmospheric Administration (NOAA) series of satellites have provided valuable, continuous regional and global coverage since 1979 when the first instrument was launched on the NOAA-6 platform. The increasing use of the visible and near-infrared AVHRR channels for monitoring vegetation conditions and mapping land cover (Cihlar et al., 1990) has prompted new research and development in many areas, including improved understanding of the optical characteristics of the instrument and quantitative image correction methodologies (Teillet, 1992).

The functional requirements and related design criteria for the AVHRR did not specify on-board radiometric calibration and so only preflight calibrations have ever been made by NOAA. Requirements for more accurate absolute radiometric calibration of the solar reflective channels have lead to the development of a variety of techniques to overcome the lack of on-board calibration. These investigations have shown that preflight calibrations are inappropriate for post-launch data acquired by nearly all the AVHRR instruments, with substantial decreases in sensitivity with time after launch compared to prelaunch values. The various approaches show comparable trends over time but the results are not necessarily in close agreement.

It is recognized that there is a need to make available time histories and the latest values for AVHRR calibration coefficients as well as to decrease the time lag between research results and their dissemination to users (Faizoun, 1992; Townshend, 1992; Abel, 1990a; Teillet, 1990). While NOAA has recently established a calibration group to address these problems, the authors in the interim have developed a multi-level electronic database specifically for the documentation and dissemination of calibration coefficients for AVHRR channels 1 and 2. This paper discusses AVHRR calibration issues and describes the multi-level electronic spreadsheet. Specific recommendations are made

Tech. Team Mtg - 12/3/92
Attach. # 5 (2 of 2)

towards the operational implementation of AVHRR radiometric calibration, including the establishment of a calibration procedure which can provide the reliable and timely coefficients urgently need internationally for vegetation monitoring and other applications.

OVERVIEW OF CALIBRATION METHODS

Standard Targets

One approximate approach is to select water bodies and forested areas near nadir and assume that they have the same reflectance from day to day throughout most of the vegetation development period (Manore and Brown, 1986). In the same vein, dark counts from space views and the White Sands National Monument area in New Mexico have been used as calibration targets by Frouin and Gautier (1987).

Cloud Radiance Approach

Another approach uses a ground radiometer to measure cloud radiance on an overcast day and a delta-Eddington cloud layer model to infer the irradiance incident on the cloud tops imaged by the AVHRR (Justus, 1988).

Underflight Method

One approach being used is to fly a well-calibrated spectroradiometer operating in the 0.425μm to 1.00μm region over White Sands (Abel et al., 1988; Smith et al., 1989). The U-2 flight at 19 km altitude is timed to coincide with the satellite overpass and the viewing geometry is arranged to match that of the AVHRR sensor. An integrating sphere is used to calibrate the aircraft instrument before and after each flight.

White Sands Approaches

Three different approaches are described by Teillet et al. (1990) for the absolute radiometric calibration of the two solar reflective channels of the AVHRR sensors. Method 1 relies on field measurements and image data from another calibrated satellite sensor that acquired high-resolution imagery on or near the day of the AVHRR overpass. Method 2 makes no reference to another sensor and is essentially an extension of the reflectance-based calibration method developed at White Sands for the in-orbit calibration of Landsat Thematic Mapper (TM) and SPOT High Resolution Visible (HRV) data (Slater et al., 1987). Method 3 achieves a calibration by reference to another satellite sensor, but it differs significantly from the first approach in that no ground reflectance and atmospheric measurements are needed on overpass day. Instead, a standard data set of atmospheric conditions is assumed to approximate the actual atmosphere and historical bidirectional reflectance data are used to adjust for differences in illumination and viewing geometry.

Calibration Over Ocean

A method used by Kaufman and Holben (1992) and Santer and Sharman (1992) for AVHRR and by Fraser and Kaufman (1986) for GOES-VISSR imagery is based on measurements of the radiance over the ocean, out of the glint direction. Under clear sky conditions, the at-satellite radiance can be modeled to $\pm$ 10% absolute accuracy (Kaufman and Holben, 1992). Since the molecular scattering is much weaker in the near-IR, ocean glint is used to transfer the calibration of the visible band to the near-IR

band, owing to the spectral independence of the glint.

Calibration Over Deserts

Deserts that are invariant in time can be used to monitor the temporal stability of the calibration. In order to use the desert for an absolute calibration, the desert spectral reflectance must be determined in each particular instance. Frouin and Gautier (1987) used laboratory measurements of the White Sands reflectance as the basis for the satellite calibration. Teillet et al. (1990) used ground measurements of the reflectance of the alkali flats area at White Sands and the nearly simultaneous image data from high resolution Landsat Thematic Mapper to derive the surface reflectance during the AVHRR observation.

Several other variations of the desert approach have been investigated. The simplest restricts the illumination and viewing geometries over carefully selected, bright sites in the Libyan Desert (Holben et al. 1990; Kaufman and Holben, 1992). Viewing geometry is chosen to be near nadir to remove sun-scanner azimuthal dependence which requires an observation every satellite repeat cycle (~9 days). Visible and near-infrared channel data are taken for a two-month period near the autumnal and vernal equinoxes in each year. Image data are visually screened for cloud and aerosol contamination after which mean and standard deviations are computed for each time period resulting in a time-dependent gain response. The method is calibrated by anchoring a relative response for a single date to an absolute value derived from an absolute calibration method.

Staylor (1990) and Santer and Sharman (1992) monitor a large area in the Libyan desert using all of the data available during the aforementioned time periods for each year of AVHRR acquisition. They empirically account for scan angle effects and determine a time-dependent relative calibration for the visible and near-infrared channels.

Using the ISCCP data base, Brest and Rossow (1991) make use of a generalization of the desert approach by selecting data over 8 surface types and 28 targets globally (deserts being only one) for all times of year and all viewing geometries. This method requires a rather sophisticated analysis to remove geometric effects and seasonal variations in surface cover reflectance, the entire AVHRR data base, and enormous computing power. The result is a relative calibration method that will respond to non-linearity in the system.

RADIOMETRIC CALIBRATION NOTATION

The radiometric calibration from 10-bit digital signal level to radiance units is accomplished by means of the following equation:

$$L^*_i = (D_i - D_{oi})/G_i \quad , \tag{1}$$

where L^* = radiance ($Wm^{-2}sr^{-1}\mu m^{-1}$), D = digital signal level (counts on a 10-bit scale), D_o = calibration offset coefficient (counts), G = calibration gain coefficient [counts/($Wm^{-2}sr^{-1}\mu m^{-1}$)], and the subscript i refers to AVHRR channel number (1 or 2). A common notation for the gain coefficient is the inverse factor

$$\alpha_i = 1/G_i \quad , \tag{2}$$

where the gain factor α_i is in units of $Wm^{-2}sr^{-1}\mu m^{-1}count^{-1}$.

The prelaunch calibration coefficients given by NOAA (Kidwell, 1991; Lauritson et al., 1979) are expressed in terms of effective normalized albedo A (in percent) such that

$$A_i = \gamma_i(D_i - D_{oi}) \quad , \tag{3}$$

where $\gamma_i = 100\pi/(E_{oi}G_i) = 100\pi\alpha_i/E_{oi}$ and E_{oi} is the exo-atmospheric solar irradiance ($Wm^{-2}\mu m^{-1}$) for channel i (Table 1). Prelaunch calibration coefficients for recent AVHRR sensors are discussed in articles by Abel (1990b) and Price (1988a,b; 1987).

TABLE 1: Exo-atmospheric solar irradiances (based on Neckel and Labs (1984)) and equivalent bandwidths for AVHRR channels 1 and 2.

NOAA	$E_o(Wm^{-2}\mu m^{-1})$		$\Delta\lambda(\mu m)$	
	ch 1	ch 2	ch 1	ch 2
6	1632	1035	0.1086	0.2228
7	1642	1021	0.1071	0.2606
8	1606	1044	0.1123	0.2295
9	1620	1036	0.1172	0.2395
10	1648	1026	0.1079	0.2226
11	1622	1048	0.1129	0.2290
12	1615	1032	0.1227	0.2219

CALIBRATION STATUS

Calibration Coefficients

It is recommended that the zero radiance counts be used for the offset D_{oi} , as approximated by the deep space view which occurs every scan. The deep space values change very slowly with time and remain close to the prelaunch values.

Almost all AVHRR instruments studied using the aforementioned calibration approaches have shown a substantial decrease in sensitivity after launch compared to prelaunch gain coefficients. The variety and frequency of changes in the AVHRR calibration gain coefficients suggest that an infrastructure be established in which frequent calibration updates are made and the results passed on to the user community within a few weeks.

Responsibility for current knowledge of the calibration of AVHRR channels 1 and 2 has resided with the data user. Although several research groups have been or are working on AVHRR calibration, the various methods have yet to be studied in a coordinated fashion and the results are often intermittent and become available months to years after the initial data acquisition. Consequently, most users have little or no knowledge of the best estimates available for calibration coefficients and end up relying on prelaunch values. On the other hand, a variety of inflight calibration techniques have been developed, allowing a more thorough exploration of AVHRR sensor characteristics and assessments of the most appropriate calibration procedures.

Multi-Level Spreadsheet

Calibration coefficients for AVHRR channels 1 and 2 have been compiled from as many sources as possible and a multi-level electronic database has been implemented. One level of information in the spreadsheet contains entries that have been obtained exclusively from the peer-reviewed literature. Another level contains all available results, including preliminary values not yet peer reviewed, in order to allow timely, although potentially risky, access to calibration information. It would also allow investigators in the field to compare their results relatively quickly and easily to the others in the data set. A third, key part of the database includes time-dependent characterizations recommended for use on operational AVHRR processing systems.

The spreadsheet includes recommended time-dependent calibrations for the AVHRR sensors on NOAA-6 through to NOAA-12 (Tables 2 and 3). The recommendations for the odd-numbered satellites are based on piecewise linear fits of the desert results of Holben and collaborators. This method was chosen for two reasons mainly. Firstly, many of the calibration approaches have not been fully validated or are more approximate in nature to begin with. Secondly, there is still insufficient correspondence between the nominally more accurate calibrations based on White Sands techniques.

Piecewise linear fits are recommended for operational use because, unlike the situation for polynomial fits for example, they will not change retroactively when new data are added at the end of the time series. There is also continuity between each linear segment. In general, the pieces have been chosen to encompass calendar years in order to avoid changes during the growing season in the northern hemisphere. Because the piecewise linear functions have been established for the first time, they are largely based on polynomial fits. The polynomial approach can be useful for quick calculations once a particular AVHRR instrument is no longer acquiring data, but it is less practical for operational systems.

A copy of the calibration spreadsheet can be made available upon request. A large proportion of the calibration gain coefficients contained in the database has also been tabulated recently by Che and Price (1992). In their article, Che and Price provide linear characterizations of the time-dependence of gain values based on all available data points for each of the NOAA-7, -9, and -11 AVHRRs. It is also worth noting that the analysis of Che and Price (1992), as well as that of D'Iorio et al. (1991), examine the significant effects of calibration on vegetation index calculations.

Level of Consensus

The methodologies described in this article and by Teillet (1992) have been implemented in a production system in Canada to geocode NOAA AVHRR imagery and to use those data to construct cloud-free NDVI composites for the entire Canadian land mass (Robertson et al., 1992; Erickson et al., 1991). In the United States, the EROS Data Center has also adopted the piecewise linear representations of the time dependence of AVHRR calibration coefficients as given in Tables 2 and 3 (Eidenshink, personal communication). Others in the international community have indicated their interest in following the same procedures (Townshend, 1992; Faizoun, 1992).

Numerous agencies in various countries are embarking on large-scale land cover change investigations based on AVHRR data, and it is important to standardize the methodologies involved as much as possible as the remote sensing community works towards continental and global products. The recent completion of a North American composite using common radiometric calibration procedures in Canada and the United States (Morasse and D'Iorio, 1992; Cover Images: Photogrammetric Engineering and Remote Sensing (June, 1992), Canadian Journal of Remote Sensing (July, 1992)) and the global 1-km AVHRR data set being promoted by the International Geosphere-Biosphere Program (IGBP) (Townshend, 1992) are two developments in this standardization process.

TABLE 2: Coefficients for piecewise linear representations of the time dependence of AVHRR calibration gain coefficients, where gain = A•(day#) + B. Radiance is in units of $Wm^{-2}sr^{-1}\mu m^{-1}$.

Effective Date	Post-launch Day #	A (counts/radiance)/day		B (counts/radiance)	
		channel 1	channel 2	channel 1	channel 2
NOAA-6 AVHRR					
1979-06-27	0	0	0	1.79	2.83
NOAA-7 AVHRR					
1981-06-23	0	-2.08E-04	-5.92E-04	1.63	2.52
1982-01-01	192	-1.77E-04	-4.36E-04	1.62	2.49
1983-01-01	557	-1.36E-04	-2.31E-04	1.60	2.38
1984-01-01	922	-1.02E-04	-6.21E-05	1.57	2.22
1984-08-22	1156	0	0	1.45	2.15
NOAA-8 AVHRR					
1983-03-28	0	0	0	1.83	2.71
NOAA-9 AVHRR					
1984-12-12	0	-2.78E-04	-3.54E-04	1.74	2.48
1986-01-01	384	-2.55E-04	-2.53E-04	1.73	2.44
1987-01-01	749	-2.33E-04	-1.54E-04	1.71	2.37
1988-01-01	1114	-2.15E-04	-7.40E-05	1.69	2.28
1988-08-19	1345	0	0	1.41	2.18
NOAA-10 AVHRR					
1986-09-17	0	-6.56E-04	-8.75E-04	1.72	2.27
1988-02-10	511	0	0	1.39	1.82
NOAA-11 AVHRR					
1988-09-24	0	7.36E-06	-2.84E-04	1.67	2.50
1989-01-01	99	1.49E-05	-1.71E-04	1.67	2.49
1990-01-01	464	2.68E-05	6.20E-06	1.66	2.41
1991-01-01	829	3.70E-05	1.59E-04	1.66	2.28
1991-09-19	1091	0	0	1.70	2.45
NOAA-12 AVHRR					
1991-05-14	0	0	0	1.87	2.95

TABLE 3: Coefficients for piecewise linear representations of the time dependence of AVHRR calibration offset coefficients, where offset = C•(day#) + D.

Effective Date	Post-launch Day #	C (counts)/day		D (counts)	
		channel 1	channel 2	channel 1	channel 2
NOAA-6 AVHRR					
1979-06-27	0	0	0	38.0	40.0
NOAA-7 AVHRR					
1981-06-23	0	-5.87E-04	-1.02E-03	36.1	38.1
1982-01-01	192	-5.28E-04	-9.29E-04	36.1	38.1
1983-01-01	557	-4.50E-04	-8.12E-04	36.1	38.0
1984-01-01	922	-3.86E-04	-7.15E-04	36.0	37.9
1984-08-22	1156	0	0	35.5	37.1
NOAA-8 AVHRR					
1983-03-28	0	0	0	40.2	43.0
NOAA-9 AVHRR					
1984-12-12	0	-1.85E-04	-1.53E-03	38.0	40.3
1986-01-01	384	-2.01E-04	-1.09E-03	38.0	40.1
1987-01-01	749	-2.16E-04	-6.57E-04	38.0	39.8
1988-01-01	1114	-2.29E-04	-3.04E-04	38.0	39.4
1988-08-19	1345	0	0	37.7	39.0
NOAA-10 AVHRR					
1986-09-17	0	-9.21E-04	-8.12E-04	37.0	37.7
1989-07-24	1041	0	0	36.1	36.9
NOAA-11 AVHRR					
1988-09-24	0	0	0	40.0	40.0
NOAA-12 AVHRR					
1991-05-14	0	0	0	40.0	40.0

CONCLUSIONS AND RECOMMENDATIONS

An electronic bulletin board should be established to document and disseminate NOAA AVHRR calibration information, particularly for the solar reflective channels. The central feature of such a bulletin board would be a multi-level spreadsheet similar to the one described in this paper for time-dependent calibration coefficients. It is also strongly suggested that NOAA, given its ownership of the AVHRR series, be responsible for ensuring the independent evaluation of calibration results on an ongoing basis and ensuring the timely inclusion of a recommended set of time-dependent calibrations as part of the electronic bulletin board.

It is recommended that the international community sponsor a calibration monitoring program using the resources of member receiving stations. The following points should be implemented in this activity:

(i) The international community should support the acquisition and archiving of data

acquired over desert calibration sites by all active AVHRR instruments by member receiving stations.

(ii) A hybrid desert method similar to those of Holben et al. (1990) and Santer and Sharman (1992) should be used. Although relative, the desert approach is simple, inexpensive, and provides the best possibility for timely determination of calibration coefficients.

(iii) Automated solar radiometer stations should be established at the desert sites to monitor atmospheric properties (especially aerosol and water vapour) and thus allow subsequent correction for their effects.

(iv) Periodic field missions are required to document surface reflectance properties and uniformity of the sites. An absolute calibration using an updated version of the methods of Teillet et al. (1990) would be made at such times as an anchor point for the ongoing desert calibrations.

(v) With the added ground sorties and automated solar radiometry components, the proposed methodology could be used to determine AVHRR calibration gain coefficients on a frequent basis (every nine days, for example). Nevertheless, how to go about the near-real-time update of coefficients for use on an operational processing system would remain a problematic issue.

It is strongly recommended that a single group take responsibility for the radiometric calibration of the NOAA AVHRR sensors. The instruments belong to NOAA and, therefore, it is suggested that calibration should be NOAA's responsibility. However, because of the international community's involvement in the calibration, it is proposed that the Calibration/Validation Working Group of the Committee on Earth Observations Satellites (CEOS), which has an international base, take an active role in working with the NOAA calibration group and other investigators to ensure the acquisition, collation, evaluation, documentation, and dissemination of calibration data. Ultimately, this includes seeking sponsorship for a routine calibration methodology, analysis and publication of results, and maintenance of an electronic bulletin board.

ACKNOWLEDGEMENTS

The authors wish to thank B. Guindon and B. Robertson for valuable discussions, G. Fedosejevs for technical assistance, and A. Kalil for wordprocessing of the article.

REFERENCES

Abel, P., Editor, (1990a). Report of the Workshop on Radiometric Calibration of Satellite Sensors of Reflected Solar Radiation, March 27-28, 1990. NOAA Technical Report NESDIS 55, National Oceanic and Atmospheric Administration, 33 pp. Washington, D.C.

Abel, P. (1990b). Prelaunch calibration of the NOAA-11 AVHRR visible and near IR channels. Remote Sensing of Environment, 31:227-229.

Abel, P., Smith, G.R., Levin, R.H. and Jacobowitz, H. (1988). Results from aircraft measurements over White Sands, New Mexico, to calibrate the visible channels of spacecraft instruments. Recent Advances in Sensors, Radiometry, and Data Processing for Remote Sensing. Proceedings of SPIE, 924:208-214.

Brest, C.L. and Rossow, W.B. (1992). Radiometric calibration and monitoring of NOAA AVHRR data for ISCCP. International Journal of Remote Sensing, 13(2):235-273.

Che, N. and Price, J.C. (1992). Survey of radiometric calibration results and methods for visible and near infrared channels of NOAA-7, -9, and -11 AVHRRs. Remote Sensing of Environment, 41:19-27.

Cihlar, J., Ahern, F.J., D'Iorio, M.A., Guindon, B., Teillet, P.M. and Fisher, T. (1990). Mapping land cover of Canada from AVHRR data. Proceedings of the 1990 International Geoscience and Remote Sensing Symposium (IGARSS '90), pp. 1237-1243. College Park, Maryland.

D'Iorio, M.A., Cihlar, J. and Morasse, C. (1991). Effect of the calibration of AVHRR data on the normalized difference vegetation index and compositing. Canadian Journal of Remote Sensing, 17(3):251-262.

Erickson, A.D., Leung, P.S., Fisher, T.A., Teillet, P.M., Guindon, B. and Brown R.J. (1991). AVHRR data archiving and processing. Proceedings of the Fourteenth Canadian Symposium on Remote Sensing, pp. 205-210. Calgary, Alberta, Canada.

Faizoun, A.C., Editor, (1992). Final report of the OSS Working Group on NOAA AVHRR Standard Preprocessing Definition. LERTS, 18 ave. E. Belin, 31055 Toulouse Cédex, France.

Fraser, R.S. and Kaufman, Y.J. (1986). Calibration of satellite sensors after launch. Applied Optics, 25:1177-1185.

Frouin, R. and Gautier, C. (1987). Calibration of NOAA-7 AVHRR, GOES-5 and GOES-6 VISSR/VAS solar channels. Remote Sensing of Environment, 22:73-101.

Holben, B.N., Kaufman, Y.J. and Kendall, J.D. (1990). NOAA-11 AVHRR visible and near-IR inflight calibration. International Journal of Remote Sensing, 11:1511-1519.

Justus, C.G. (1988). Calibration of satellite shortwave sensors using overcast cloudlayer targets. Proceedings of SPIE, 24:120-128.

Kaufman, Y.J. and Holben, B.N. (1992). Calibration of the AVHRR visible and near-IR bands by atmospheric scattering, ocean glint and desert reflection. International Journal of Remote Sensing (in press).

Kidwell, K.B. (1991). NOAA Polar Orbiter Data Users' Guide. National Oceanic and Atmospheric Administration, World Weather Building, Washington, D.C.

Lauritson, L., Nelson, G.L. and Porto, F.W. (1979). Data extraction and calibration of TIROS-N/NOAA radiometers. NOAA Technical Memorandum NESS 107. National Oceanic and Atmospheric Administration, World Weather Building, Washington, D.C.

Manore, M. and Brown, R.J. (1986). Secondary targets for the radiometric correction of AVHRR imagery for crop monitoring. Proceedings of the Tenth Canadian Symposium on Remote Sensing, pp. 875-889. Edmonton, Alberta.

Morasse, C.-R. and D'Iorio, M.A. (1992). Développement d'une base de données AVHRR pour le Continent nord-americain dans le cadre des études sur les changements planétaires. Technical Note, Canadian Journal of Remote Sensing, 18(3) (in press).

Neckel, H. and Labs, D. (1984). The solar radiation between 3300 and 12500 Å. Solar Physics, 90:205-258.

Price, J.C. (1987). Calibration of satellite radiometers and the comparison of vegetation indices. Remote Sensing of Environment, 21:15-27.

Price, J.C. (1988a). An update on visible and near infrared calibration of satellite instruments. Remote Sensing of Environment, 24:419-422.

Price, J.C. (1988b). Erratum - Calibration of the NOAA 10 AVHRR. Remote Sensing of Environment, 26:303.

Robertson, B., Erickson, A., Friedel, J., Guindon, B., Fisher, T., Brown, R., Teillet, P., D'Iorio, M., Cihlar, J. and Sanz, A. (1992). Geocomp, a NOAA AVHRR data geocoding and compositing system. Proceedings of the ISPRS Congress XVII (Commission II), 6pp. Washington, D.C. (in press).

Santer, R.P. and Sharman, M. (1992). Temporal radiometric calibration of the visible and near infrared channels of the NOAA AVHRR instrument using invariant desert targets (in preparation).

Slater, P.N., Biggar, S.F., Holm, R.G., Jackson, R.D., Mao, Y., Moran, M.S., Palmer, J.M. and Yuan, B. (1987). Reflectance- and radiance-based methods for the in-flight absolute calibration of multispectral sensors. Remote Sensing of Environment, 22:11-37.

Staylor, W.F. (1990). Degradation rates of the AVHRR visible channel of the NOAA 6, 7 and 9 spacecraft. Journal of Atmospheric and Oceanic Technology, 7(3):411-423.

Smith, G.R., Levin, R.H., Koyanagi, R.S. and Wrigley, R.C. (1989). Calibration of the visible and near-infrared channels of the NOAA-9 AVHRR using high-altitude aircraft measurements from August 1985 and October 1986. NASA Technical Memorandum 101063, NASA Ames Research Center, Moffett Field, California.

Teillet, P.M. (1992). An algorithm for the radiometric and atmospheric correction of AVHRR data in the solar reflective channels. Remote Sensing of Environment (in press).

Teillet, P.M., Editor (1990). Report on a special meeting on AVHRR data preprocessing and compositing methods. Canada Centre for Remote Sensing, 22 pp. Ottawa, Ontario, Canada.

Teillet, P.M., Slater, P.N., Ding, Y., Santer, R.P., Jackson, R.D. and Moran, M.S. (1990). Three methods for the absolute calibration of the NOAA AVHRR sensors in-flight. Remote Sensing of Environment, 31:105-120.

Townshend, J.R.G., Editor (1992). Improved Global Data for Land Application: A Proposal for a New High Resolution Data Set. Report of the Land Cover Working Group of IGBP-DIS. IGBP Report No. 20, 87pp. Stockholm, Sweden.

SPOT CALIBRATION METHODS

Preflight methods

Ground absolute calibration using a large aperture integrating sphere (+ other sources)

Estimation of the instruments spectral sensitivity in vacuum conditions

In-flight methods

On-board calibration devices (halogen lamp, sun calibrator)

Absolute calibration by reference to earth's surface measurements over selected test sites : White Sands, Edwards AFB, La Crau

Intercalibration comparing simultaneous (or nearly simultaneous) acquired images with or without ground truth

Tech. Team Mtg - 12/3/92

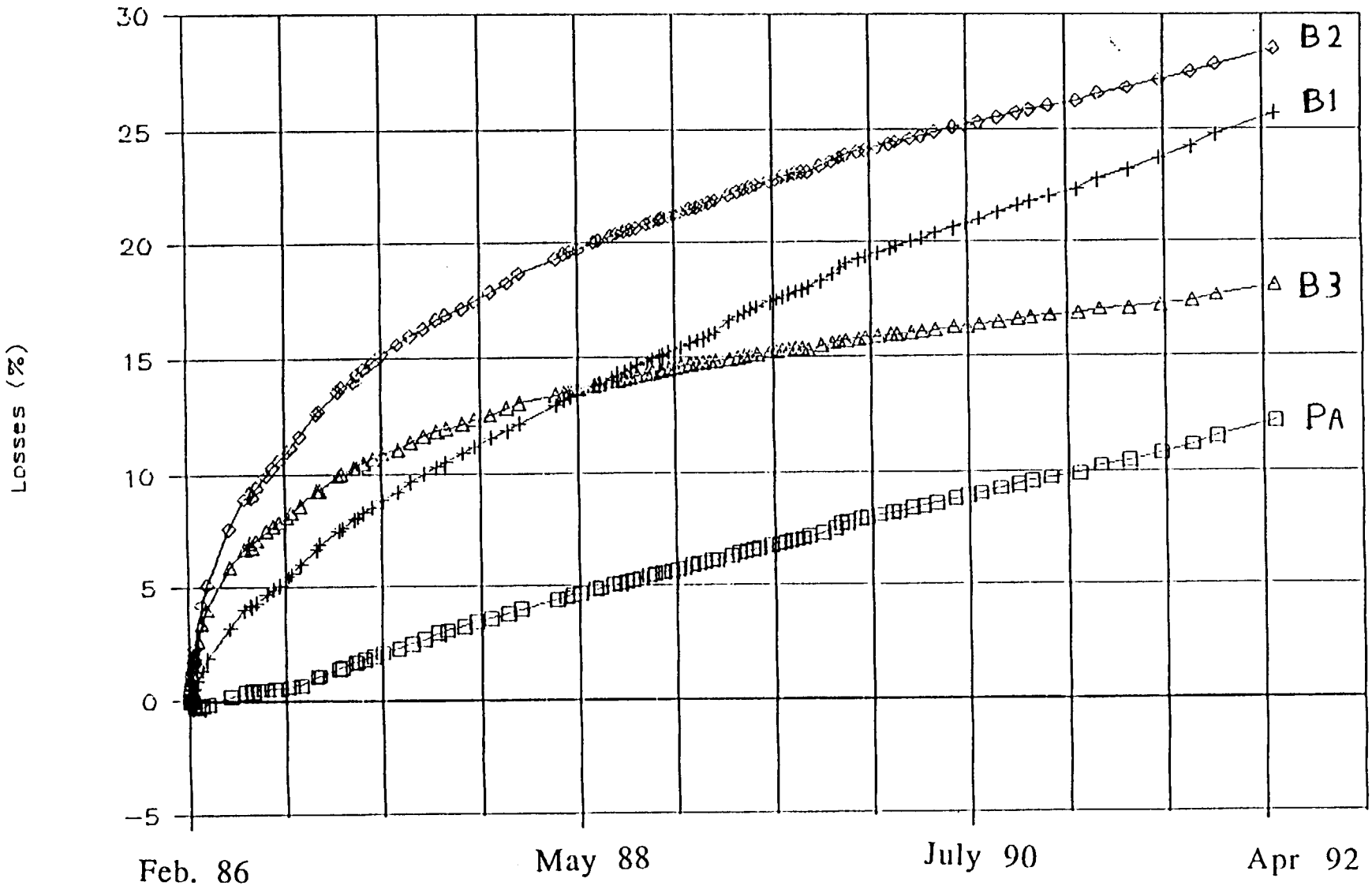

Fig. 1 : Lamp signal losses versus time for SPOT 1 HRV1

DEVELOPMENT OF NEW METHODS (1)

Stable desert areas

Some North African deserts are stable enough to represent good standard references, at least for multitemporal or interband calibration

SPOT 2 vertical acquisitions programmed over some selected sites.

The SPOT histograms data base

Storage in a data base of the histograms of all acquired cloud free images (more than 40000 scenes already stored)

Capability to get worldwide reflectance maps through the SPOT spectral bands

Opportunity of a statistical inter-SPOT calibration.

Figure 4.1 : Ak SPOT1 HRV2 Pa

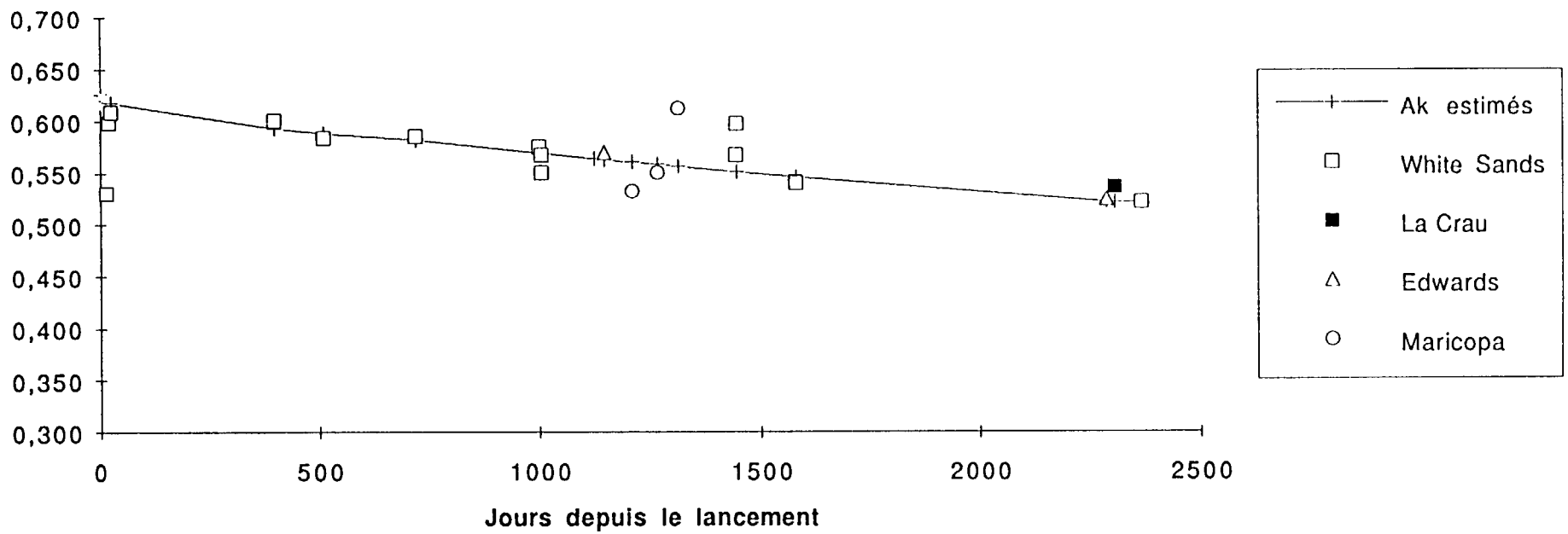

Figure 4.2 : Ak SPOT1 HRV1 Xs1

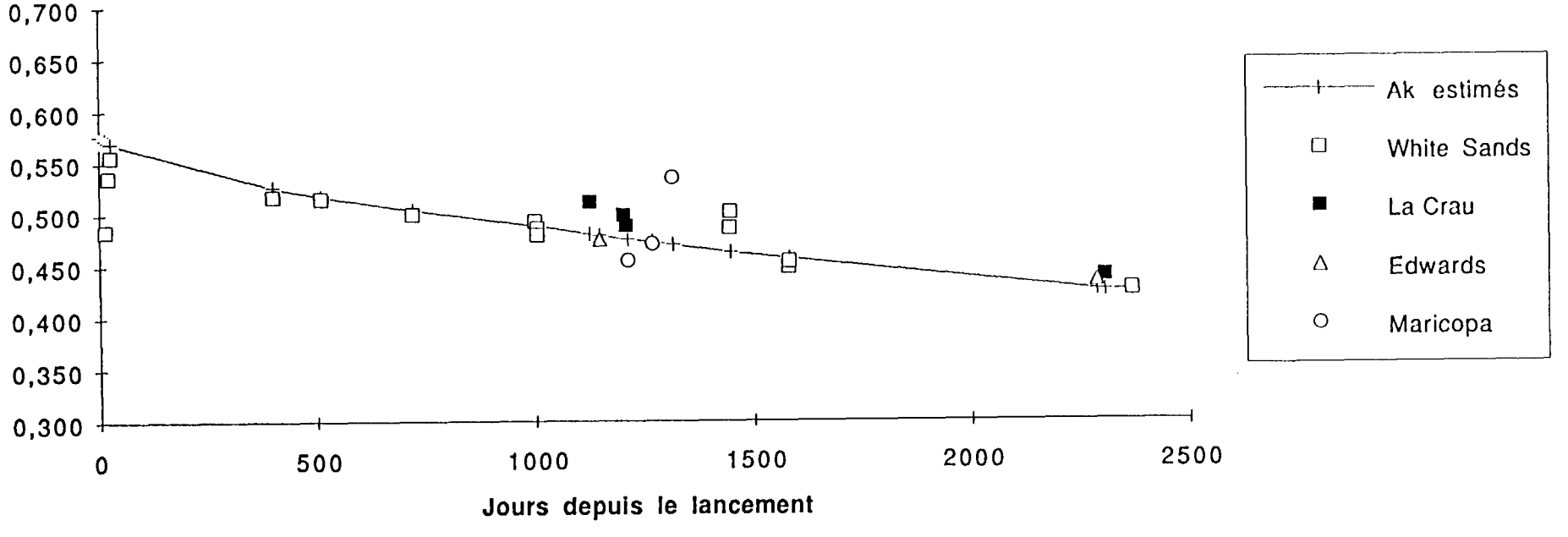

Figure 4.3 : Ak SPOT1 HRV1 Xs2

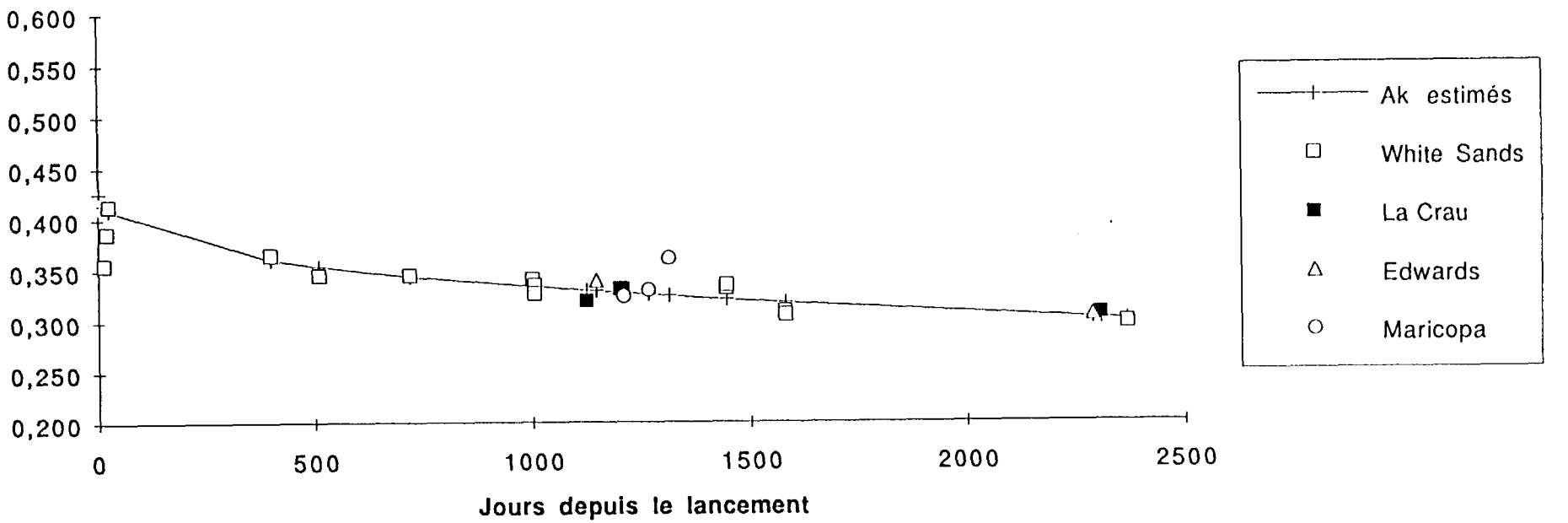

Figure 4.4 : Ak SPOT1 HRV1 Xs3

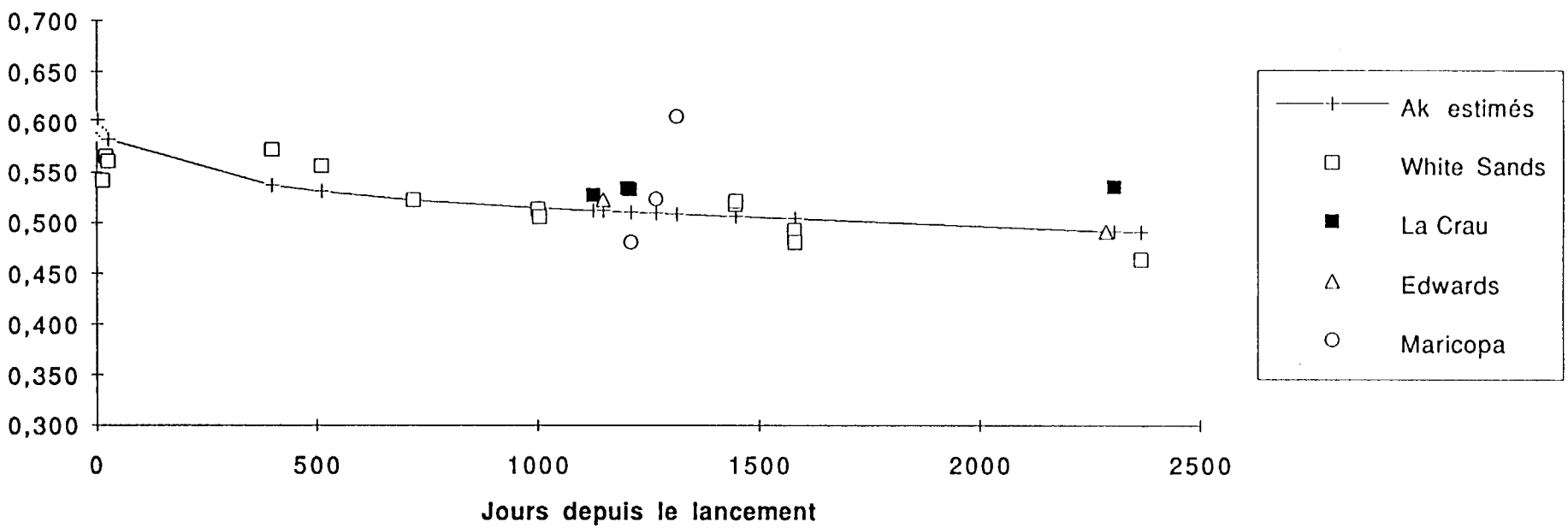

Figure 5.1 : Ak SPOT2 HRV1 Pa

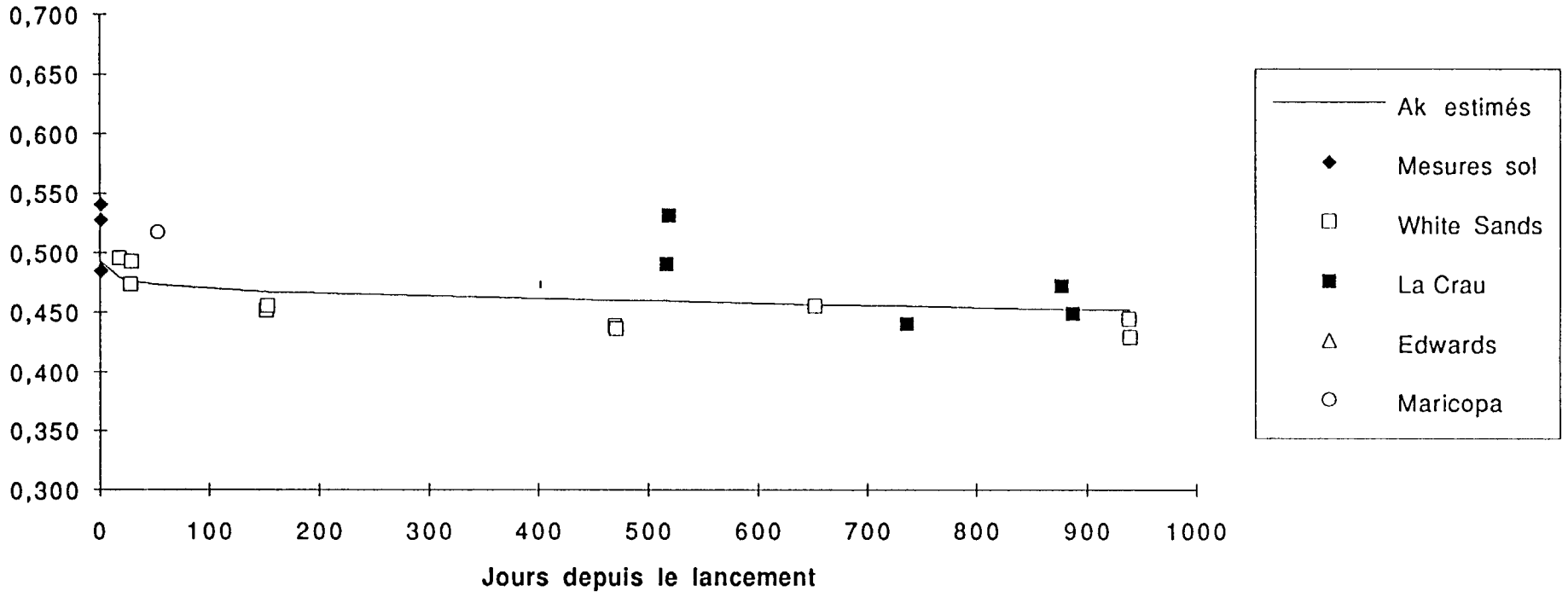

Figure 5.2 : Ak SPOT2 HRV2 Xs1

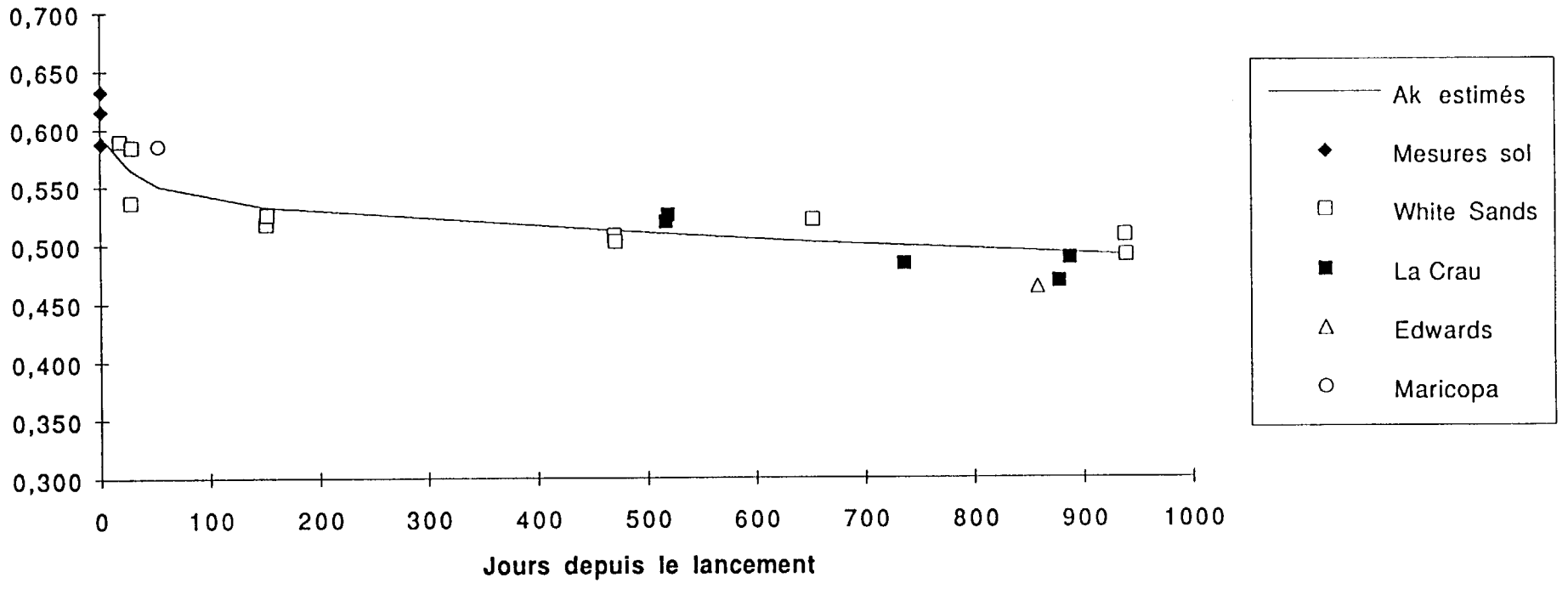

Figure 5.3 : Ak SPOT2 HRV2 Xs2

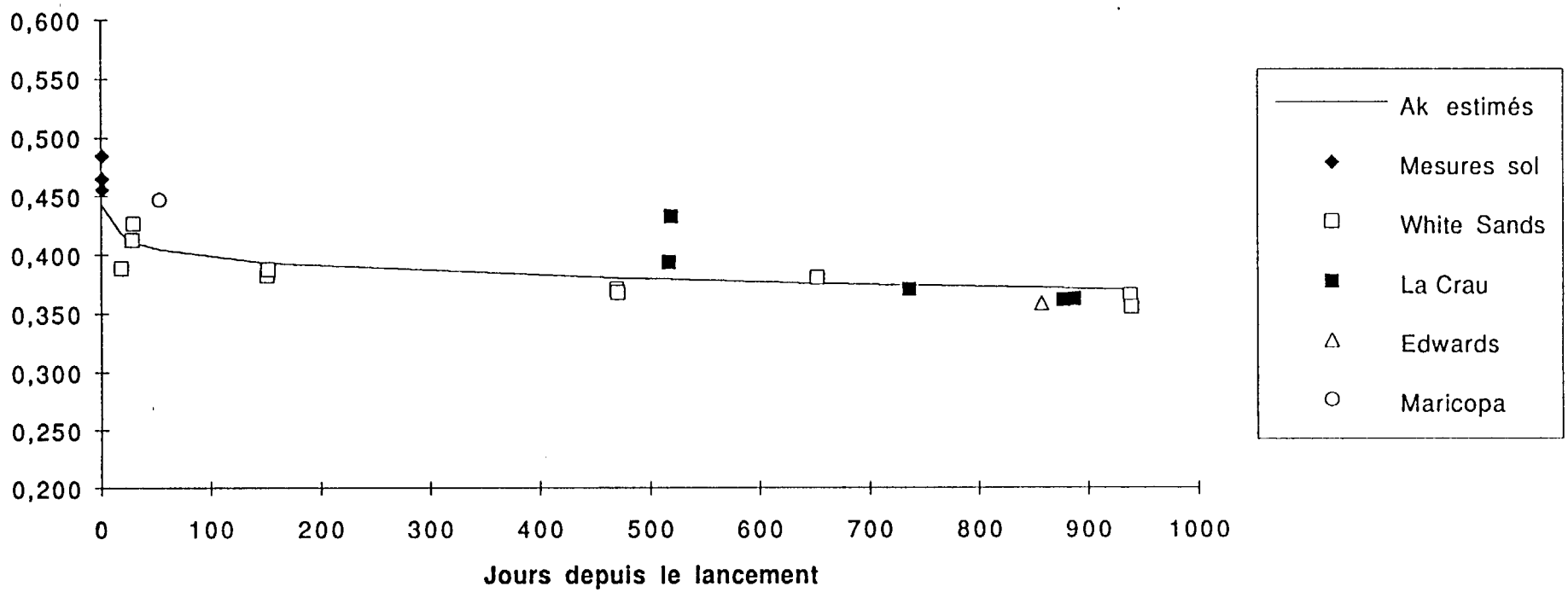

DRAFT 1

APPENDIX B: Airborne Imaging Spectrometer Sensor Characteristics
(FWHM = full-width-half-maximum, FOV = field-of-view, IFOV = instaneous field-of-view, GIFOV = ground instaneous field-of-view)

Sensor (Agency)	Number of Bands	Spectral Coverage (nm)	Band Width at FWHM(nm)	IFOV (mrad) (GIFOV (m))	FOV(°) (km)	Data Product	Period of Operation
FLI/PMI (MONITECH)	288 8	430-805	2.5	.66/.80	70.0	Profiles Image	1984-1990
CASI (Itres Research)	up to 288	430-870 (nominal)	2.9	1.2	35.0	Profiles Image	since 1989
SFSI (CCRS)	122	1200-2400	10.0	0.4 (≥0.5)	11.7	Image Cube	under construction (1993)
AIS-1 (NASA/JPL)	128	900-2100 1200-2400	9.3	1.91	3.7	Image Cube	1982-1985
AIS-2 (NASA/JPL)	128	800-1600 1200-2400	10.6	2.05	7.3	Image Cube	1985-1987
AVIRIS	224	400-2450	9.4-16.0	1.0 (20)	3.0 (12)	Image Cube	since 1987
ASAS (NASA/GSFC)	29	455-873	15.0	.80	25.0	Image Cube (7 viewing angles) +45°/-45°	1987-1991
upgraded ASAS	62	400-1060	11.5	.80	25.0	Image Cube (up to 10 viewing angles) +75°/-55°	since 1992
GERIS (GER)	24 7 32	400-1000 1000-2000 2000-2500	25.4 120.0 16.5	2.5, 3.3, or 4.5	90.0	Image Cube	since 1986
ROSIS (MBB/DLR)	128	430-850	≤5.0	0.55	32.4	Image Cube	since 1991
IMS	64 64	800-1700 1500-3000	12.5 25.0	3.3/11.7	40.0 (selectable)	Image Cube	since 1991
AMSS (GEOSCAN)	32 8 6	500-980 2000-2500 8000-12000	20.0-71.0 60.0 570.0	2.1/3.0	92.0	Image cube	since 1985

Dr Karl Staenz, CCRS/MPO

Susan Till/CCRS
27 NOV 1992

Tech. Team Mtg 12/3/1992 - 11-27

APPENDIX B (cont'd)

Sensor (Agency)	Number of Bands	Spectral Coverage (nm)	Band Width at FWHM(nm)	IFOV (mrad) (GIFOV (m))	FOV(°) (km)	Data Product	Period of Operation
DAIS-7915 (GER)	32 8 32 1	498-1010 1000-1800 1970-2450 3000-5000 8700-12300	16.0 100.0 15.0 2000.0 600.0	3.3, 2.2, or 1.1	78.0	Image Cube	under construction
ASTER (GER)	1 3 20	760-850 3000-5000 8000-12000	90.0 600.0 200.0	1,0, 2.5 or 5.0	28.8, 65.0, or 104.0	Image Cube	under construction
MIVIS (Daedalus)	20 8 64 10	433-833 1150-1550 2000-2500 8200-127000	20.0 50.0 8.0 400.0/500.0	2.0	70.0	Image Cube	under construction
HYDICE (Naval Research Laboratory)	256	400-500	4.7/11.7	0.5	7.2	Image Cube	under construction (1994)
ASDIS (Analytical Spectral Devices)	70 128 6	400-800 900-2450 8000-11000	7 12 500	2.8	82.0	Image Cube	under construction
HSI (SAIC)	128	400-900	4.3	0.14	9.3	Image Cube	under construction
MODIS Simulator (NASA/AMES)	9 16 16 9	529-969 1595-2405 2925-5325 8342-14521	31-55 nm 47-57 nm 142-151 nm 352-517 nm				under construction (1994)
MEIS (McDonnel Douglas)	>200	350-900	2.5 nm	2.5	2.0	Image Cube	

Staenz, CCRS/MPO (1992-11-27)

APPENDIX C: Spaceborne Imaging Spectrometer Sensor Characteristics
(FWHM = full-width-half-maximum, FOV = field-of-view, GIFOV = ground instaneous field-of-view)

Sensor (Agency)	Number of Bands	Spectral Coverage (nm)	Band Width at FWHM(nm)	GIFOV (mrad) (m)	FOV (km)	Data Product	Tentative Launch Date
UVIST (US MILITARY)	>200	380-900	1-3	(100-1000)	(25)	Image Cube	MSX spacecraft (1994)
NIMS (NASA/JPL)	504	700-5100	10	0.5		Image Cube	flown terrestrial mission
VIMS (NASA/JPL)	320	400-5000	15	0.5		Image Cube	flown terrestrial mission
MIN MAPS	192	350-2400	12.5	0.45	5.8	Image Cube	1996?
HIRIS (NASA/EOS)	192	400-2450	9.4/11.7	(30)	(24)	Image Cube	AM platform 2003
MODIS (NASA/EOS)	36	415-2130 3750-4570 6720-14240	10-500	(250-1000)	(2330)	Images	AM platform 1998 PM platform 2000
MERIS (ESA/EOS)	15 (selectable)	400-1050	5-10 (selectable)	(250-1000)	(1450)	Images	ESA-POEM 1 AM platform 1998

Staenz, CCRS/MPO (1992-11-27)